Measurement of Transverse Momentum Dependent Asymmetries with COMPASS Experiment at CERN

Dissertation

zur

Erlangung des Doktorgrades (Dr. rer. nat.)

der

Mathematisch-Naturwissenschaftlichen Fakultät

der

Rheinischen Friedrich-Wilhelms-Universität Bonn

vorgelegt von

Girisan Venugopal

aus

Chennai

Bonn 2007

Declaration

I hereby declare that the work in this thesis is original and has been carried out by me at the Helmholtz Institut für Strahlen- und Kernphysik, Universität Bonn, under the supervision of Prof. Dr. Frank Hinterberger and in partial fulfillment of the requirements of the Doctor rerum naturalium (Dr.rer.nat.) degree of the University of Bonn. I further declare that this work has not been the basis for the awarding of any degree, diploma, fellowship, associateship or similar title of any university or institution.

<div align="right">

Girisan Venugopal
September 2007

Helmholtz Institut für Strahlen- und Kernphysik,
Universität Bonn,
Nußallee 14-16, 53115 - Bonn ,
Germany.

</div>

Abstract

The COMPASS experiment, which started running at the European Council for Nuclear Research, CERN, in Geneva in 2001, is currently investigating in a wide ranging programme the spin structure of the nucleon through deep-inelastic scattering (DIS). The experiment uses a polarized muon beam and a polarized deuterium target, which together allow access to all terms of the polarized DIS cross-section. Two of the most important functions which COMPASS is designed to fulfil are a precision measurement of the gluon polarization ΔG and the investigation of the transverse spin effects, specially extracting the transverse polarized quark distribution functions $\Delta_T q$. In Semi-Inclusive DIS of polarized leptons on a transversely polarized target, eight azimuthal modulations appear in the cross-section. Within the QCD parton model, four azimuthal asymmetries can be interpreted at leading order, two of them being the Collins and Sivers asymmetries. The other two leading twist asymmetries are related to different transverse momentum dependent quark distribution functions. There are four additional asymmetries which can be interpreted as twist-three contributions. This thesis describes the analysis with the data taken with transverse spin configuration during the COMPASS beam-time 2002 - 2004, resulting in the extraction of the eight Transverse Momentum Dependent (TMD) asymmetries.

Contents

Chapter 1

Introduction - Physics Motivation

> "Wisdom is not a product of
> schooling but of the lifelong
> attempt to acquire it."
>
> Albert Einstein

The atomic nucleus consists of nucleons i.e. protons and neutrons. Since the mid 1960s it became clear that the nucleons are not the elementary particles i.e. fundamental indivisible constituents of the atomic nucleus. They have their own inner structure. The low energy properties of the nucleons and hyperons can be described by the constituent quark model in which baryon is made up of three strongly interacting constituent quarks (up, down and strange) with masses of about one third of the baryon mass. In this model, two of the quarks have spin $\frac{1}{2}$ in the up direction and one has spin $\frac{1}{2}$ in the down direction. The proton consists of two up quarks with charge $+\frac{2}{3}$ e and one down quark with charge $-\frac{1}{3}$ e, whereas the neutron consists of two down quarks and one up quark. These quarks are point-like structureless particles whose interactions are through the exchange of vector bosons in strong interaction, namely, *gluons*

The structure of the nucleon can be studied by scattering a beam of leptons off a target nucleon. When the incident lepton beam has very high energy compared to the nucleon mass then we can explore the internal structure of the nucleons. Deep Inelastic Scattering (DIS) involving large momentum transfer showed that a nucleon is made up of point-like constituents, the so-called *partons*. These partons introduced by Feynman have a lot in common with the constituent quarks of Gell-Mann and Zweig, which also have spin 1/2, electric charges of $+\frac{2}{3}$ e and $-\frac{1}{3}$ e, flavor and color, but very small masses ($m_u \approx 4$ MeV/c^2, $m_d \approx 7$ MeV/c^2 and $m_s \approx 150$ MeV/c^2) and are called *current* quarks in order to distinguish them from the constituent quarks. In parton model, the nucleon consists of three nearly massless valence quarks, quark-antiquark pairs (sea quarks) and gluons. The ap-

pearance of the first data on polarized deep inelastic scattering (DIS) opened a new field of experimental and theoretical investigation. Originally, it was assumed that the spin of the nucleon, $\frac{1}{2}$, could be fully attributed to the spin of the quarks. It was assumed that the spins of two quarks cancel each other and the remaining quark gives the spin of the nucleon. A measure of the quark spin distribution is given by the helicity distribution function Δq. In the infinite momentum frame, where the nucleon is moving with a very high momentum, the helicity distribution describes the number of quarks with their spin aligned with that of the nucleon minus the number of quarks with opposite spin.

$$\frac{1}{2} = \frac{1}{2}\Delta\Sigma + \Delta G + L_q + L_g. \tag{1.1}$$

Eq. (1.1) illustrates that the total spin of the nucleon must arise from the combination of three sources :
(i) The spin distribution of the quarks($\Delta\Sigma$)
(ii) The spin distributions of the gluons(ΔG)
(iii) The angular momentum of quarks and gluons L_q, L_g
The quark spin contribution can be further decomposed into contributions from the different flavors i.e. $\Delta\Sigma =\Delta u+\Delta\overline{u}+\Delta d+\Delta\overline{d}+\Delta s+\Delta\overline{s}$. The contributions of charm or heavier quarks is usually neglected as it is believed to be very small. It was a surprise (called as *spin crisis*) when the EMC experiment showed in late 1980s that only a small fraction ($\Delta\Sigma = 0.12 \pm 0.09 \pm 0.14$) of the proton spin could be attributed to the quark spins. The "*spin crisis*" urged further investigations in an attempt to find the missing component. COMPASS [1] is a fixed target experiment on the SPS M2 beamline at CERN, which was proposed to measure the contribution of the gluons to the nucleon spin (ΔG).

The measurement of another unknown quantity, the transverse spin or *transversity* distribution is also one of the main goals of COMPASS. In the infinite momentum frame with the nucleon's spin transverse to the direction of motion, the transversity distribution $\Delta_T q$ or h_1 or δ_q describes the number of quarks with their spin aligned in transverse direction parallel to the nucleon's spin minus the number of quarks with antiparallel alignment. In the rest frame of the nucleon, the probability to find quark spin aligned with the nucleon spin does not depend on the nucleon's spin orientation. However, if the nucleon is boosted to a very high momentum in the direction of its spin, the alignment probability corresponds to the helicity distribution. If the nucleon is boosted transverse to its spin, the quark spin distribution corresponds to a different distribution known as the transversity distribution. Transversity is another piece of the nucleon's spin structure. It can give new and important information on the inner structure of the nucleon. Besides the helicity and the tranversity distribution functions, six other quark distribution functions exist for each quark flavor in leading twist, collectively called as the Transverse Momentum Dependent (TMD) distribution functions. The transversity distribution escaped notice untill 1979 when Ralston and Soper [2] found it in their study of Drell-Yan spin asymmetries for transversely polarized baryons. The reason is its

chiral-odd nature which requires the combination with another chiral-odd object in helicity observing processes.

1.1   Thesis outline

Extraction of eight target transverse spin dependent asymmetries with COMPASS data taken between the years 2002 - 2004 will be the scope this thesis. The theory of inner structure of the nucleon is reviewed in Chapter 2 with emphasis on the concept of the factorization of the deep-inelastic scattering process into distribution and fragmentation functions. A detailed description of COMPASS spectrometer and data acquisition system are presented in Chapter 3. The formalism of the extraction of TMD asymmetries from the experimental data and systematic studies performed are presented in Chapter 4. Final results obtained along with interpretation given by the model calculation are presented in Chapter 5. Chapter 6 has the summary and outlook to complete this thesis.

Chapter 2

Theoretical background

> "I am now convinced that
> theoretical physics is actually
> philosophy."
>
> Max Born

Attempting to understand the intrinsic spin structure of the proton and neutron has been an active area of both experimental and theoretical research for the past twenty years. With the confirmation that the proton and neutron were not elementary particles, physicists were challenged with the task of explaining the nucleon's spin in terms of its constituents. This chapter introduces the deep inelastic scattering (DIS) as one of the main tools to investigate the nucleon spin in section 2.1 along with the quark parton model. Section 2.2 introduces the inclusive DIS in QCD improved quark parton model whereas section 2.3 describes the semi-inclusive deep inelastic scattering. Final section 2.4 describes the target transverse spin dependent asymmetries.

2.1   Inclusive deep inelastic scattering

The scattering of point-like leptons [3], l off a nucleon N offers a clean probe to investigate the structure of protons and neutrons. In this process

$$l + N \to l' + X. \tag{2.1}$$

Here l is the initial lepton, N is the target nucleon, l' is the scattered lepton and X is the final state hadrons. Fig. 2.1 shows a schematic diagram of deep inelastic scattering. The lepton with four-momentum $k = (E, \vec{k})$ is scattered at an angle θ. In case of elastic scattering, it is directly connected to the energy of the scattered
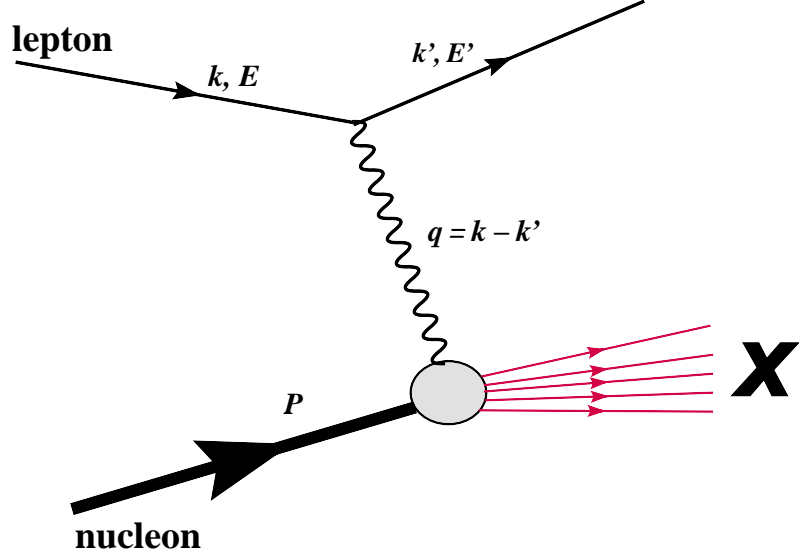
Figure 2.1: The basic diagram for deep-inelastic scattering lepton hadron scattering.The virtual photon momentum is q. The final hadronic state is not measured and is denoted by X

lepton with four-momentum $k' = (E', \vec{k'})$. Thus one variable is sufficient to describe the process. To describe inelastic scattering, two independent variables are needed, e.g. θ and E', as the lepton has enough energy to break up the proton. In deep inelastic scattering the invariant mass W of the final hadronic state X is well above the resonance region and the four-momentum transfer, $q = k - k'$, of the exchanged boson is large enough to resolve the nucleon's constituents and to investigate their properties. For COMPASS kinematics the exchanged boson is usually a virtual photon.

2.1.1 Kinematics

The relevant kinematic variables for the description of the DIS process are summarized in Table. 2.1. Instead of using E' and the lepton scattering angle θ to characterize the process, two dimensionless scaling variables,

$$y = \frac{P.q}{P.k} = \frac{\nu}{E},$$ (2.2)

and

$$x = \frac{Q^2}{2P \cdot q} = \frac{Q^2}{2M\nu},$$ (2.3)

are used. Here P is the four-momentum of the target nucleon, M the nucleon's mass, $\nu = E - E'$, the virtual photon energy, y, the fractional energy, x, the Bjorken scaling variable and $Q^2 = -q^2$. The invariant mass of the photon nucleon system is

$$W^2 = (P + q)^2 = M^2 + 2M\nu - Q^2$$ (2.4)

The Bjorken scaling variable x is interpreted as the fraction of the nucleon momen-

$q = k - k'$	four-momentum transfer to the target
$s = (P, k)^2 \approx M^2 + 2ME$	squared centre-of-mass energy
$\nu = \frac{P.q}{M} \simeq E - E'$	energy transfer to the target
$Q^2 = -q^2 \approx 4EE' sin^2(\theta/2)$	squared invariant mass of the virtual photon
$W^2 = (P + q)^2 = M^2 + 2M\nu - Q^2$	squared mass of the final state
$x = \frac{Q^2}{2P.q} = \frac{Q^2}{2M\nu}$	Bjorken scaling variable
$y = \frac{P.q}{P.k} = \frac{\nu}{E}$	fractional energy transfer to the target

Table 2.1: kinematic variables used in the description of DIS

tum carried by the struck quark in the infinite momentum frame.

2.1.2 The deep-inelastic cross-section

The differential cross-section for inclusive DIS, where the scattering lepton has an energy between E' and $E' + dE'$ and is found in the solid angle $d\Omega$, can be written as a product of a leptonic tensor $L_{\mu\nu}$ and a hadronic tensor $W_{\mu\nu}$ [4, 5]

$$\frac{d^3\sigma}{d\Omega dE'} = \frac{y\alpha^2}{2Mq^4}\frac{E'}{E}L_{\mu\nu}W^{\mu\nu}. \qquad (2.5)$$

Here α is the electromagnetic coupling constant. The leptonic and hadronic tensor describe the interaction at the leptonic and hadronic vertices of the DIS process [6, 7]. They can be split up into parts which are symmetric and antisymmetric under parity transformation as follows:

$$L_{\mu\nu}^{(S)}(k, k') + iL_{\mu\nu}^{(A)}(k, k', s), \qquad W_{\mu\nu}^{(S)}(P, q) + iW_{\mu\nu}^{(A)}(P, q, S). \qquad (2.6)$$

Here only the antisymmetric parts are spin-dependent. In the cross-section of Eq. (2.5), antisymmetric combinations of $L_{\mu\nu}$ and $W_{\mu\nu}$ do not appear due to parity conservation of the electromagnetic interaction.

Since the lepton is a point-like spin-1/2 particle, the leptonic tensor can be calculated in the formalism of QED[1]. The small electromagnetic coupling constant $\alpha \approx 1/137$ and the fact that photons do not couple to themselves allow the application of

---

[1]Quantum Electrodynamics

perturbative QED. Using Dirac matrices and the Dirac spinor for spin-1/2 particles with four momentum and spin four vectors, the leptonic tensor reads like [8]:

$$L_{\mu\nu} = 2 \left(k_\mu k'_\nu + k_\nu k'_\mu - g_{\mu\nu}(kk' - m^2) + im\epsilon_{\mu\nu\lambda\sigma}q^\lambda s^\sigma \right). \tag{2.7}$$

Here, $g_{\mu\nu}$ denotes the metric tensor, $\epsilon_{\mu\nu\lambda\sigma}$ denotes the Levi-Civita tensor. $W_{\mu\nu}$ parameterizes our lack of knowledge of the nucleon structure and is defined by [9],

$$W_{\mu\nu} = \frac{1}{2\pi} \int d^4x e^{iq.x} \langle P, S | [j^\mu(x), j^\nu(0)] | P, S \rangle. \tag{2.8}$$

S is the spin vector of the nucleon with momentum P and $\langle P, S | [j^\mu(x), j^\nu(0)] | P, S \rangle$, the nucleon matrix elements of the commutator of electromagnetic currents $j^\mu(x)$ and j^ν. The hadronic tensor $W_{\mu\nu}$ does not describe an elementary particle but a particle with an unknown internal structure. The complex inner structure of the nucleon prevents the calculation of the hadronic tensor. The hadronic tensor is parameterized with the help of four *structure functions* F_1, F_2, g_1 and g_2. They depend on two independent variables x and Q^2 in DIS.

$$W_{\mu\nu} = 2\left[F_1(x, Q^2)\left(-g_{\mu\nu} + \frac{q^\mu q^\nu}{q^2} \right) + \frac{F_2(x, Q^2)}{Pq}\left(P^\mu - \frac{Pq}{q^2}q^\mu \right)\left(P^\nu - \frac{Pq}{q^2}q^\nu \right) + \right.$$
$$\left. +i\frac{M}{Pq}\epsilon^{\mu\nu\lambda\sigma}q\lambda\left(g_1(x, Q^2)S_\sigma + g_2(x, Q^2)(S_\sigma - \frac{S_q}{Pq}P_\sigma) \right) \right] \tag{2.9}$$

The two structure functions $F_1(x, Q^2)$ and $F_2(x, Q^2)$ are associated with unpolarized DIS whereas $g_1(x, Q^2)$ and $g_2(x, Q^2)$ with polarized DIS. The combination of the general expressions for $L_{\mu\nu}$ and $W_{\mu\nu}$ in Eq. (2.5) also produces separate symmetric and anti-symmetric terms :

$$\frac{d\sigma}{d\Omega dE'} = \frac{\alpha^2}{Mq^4}\frac{E'}{E}\left(L^{(S)}_{\mu\nu}(k, k')W^{\mu\nu(S)}(P, q) - L^{(A)}_{\mu\nu}(k, k', s)W^{\mu\nu(A)}(P, q, S) \right) \tag{2.10}$$

The resultant double spin dependence on both the lepton spin s and the hadron spin S of the anti-symmetric part of the cross-section suggests that this term must be investigated with polarized beam and target. The COMPASS experiment with polarized beam and target is in a position to perform such investigations. For such an investigation with an experiment like COMPASS, it is only possible to produce a muon beam which is polarized either parallel or anti-parallel to the direction of its momentum. It is the target polarization which can be chosen without restriction.

2.1.3 The unpolarized cross-section

Averaging over all spin states in the initial state of the scattering process, only the spin independent symmetric parts of the leptonic and hadronic tensors survive and

the unpolarized cross-section can be written as [10]

$$\frac{d\sigma^{unpol}}{d\Omega dE'} = \frac{\alpha^2}{Mq^4}\frac{E'}{E}L_{\mu\nu}^{(s)}W^{\mu\nu(s)} \tag{2.11}$$

$$= \frac{4\alpha^2 E'^2}{q^4}\left[\frac{2F_1(x,Q^2)}{M}\sin^2\frac{\theta}{2} + \frac{F_2(x,Q^2)}{\nu}\cos^2\frac{\theta}{2}\right] \tag{2.12}$$

The structure functions $F_1(x,Q^2)$ and $F_2(x,Q^2)$ reflect the unpolarized inner structure of the nucleon. The structure functions are approximately independent of the momentum transfer from the probe to the nucleon, this phenomenon is known as Bjorken scaling [11].

2.1.4 The polarized cross-section

In contrast to the symmetric part, the antisymmetric part of the cross-section depends on the lepton and the nucleon spin. For a lepton with its spin and momentum aligned, i.e. longitudinally polarized, the cross-section depends on the azimuthal and polar angles, φ and β, of the target spin S with respect to the lepton beam (see Fig. 2.2). In the difference between two opposite target polarization states ± 1, the
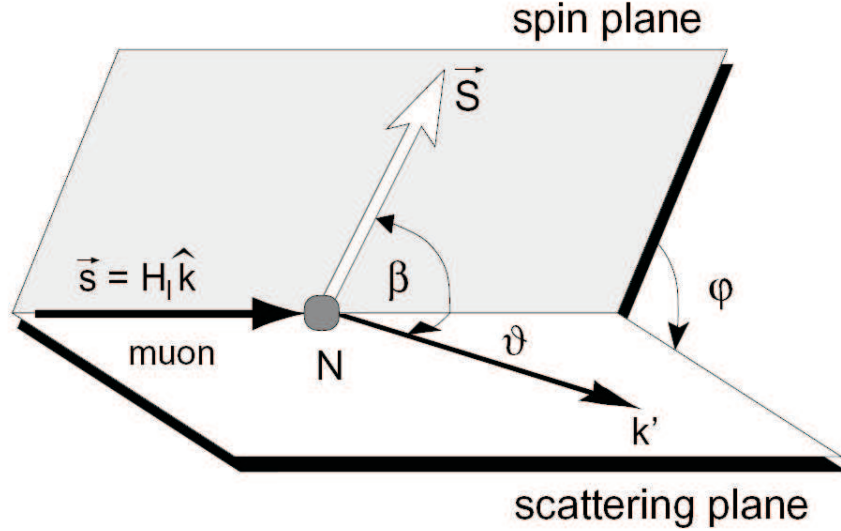

Figure 2.2: Definition of azimuthal and polar angles of the target spin S

unpolarized cross-section cancels and one obtains the polarized cross-section [10]

$$
\frac{d^3\sigma^{pol}}{dxdyd\varphi} = \frac{d^3\sigma(+1)}{dxdyd\varphi} - \frac{d^3\sigma(-1)}{dxdyd\varphi} \tag{2.13}
$$

$$
= \frac{4\alpha^2}{sxy}\left\{ \left[\left(2 - y - \frac{\gamma^2 y^2}{2}\right)g_1(x, Q^2) - \gamma^2 y g_2(x, Q^2)\right]\cos\beta +
$$

$$
+\gamma\sqrt{1 - y - \frac{\gamma^2 y^2}{4}}[\gamma g_1(x, Q^2) + 2g_2(x, Q^2)]\sin\beta\cos\varphi \right\} \tag{2.14}
$$

If the target nucleons are longitudinally polarized, where $\beta = 0$, then the cross-section reduces to

$$
\frac{d^3\sigma^{\rightarrow\Rightarrow}}{dxdyd\varphi} - \frac{d^3\sigma^{\rightarrow\Leftarrow}}{dxdyd\varphi} = \frac{4\alpha^2}{sxy}\left[\left(2 - y - \frac{\gamma^2 y^2}{2}\right)g_1(x, Q^2) - \gamma^2 y g_2(x, Q^2)\right]. \tag{2.15}
$$

Here $\rightarrow$ indicates the spin orientation of the incoming lepton whereas $\Rightarrow\Leftarrow$ indicates the different spin states of the target nucleon. The cross-section is dominated by the structure function $g_1(x, Q^2)$ because $g_2(x, Q^2)$ is suppressed by the factor $\gamma \approx 1/Q^2$ and it vanishes in the simple quark parton model (see section 2.1.6). The contribution of $g_2(x, Q^2)$ vanishes completely in the case of a target polarized longitudinally with respect to the virtual photon.
In the case of target polarized transverse to the incoming lepton beam, then $\beta = \pi/2$ and the polarized cross-section remains φ dependent

$$
\frac{d^3\sigma^{\rightarrow\Downarrow}}{dxdyd\varphi} - \frac{d^3\sigma^{\rightarrow\Uparrow}}{dxdyd\varphi} = \frac{4\alpha^2}{sxy}\gamma\sqrt{1 - y - \frac{\gamma^2 y^2}{4}}\left\{\gamma g_1(x, Q^2) + 2g_2(x, Q^2)\right\}\cos\varphi. \tag{2.16}
$$

Here, neither $g_1(x, Q^2)$ nor $g_2(x, Q^2)$ dominates the cross-section. The combination of measurements on longitudinally and transversely polarized target allows the extraction of $g_2(x, Q^2)$ [12].

2.1.5 Forward virtual Compton scattering

The asymmetries are often expressed in terms of the flow of virtual photons absorbed by the nucleon, with the beam lepton playing no role other than that of a photon source. The optical theorem relates the hadronic tensor to the imaginary part of the forward virtual Compton scattering amplitude $T_{\mu\nu}$:

$$
W_{\mu\nu} = \frac{1}{2\pi}ImT_{\mu\nu} \tag{2.17}
$$

with

$$
T_{\mu\nu} = i\int d^4\xi e^{iq\cdot\xi} < PS \mid T(J_\mu(\xi)J_\nu(0)) \mid PS > \tag{2.18}
$$

The optical theorem relates the imaginary part of the Compton scattering amplitude to the virtual-photon absorption cross-sections. The following relations between these and the nucleon structure functions may be obtained [13]:

$$\sigma_L^0 = \frac{4\pi^2\alpha}{MK}\Big(-F_1 + \frac{F_2}{2x}(1+\gamma^2)\Big), \tag{2.19}$$

$$\sigma_T^{1/2} = \frac{4\pi^2\alpha}{MK}\Big(F_1 + g_1 - \gamma^2 g_2\Big), \tag{2.20}$$

$$\sigma_T^{3/2} = \frac{4\pi^2\alpha}{MK}\Big(F_1 - g_1 + \gamma^2 g_2\Big), \tag{2.21}$$

$$\sigma_{TL}^{1/2} = \frac{4\pi^2\alpha}{MK}\Big(\gamma(g_1 + g_2)\Big). \tag{2.22}$$

Here, M is the nucleon mass and $K = \nu - Q^2/2M$ is the normalization factor [14]. The indices $\frac{1}{2}$ and $\frac{3}{2}$ represent the relative alignment of the photon and nucleon spins in relation to one another (anti-parallel or parallel).

The ratio of the photo-absorption cross-sections of longitudinal and transverse virtual photons is given by:

$$R(x, Q^2) = \frac{\sigma_L(x, Q^2)}{\sigma_T(x, Q^2)}, \tag{2.23}$$

with which, the structure functions $F_1(x, Q^2)$ and $F_2(x, Q^2)$ can be related to each other by

$$R(x, Q^2) = \frac{(1+\gamma^2)F_2(x, Q^2) - 2xF_1(x, Q^2)}{2xF_1(x, Q^2)}. \tag{2.24}$$

In the Bjorken limit where $Q^2 \to \infty$, $\nu \to \infty$ and x remains constant, the kinematic factor γ can be neglected and the photo-absorption cross-section σ_L with helicity 0 vanishes as a consequence of the requirement of helicity conservation at the virtual photon-parton scattering vertex. Thus $R \to 0$ and Eq. (2.23) yields the Callan-Gross relation [15].

$$F_2(x, Q^2) = 2xF_1(x). \tag{2.25}$$

This relation has been verified experimentally from SLAC data [16], [17], [18], [19], [20] and is an evidence that the constituents of the nucleon are spin $\frac{1}{2}$ particles.

2.1.6 The quark parton model

The quark parton model developed by R.P.Feynman at the beginning of the 1960s describes the nucleon as composed of smaller fundamental constituents, which Feynman called *partons* [21]. These building blocks of the nucleon swiftly became identified with *quarks*, the existence of which had been postulated independently by Gell-Mann [22] and Zweig [23] a few years before. Quarks are the particles with one-third integer charge and a spin of one half.

The quark parton model allows us to understand structure function in terms of

quarks. According to QPM, a deep-inelastic scattering event can be regarded as a superposition of elastic lepton-parton scattering processes. This holds true only when the momentum transfer Q^2 of the photon is sufficiently large so that the individual partons can be resolved. The interaction must be of short duration so that the partons cannot interact among themselves. If the hit parton, q, carries the fraction ξ of the hadron's four-momentum, $p_q = \xi P$, the energy in the hadronic final state, W, is

$$W^2 = (p_q + q)^2 \tag{2.26}$$

For a structureless parton, only elastic scattering can occur requiring $W^2 = (\xi M)^2$. Using this identity the above equation can be written as:

$$\xi^2 M^2 = \xi^2 P^2 + 2\xi Pq + q^2. \tag{2.27}$$

Substituting the identities, $q^2 = -Q^2$ and $P = M$ we get,

$$\xi = \frac{Q^2}{2pq} \equiv x. \tag{2.28}$$

Thus the Bjorken variable x has a very intuitive interpretation as the fraction of nucleon momentum carried by a single parton before a scattering event.
For scattering from a free massless spin-$\frac{1}{2}$ parton inside a hadron, the hadronic tensor, $W^{\mu\nu}$ can be calculated and one finds the structure functions:

$$F_1^{parton}(x) = \frac{1}{2} e_p^2 \delta(\xi - x), \quad F_2^{parton}(x) = e_p^2 \xi \delta(\xi - x).$$

$$g_1^{parton}(x) = \lambda \frac{1}{2} e_p^2 \delta(\xi - x), \quad g_2^{parton}(x) = 0. \tag{2.29}$$

Here e_p is the parton's charge and δ is the Dirac function. The factor $\lambda = \pm 1$ represents the spin direction of the parton in relation to the nucleon spin. It accounts for the fact that g_1 is defined using the nucleon's spin orientation and therefore an additional minus sign is needed when the parton's spin is oriented opposite to the one of the nucleon. The fourth structure function g_2 does not have a simple interpretation in the quark parton model because it is generally assumed that no quark has spin transverse to the nucleon spin.
The probability to find a parton inside a nucleon of a certain type carrying momentum fraction ξ is parameterized by the parton distribution functions $q_i^\lambda(\xi)$. For the quarks, $q_i = u, d, s, ...$ is used whereas for the gluons $q_i = g$ is used. For a longitudinally polarized nucleon, parallel and antiparallel orientation of the parton spin with respect to the nucleon spin are denoted by $\lambda = \pm 1$, whereas for transversely polarized nucleon, it is denoted by $\lambda = (\uparrow, \downarrow)$. Usually the $q_i(x)$ is understood as the sum of the distribution functions of quarks and anti-quarks in both helicity states of particular flavor i, whose spins are parallel or anti-parallel to the nucleon spin.

$$q = q^+ + q^-, \quad \Delta q = q^+ - q^-, \quad \Delta_T q = q^\uparrow - q^\downarrow. \tag{2.30}$$

Here Δq denotes the difference of the helicity states and $\Delta_T q$ is the transversity distribution function. The hadron structure functions are then given by:

$$F(x) = \sum_{i,\lambda} \int_0^1 q_i^\lambda(\xi) F^{parton}(x, \xi) d\xi. \tag{2.31}$$

Here i runs over all quark flavors and $F = F_1, F_2, g_1$, and g_2 yielding,

$$F_1(x) = \frac{1}{2} \sum_i e_i^2 \Big(q_i^+(x) + q_i^-(x) \Big) = \frac{1}{2} \sum_i e_i^2 q_i(x) \tag{2.32}$$

$$F_2(x) = x \sum_i e_i^2 \Big(q_i^+(x) + q_i^-(x) \Big) = x \sum_i e_i^2 q_i(x) \tag{2.33}$$

$$g_1(x) = \frac{1}{2} \sum_i e_i^2 \Big(q_i^+(x) - q_i^-(x) \Big) = \frac{1}{2} \sum_i e_i^2 \Delta q_i(x) \tag{2.34}$$

$$g_2(x) = 0. \tag{2.35}$$

2.1.7 QCD improved quark parton model

In the late 70s, a more or less complete description of the nucleon was given by the field theory of Quantum Chromo-dynamics (QCD). QCD is the non-abelian gauge theory of the strong interaction through different colors. QCD introduces gluons as vector bosons conveying the strong nuclear interaction. In the QCD improved quark parton model, the quarks can radiate gluons, which can themselves either be re-absorbed by the quarks to produce quark-antiquark pairs or radiate further gluons. Quarks couple to the strong interaction through three different colors. In contrast to Quantum Electrodynamics (QED) where the photons have no electrical charge and cannot couple to each other, the field quanta of the strong interaction i.e the gluons, do carry charge. This causes a scale or energy dependence of the strong coupling constant α_s.

$$\alpha_s(Q^2) = \frac{12\pi}{(33 - 2n_f)ln(Q^2/\Lambda_{QCD}^2)} \tag{2.36}$$

Here Λ_{QCD}^2 is the QCD scale parameter which depends on the number of quark flavors n_f and the re-normalization scheme. The above equation is valid only for $Q^2 \gg \Lambda_{QCD}^2$. This shows that the coupling constant decreases with increasing Q^2. For $\alpha_s \ll 1$, one has to apply perturbative QCD method. But the coupling constant is not to be necessarily smaller than 1 for small Q^2 region, so the perturbation theory fails. For this so-called confinement region ($Q^2 \leq 1$ GeV/c), where α_s is of the order of 1 or larger, lattice QCD calculations have to be used to describe the experimental data.

There is a depletion of high momentum partons and an increase in the low momentum parton distribution as Q^2 increases. This phenomenon known as *scaling violation* can be seen in Fig. 2.3, where the structure function F_2 is plotted as a function of Q^2 for different values of x.

With sufficiently large Q^2, the gluon can be resolved into a quark-antiquark pair and the photon can interact with one of them. Now the structure functions have the same form as in the case of QPM, but with Q^2 dependence. Their respective logarithmic behavior is described by the Dokshitzer-Gribov-Lipatov-Altarelli-Parisi
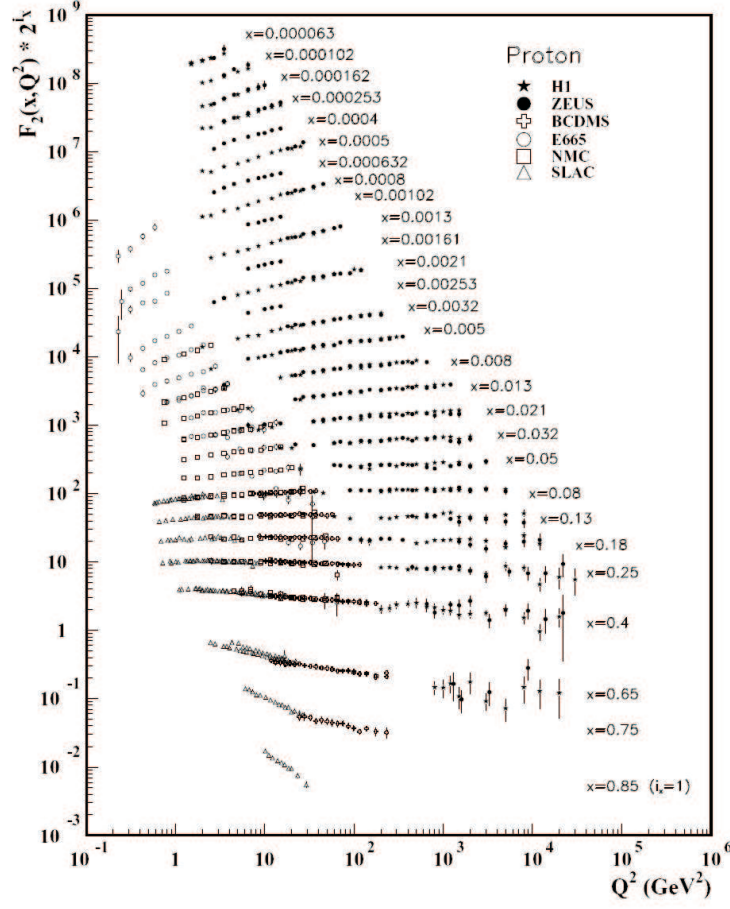
Figure 2.3: The proton structure function F_2 measured in electromagnetic scattering of positrons on protons at e-p collider HERA (ZEUS and H1) and for electrons (SLAC) and muons (BCDMS, E665, NMC) on a fixed target.

equations or simply DGLAP equations [24, 25, 26, 27]. The photo absorption cross-section ratio R (see Eq. (2.23)) now vanishes in the leading order perturbative QCD calculations. Therefore the Callen-Gross equation (see Eq. (2.25)) holds true also in the QCD improved QPM. However the structure function g_2 which vanishes in naive QPM (see Eq. (2.35)) does not vanish in QCD improved QPM, instead it arises from quark-gluon interactions.

2.2 Inclusive DIS in QCD improved QPM

In the QCD improved parton model, the scattering process can be described as elastic quark-lepton scattering inside the nucleon. In the interaction with a virtual photon with sufficiently large Q^2, quarks behave like quasi-free particles. The hand-bag diagram representing the hadronic tensor $W_{\mu\nu}$ [28] is shown in Fig. 2.4. The
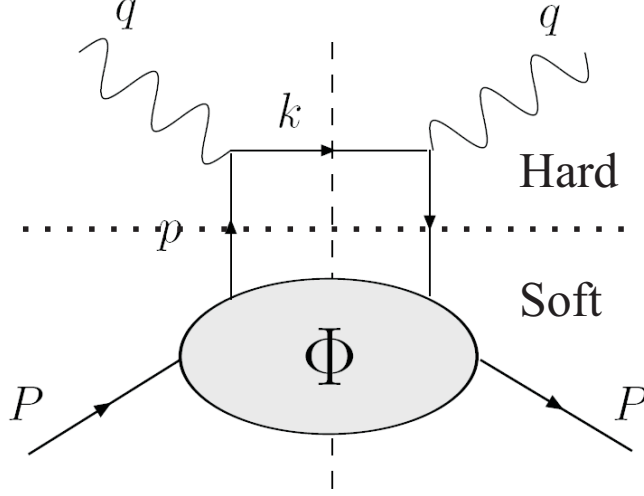
Figure 2.4: Handbag diagram. The virtual photon with 4-momentum q strikes a quark inside the nucleon with momentum p.

virtual photon is absorbed by a quark with initial four momentum p. Thus the four momentum of the outgoing quark is $k = p + q$. Neglecting quark masses, the hadronic tensor Eq. (2.8) is rewritten as

$$
\begin{aligned}
W_{\mu\nu}(q, P, S) = {} & \frac{1}{2\pi} \sum_q e_a^2 \sum_X \int \frac{d^3 P_X}{(2\pi)^3 2E_X} \int \frac{d^4 p}{(2\pi)^4} \int \frac{d^4 k}{(2\pi)^4} \\
& \times (2\pi)^4 \delta^4(P - p - P_X)(2\pi)^4 \delta^4(p + q - k) \\
& \times \Big([\bar{u}(k)\gamma^\mu \phi(p, P, S)]^* [\bar{u}(k)\gamma^\nu \phi(p, P, S)] \\
& + [\bar{\phi}(p, P, S)\gamma^\mu u(k)]^* [\bar{\phi}(p, P, S)\gamma^\nu u(k)] \Big).
\end{aligned}
\tag{2.37}
$$

Here p and k are quark momenta before and after interaction with the virtual photon, whereas P and S indicate the nucleon momentum and its spin.

The hadronic tensor can be decomposed into two parts, hard process and soft process as shown in Fig. 2.4. The soft part contains a non perturbative QCD part. The soft part can be described by introducing a quark-quark correlation function Φ.

$$
\begin{aligned}
\Phi_{i,j}(p, P, S) = {} & \sum_X \int \frac{d^3 P_X}{(2\pi)^3 2E_X} (2\pi)^4 \delta^4(P - p - P_X) \\
& \times \langle PS | \bar{\psi}_j(0) | X \rangle \langle X | \psi_i(0) | PS \rangle
\end{aligned}
\tag{2.38}
$$

The quark-quark correlation matrix $\Phi_{i,j}$ describes the confinement of the quarks inside the nucleon and depends on the four momentum of the quark p and the proton P and the spin of the proton S. In the above equation, ψ is the quark spinor with i, j being Dirac indices. At leading order of $1/Q$, the correlation function contains all the relevant information on the non-perturbative dynamics of quarks

inside the nucleon.

Using the quark-quark correlation function, the hadronic tensor can be rewritten as

$$
\begin{aligned}
W_{\mu\nu}(q, P, S) &= \sum_q e_q^2 \int \frac{d^4 p}{(2\pi)^4} \delta\left((p+q)^2 - m_q^2\right) \\
&\times Tr\left[\Phi(p, P, S)\gamma^\mu(\not p + \not q + m_q)\gamma^\nu \right. \\
&\left. + \bar\Phi(p, P, S)\gamma^\nu(\not p + \not q - m_q)\gamma^\mu\right].
\end{aligned}
\tag{2.39}
$$

Here Fourier transformation of Dirac delta function and the completeness of the $|X\rangle$ are used. $\bar\Phi$ is the correlation function of anti-quark which is obtained from Eq. (2.38) by interchanging ψ with $\bar\psi$.

2.2.1 Parton distribution functions

Quark level information of the nucleon can be obtained from the quark-quark correlation function. The information is expressed in terms of the parton distribution functions (PDF). Here we consider the nucleon momentum in light-cone coordinate system $P = (P^+, P^-, P_T = 0)$, similarly the quark momentum is expressed as $p = (p^+, p^-, p_T)$. The PDF is derived from the quark-quark correlation function and is obtained by integrating Φ over the rest of the components of quark momentum p^- and p_T. Thus the integrated Φ is a function of the light-cone momentum p^+. If we choose the infinite momentum frame, the transverse component of the momentum $|p_T|$ is small enough in comparison with the nucleon momentum P^+. Then one can write $p^+ \simeq xP^+$. Now the resulting integrated Φ depends only on the light-cone momentum fraction $x = p^+/P^+$ and S,

$$
\int dp^- d^2 p_T \Phi_{ij}(p, P, S)\Big|_{p^+=xP^+} = \Phi_{ij}(x, S).
\tag{2.40}
$$

Now the *projected* correlation function $\Phi^{[\Gamma]}$ can be introduced, which is defined as

$$
\Phi^{[\Gamma]}(x) \equiv \frac{1}{2}\int dp^- d^2 p_T Tr(\Phi(p, P, S)\Gamma).
\tag{2.41}
$$

Here Γ is a 4 x 4 Dirac matrix. The projection Γ determines the characteristic of the quark current j^q,

$$
j^q = \frac{1}{2}\bar\psi\Gamma\psi.
\tag{2.42}
$$

From this, the vector and axial currents are expressed as

$$
\text{Vectorcurrent} \;:\; j_v^q = \frac{1}{2}\bar\psi\gamma^+\psi
$$
$$
\text{Axialcurrent} \;:\; j_a^q = \frac{1}{2}\bar\psi\gamma^+\gamma^5\psi.
\tag{2.43}
$$

Parton distribution functions are defined using the projected Φ. In case of the vector current, the projection $\Gamma = \gamma^+$ gives the spin-independent parton distribution function f_1,

$$\Phi^{[\gamma^+]}(x) = f_1(x). \tag{2.44}$$

The spin-independent structure function F_1 can be reconstructed as the sum of the f_1 for possible quarks q and anti-quarks $\bar{q}$,

$$F_2(x) = 2xF_1(x) = \sum_{q/\bar{q}} e_q^2 f_1^q(x). \tag{2.45}$$

Similarly, by the projection $\Gamma = \gamma^+\gamma^5$, the quark helicity distribution Δ_q is obtained,

$$\Phi^{[\gamma^+\gamma^5]}(x) = \Delta q(x). \tag{2.46}$$

From this, the spin dependent structure function g_1 is obtained,

$$g_1(x) = \frac{1}{2} \sum_q e_q^2 \Delta q(x). \tag{2.47}$$

In addition to the two parton distribution function defined above, there is a third quark distribution function so-called *transversity* distribution denoted as h_1. The transversity distribution is obtained from the projection $\Gamma = i\sigma^{i+}\gamma^5 = \gamma^+\gamma^1\gamma^5$,

$$\Phi^{[i\sigma^{i+}\gamma^5]}(x) = h_1(x). \tag{2.48}$$

The transversity distribution $h_1(x)$ supplies, together with the unpolarized DF $f_1(x)$ and the helicity distribution $\Delta q(x)$, a complete picture of the nucleon in leading order shown in Fig. 2.5. $f_1(x)$ describes the unpolarized distribution, the helicity
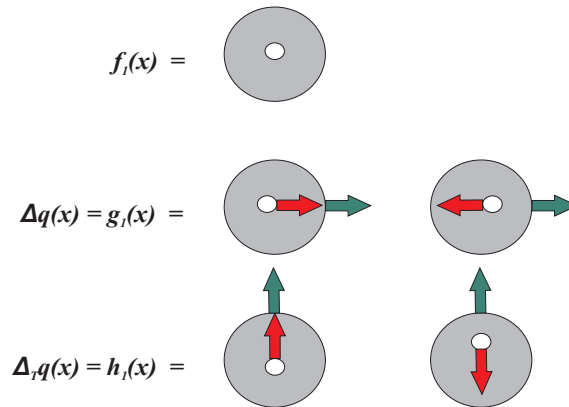

Figure 2.5: Probabilistic interpretation of leading order integrated PDFs.

distribution $\Delta q(x)$ describes longitudinally polarized quarks inside a longitudinally polarized nucleon and the transversity distribution h_1 describes transversely polarized quarks inside a transversely polarized nucleon [29].

2.2.2 Transversity

As explained before, the transversity distribution function describes transversely polarized quarks in transversely polarized nucleon. The scattering amplitude and the discontinuity that defines a distribution function are shown in Fig. 2.6. The quark
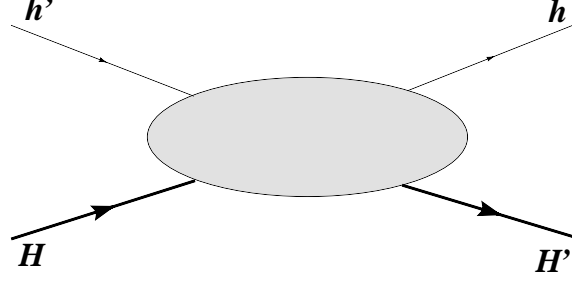

Figure 2.6: The forward scattering amplitude with helicities of quarks and hadrons.

(h, h') and hadron (H, H') helicities take on the values $\pm 1/2$. Helicity conservation requires $H + h' = H' + h$. Parity sends $h \to -h$ etc., and time reversal interchanges initial (H, h') and final (H', h) helicities. This leaves exactly three independent quark distribution functions corresponding to the helicity labels [30].

$$
\begin{aligned}
& \frac{1}{2} \quad \frac{1}{2} \quad \rightarrow \quad \frac{1}{2} \quad \frac{1}{2} \\
\frac{1}{2} \quad & -\frac{1}{2} \quad \rightarrow \quad \frac{1}{2} \quad -\frac{1}{2} \\
\frac{1}{2} \quad & -\frac{1}{2} \quad \rightarrow \quad -\frac{1}{2} \quad \frac{1}{2}.
\end{aligned}
\tag{2.49}
$$

These three helicity amplitudes can be grouped into combinations that measure spin average q, helicity difference Δq, and the transversity distribution h_1,

$$
\begin{aligned}
q \;\; &\leftrightarrow\;\; \left(\frac{1}{2} \;\; \frac{1}{2} \;\; \rightarrow \;\; \frac{1}{2} \;\; \frac{1}{2} \right) + \left(\frac{1}{2} \;\; -\frac{1}{2} \;\; \rightarrow \;\; \frac{1}{2} \;\; -\frac{1}{2} \right) \\
\Delta_q \;\; &\leftrightarrow\;\; \left(\frac{1}{2} \;\; \frac{1}{2} \;\; \rightarrow \;\; \frac{1}{2} \;\; \frac{1}{2} \right) - \left(\frac{1}{2} \;\; -\frac{1}{2} \;\; \rightarrow \;\; \frac{1}{2} \;\; -\frac{1}{2} \right) \\
h_1 \;\; &\leftrightarrow\;\; \left(\frac{1}{2} \;\; -\frac{1}{2} \;\; \rightarrow \;\; -\frac{1}{2} \;\; \frac{1}{2} \right)
\end{aligned}
\tag{2.50}
$$

The distributions q and Δ_q are the sum and difference, respectively, of the probability to find a quark polarized among and against the polarization of a nucleon in a helicity eigenstate. The transversity is off-diagonal in helicity and does not appear to have a probabilistic interpretation. Instead, in the basis of transverse spin eigenstates, h_1 can be interpreted as the probability to find a quark with its spin aligned along the transverse spin of the nucleon minus the probability to find it oppositely aligned. So the quark-hadron forward scattering amplitude that defines h_1, flips the chirality as well as the helicity of the quark. Since all perturbative QCD processes and all interactions with external electroweak currents conserve chirality, h_1 decouples

from all hard scattering processes that involve only one quark distribution function [31]. Therefore it is impossible to measure transversity in ordinary deep inelastic scattering.

2.2.3 Transverse Momentum Dependent (TMD) distribution functions

As seen before, the Parton distribution functions are obtained by projections of the integrated quark-quark correlation function (see Eq. (2.40)). The quark distribution functions which can be obtained from the integrated correlation function at leading twist were presented earlier. Now if the transverse momentum is taken into account (see Eq. (2.40)) in the hard process, other quark distributions can be defined.

The p_T dependent PDF is defined using projections of the un-integrated correlation function, which is defined as

$$\Phi^{[\Gamma]}(x, p_T) \equiv \frac{1}{2} \int dp^- Tr(\Phi(p, P, S)\Gamma). \tag{2.51}$$

Using this projected correlation function, the PDFs defined previously are rewritten at leading order in $1/Q$ as [32]:

$$\Phi^{[\gamma^+]}(x, p_T) = f_1(x, p_T^2) + \frac{\epsilon_T^{ij} p_{Ti} S_{Tj}}{M_N} f_{1T}^{\perp}(x, p_T^2) \tag{2.52}$$

$$\Phi[\gamma^+\gamma^5](x, p_t) = \lambda g_{1L}(x, p_T^2) + \frac{p_t \cdot S_T}{M_N} g_{1T}(x, p_T^2) \tag{2.53}$$

$$\Phi[i\sigma^{i+}\gamma^5](x, p_T) = S_T^i h_{1T}(x, p_T^2) + \frac{p_T^i}{M_N}\left(\lambda h_{1L}^{\perp}(x, p_T^2) + \frac{p_T \cdot S_T}{M_N} h_{1T}^{\perp}(x, p_T^2)\right)$$

$$+ \frac{\epsilon_T^{ij} p_{Ti}}{M_N} h_{1\perp}(x, p_T^2). \tag{2.54}$$

Within this picture the nucleon can be characterized by eight TMD quark distribution functions. The probabilistic interpretation of these distribution functions is as follows:

1. $f_1(x, p_T^2)$ describes the unpolarized quark distribution function,

2. $f_{1T}^{\perp}(x, p_T^2)$ describes the unpolarized quark inside a transversely polarized nucleon. It is called the Sivers function and has a nature of (naive) time-reversal odd (T-odd).

3. $g_{1L}(x, p_T^2)$ describes the helicity distribution function,

4. $g_{1T}(x, p_T^2)$ describes the distribution of longitudinally polarized quarks in transversely polarized nucleon,

5. $h_{1T}(x, p_T^2)$ describes quark transverse polarization along target transverse polarization,

6. $h_{1L}^\perp(x, p_T^2)$ describes quark transverse polarization along quark intrinsic transverse momentum in the longitudinally polarized target,

7. $h_{1T}^\perp(x, p_T^2)$ describes quark transverse polarization along quark intrinsic transverse momentum in the transversely polarized target,

8. $h_{1\perp}(x, p_T^2)$ describes quark transverse polarization along normal to the plane defined by quark intrinsic transverse momentum and nucleon momentum in the unpolarized target.

The helicity distribution Δq and the transversity distribution function h_1 introduced before are rewritten as [32]:

$$\Delta q(x, p_T^2) = g_{1L}(x, p_T^2), \tag{2.55}$$

$$h_1(x, p_T^2) = h_{1T}(x, p_T^2) + \frac{p_T^2}{2M_N} h_{1T}^\perp(x, p_T^2). \tag{2.56}$$

These transverse momentum dependent PDFs can be classified with the nucleon polarization state [32]. The quark-quark correlation function is expressed by separating the terms corresponding to unpolarized (O), longitudinal (L) and transversely (T) polarized target,

$$\Phi_O(x, p_T) = \left\{ f_1(x, p_T^2) + ih_1^\perp(x, p_T^2)\frac{\not{p}_T}{M} \right\} P_+ \tag{2.57}$$

$$\Phi_L(x, p_T) = \left\{ \lambda\Delta q(x, p_T^2)\gamma_5 + \lambda h_{1L}^\perp(x, p_T^2)\gamma_5\frac{\not{p}_T}{M} \right\} P_+ \tag{2.58}$$

$$\Phi_T(x, p_T) = \left\{ f_{1T}^\perp(x, p_T^2)\frac{\epsilon T_{\rho\sigma}p_T^\sigma S_T^\sigma}{M} + g_{1T}(x, p_T^2)\frac{p_T \cdot S_T}{M}\gamma_5 \right.$$
$$\left. + h_{1T}(x, p_T^2)\gamma_5\not{S} + h_{1T}^\perp(x, p_T^2)\frac{p_T \cdot S_T}{M}\gamma_5\frac{\gamma_5\not{p}_T}{M}\gamma_5 \right\} P_+. \tag{2.59}$$

The sum of these correlation functions gives the full spin structure of the nucleon,

$$\Phi(x, p_T) = \Phi_O(x, p_T) + \Phi_L(x, p_T) + \Phi_T(x, p_T). \tag{2.60}$$

In order to access these TMD distribution functions, DIS measurement with transversely polarized target is required. However, the transverse spin is naturally suppressed in high energy interaction since the transverse component of the spin is no longer eigenstate of transverse spin operator. Moreover it is expected that transverse momentum is very small compared to the nucleon momentum. Therefore the inclusive measurement does not provide an access to these distribution functions.

2.3   Semi-inclusive DIS

As explained in the previous section, transversity cannot be measured in inclusive DIS. In order to access the chiral-odd transversity function, it has to be combined

with another chiral-odd object. One of the possibilities is the semi-inclusive DIS process, where at least one produced hadron h with four-momentum P_h is detected in addition to the scattered lepton. Fig. 2.7 shows a schematic diagram of a semi-inclusive measurement. In addition to two scaling variables introduced in inclusive
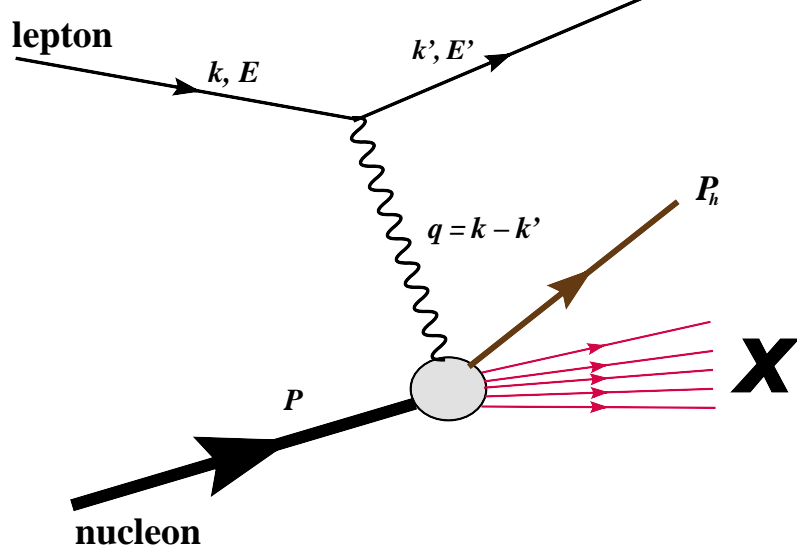

Figure 2.7: The basic diagram for deep-inelastic lepton hadron scattering. The virtual photon momentum is q. The final hadronic state is not measured and is denoted by X

DIS measurement (see Eqs. (2.2) and (2.3)), a third scaling variable z is introduced in semi-inclusive measurement, which describes the proportion of the photon energy carried by the detected hadron:

$$z = \frac{P \cdot P_h}{P \cdot q} =_{lab} \frac{E_h}{\nu}. \tag{2.61}$$

The semi-inclusive measurement allows us to access the transverse momentum dependent PDFs in DIS experiment. The quark parton model is extended by a fragmentation model introducing a set of new functions called *fragmentation functions* (FF) which allows to relate the appearance of certain hadrons h in the final state to the parton distribution functions for different flavors [33]. Fig. 2.8 shows the extended handbag diagram for semi-inclusive DIS. The quark fragmentation functions are derived from the quark-decay functions Δ.

2.3.1 Fragmentation Functions

The hadronic tensor explained in Eq. (2.39) is expanded with the decay function Δ as [34, 35]:

$$W_{\mu\nu}(q, P, S) = \sum_q e_q^2 \int \frac{d^4p}{(2\pi)^4} \frac{d^4k}{(2\pi)^4} \delta^{(4)}(p-q-k) Tr(\Phi(p, P, S)\gamma^\mu \Delta(k, P_h)\gamma^\nu \tag{2.62}$$
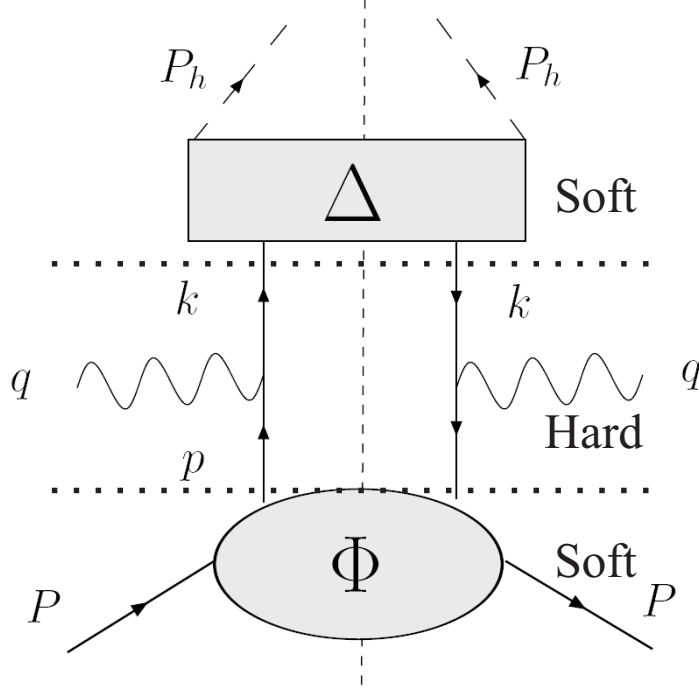
Figure 2.8: Extended handbag diagram for semi-inclusive DIS.

Here Φ is the correlation function as already defined in Eq. (2.38) and Δ is the new decay function, which is defined as [36]:

$$
\begin{aligned}
\Delta(k, P_h, S_h) \;=\; & \sum_X \frac{1}{(2\pi)^4} \int d^4 z e^{ik\cdot z} \\
& \times \langle 0|\psi_i(z)|P_h, S_h; X\rangle \langle P_h, S_h; X|\bar\psi_j(0)|0\rangle
\end{aligned}
\tag{2.63}
$$

The above equation describes the way in which the struck quark evolves into a hadronic final state in which the hadron h is detected. This process is called hadronization or fragmentation of the quark. Decomposition of Δ function in the basis of Dirac matrices including the final quark transverse momentum yields eight fragmentation functions in leading twist [37, 38]. However, after summation over the spin of the produced hadron, only two fragmentation functions remain, namely, the unpolarized FF $D_1^{q\to h}(z, P_{hT}^2)$ and the so-called Collins FF $H_1^{\perp q\to h}(z, P_{hT}^2)$ [39]. The index $q \to h$ indicates the fragmentation of a quark with flavor q into a hadron type h. These above twist-two FFs have probabilistic interpretation. The unpolarized FF is the probability density that a struck quark of flavor q with transverse momentum k_T fragments into a certain hadron of type h with energy fraction z, whereas the Collins FF is the difference of the probability densities for quarks with transverse spin states $\uparrow$ and $\downarrow$ to fragment into a hadron h, shown in Fig. 2.9
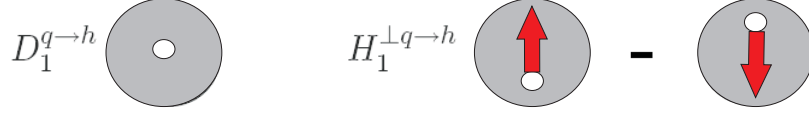
Figure 2.9: Leading twist transverse momentum dependent quark fragmentation functions independent of the produced hadron.

2.3.2 The SIDIS cross-section in terms of structure functions

Assuming single photon exchange, the lepton-hadron cross-section in SIDIS can be expressed in a model-independent way by a set of 18 structure functions [40, 41].

$$
\begin{aligned}
\frac{d\sigma}{dxdyd\psi dzd\phi_h dP_{h\perp}^2} =\ & \frac{\alpha^2}{xyQ^2}\frac{y^2}{2(1-\varepsilon)}\Big(1+\frac{\gamma^2}{2x}\Big) \\
& \times\Bigg\{ F_{UU,T} + \varepsilon F_{UU,L} + \sqrt{2\varepsilon(1+\varepsilon)}\cos\phi_h F_{UU}^{\cos\phi_h} \\
& + \varepsilon\cos(2\phi_h)F_{UU}^{\cos 2\phi_h} + P_{beam}\sqrt{2\varepsilon(1-\varepsilon)}\sin\phi_h F_{LU}^{\sin\phi_h} \\
& + S_L\Big[\sqrt{2\varepsilon(1+\varepsilon)}\sin\phi_h F_{UL}^{\sin\phi_h} + \varepsilon\sin(2\phi_h)F_{UL}^{\sin 2\phi_h}\Big] \\
& + S_L P_{beam}\Big[\sqrt{1-\varepsilon^2}\ F_{LL} + \sqrt{2\varepsilon(1-\varepsilon)}\ \cos\phi_h\ F_{LL}^{\cos\phi_h}\Big] \\
& + |S_T|\Big[\sin(\phi_h-\phi_S)\Big(F_{UT,T}^{\sin(\phi_h-\phi_S)} + \varepsilon F_{UT,L}^{\sin(\phi_h-\phi_S)}\Big) \\
& + \varepsilon\sin(\phi_h+\phi_S)F_{UT}^{\sin(\phi_h+\phi_S)} + \varepsilon\sin(3\phi_h-\phi_S)F_{UT}^{\sin(3\phi_h-\phi_S)} \\
& + \sqrt{2\varepsilon(1+\varepsilon)}\sin\phi_S F_{UT}^{\sin\phi_S} + \sqrt{2\varepsilon(1+\varepsilon)}\sin(2\phi_h-\phi_S)\ F_{UT}^{\sin(2\phi_h-\phi_S)}\Big] \\
& + |S_T| P_{beam}\Big[\sqrt{1-\varepsilon^2}\cos(\phi_h-\phi_S)F_{LT}^{\cos(\phi_h-\phi_S)} \\
& + \sqrt{2\varepsilon(1-\varepsilon)}\cos\phi_S F_{LT}^{\cos\phi_S} \\
& + \sqrt{2\varepsilon(1-\varepsilon)}\cos(2\phi_h-\phi_S)F_{LT}^{\cos(2\phi_h-\phi_S)}\Big]\Bigg\}
\end{aligned}
\tag{2.64}
$$

where α is the fine structure constant and the structure functions F_{sub}^{sup} on the right hand side depend on x, Q^2, z and P_T^h. The notations for the structure functions have the following meaning: the superscript correspond to azimuthal asymmetry described by given structure function whereas the first and second subscript indicate the respective polarization of beam and target and the third subscript specifies the polarization of the virtual photon. Integrating these structure functions over produced hadron momentum and summing up over all hadrons in the final state, one can find relations between the polarized SIDIS structure functions and ordinary

DIS structure functions [42].

The ratio ε of longitudinal and transverse photon flux in Eq. (2.64) is given by

$$\varepsilon = \frac{1 - y - \frac{1}{4}\gamma^2 y^2}{1 - y + \frac{1}{2}y^2 + \frac{1}{4}\gamma^2 y^2},\tag{2.65}$$

where $\gamma = \frac{2Mx}{Q}$. Using Eq. (2.65) the depolarization factors entering equation 2.64 can be written as [40]:

$$\frac{y^2}{2(1-\epsilon)} = \frac{1}{1+\gamma^2}(1 - y + \frac{1}{2}y^2) + \frac{1}{4}\gamma^2 y^2 \approx (1 - y + \frac{1}{2}y^2),\tag{2.66}$$

$$\frac{y^2}{2(1-\epsilon)}\epsilon = \frac{1}{1+\gamma^2}(1 - y - \frac{1}{4}\gamma^2 y^2) \approx (1 - y),\tag{2.67}$$

$$\frac{y^2}{2(1-\epsilon)}\sqrt{2\epsilon(1+\epsilon)} = \frac{1}{1+\gamma^2}(2 - y)\sqrt{1 - y - \frac{1}{4}\gamma^2 y^2} \approx (2 - y)\sqrt{1 - y}\tag{2.68}$$

$$\frac{y^2}{2(1-\epsilon)}\sqrt{2\epsilon(1+\epsilon)} = \frac{1}{\sqrt{1+\gamma^2}}y\sqrt{1 - y - \frac{1}{4}\gamma^2 y^2} \approx y\sqrt{1 - y},\tag{2.69}$$

$$\frac{y^2}{2(1-\epsilon)}\sqrt{1-\epsilon^2} = \frac{1}{\sqrt{1+\gamma^2}}y(1 - \frac{1}{2}y) \approx y(1 - \frac{1}{2}y).\tag{2.70}$$

2.4 Target transverse spin dependent asymmetries

For a hadron produced in the current fragmentation region of SIDIS, the cross-section is a convolution of initial quark distribution in the nucleon, defined as,

$$d\sigma^{l+N \to l'+h+X} \propto DF \otimes d\sigma^{l+q \to l'+q'} \otimes FF.\tag{2.71}$$

Here $d\sigma^{l+q \to l'+q'}$ is the polarized lepton-quark elastic hard scattering cross-section and the symbol $\otimes$ stands for convolution over quark intrinsic transverse momentum. As one can see from the general expression (see Eq. (2.64)), there are only eight possible target transverse polarization S_T dependent azimuthal modulations, with five single target spin and three double spin. These azimuthal modulations are combined with eight independent structure functions. Using Eq. (2.71), each structure function can be written independently as a convolution of eight transverse momentum dependent distribution functions (explained in section 2.2.3) and two fragmentation functions (explained in section 2.3.1). Within the leading order QCD parton model calculations, the structure functions entering in the amplitudes of target transverse polarization dependent azimuthal modulations are given by the following convolutions:

$$F_{UT}^{\sin(\phi_h - \phi_s)} \propto f_{1T}^{\perp q} \otimes D_1^{q \to h},\tag{2.72}$$

$$F_{UT}^{\sin(\phi_h + \phi_s)} \propto h_1^q \otimes H_1^{\perp\, q \to h},\tag{2.73}$$

$$F_{LT}^{\cos(\phi_h - \phi_s)} \propto g_{1T}^q \otimes D_1^{q \to h},\tag{2.74}$$

$$F_{UT}^{\sin(3\phi_h - \phi_s)} \propto h_{1T}^{\perp q} \otimes H_1^{\perp\, q \to h}.\tag{2.75}$$

Whereas the spin independent part of the cross section is given by

$$F_{UU,T} \propto f_1^q \otimes D_1^{q \to h}. \tag{2.76}$$

Eqs. (2.72) to (2.75) defines the four leading twist modulations, out of which $\sin(\phi_h - \phi_s)$ and $\sin(\phi_h + \phi_s)$ modulations describe the Sivers [43] and Collins effect [39] respectively. The other two leading twist modulations give us access to DFs g_{1T}^q and $h_{1T}^{\perp q}$.

Within the QCD parton model, the non-zero contributions arise also for the remaining 4 azimuthal modulations at twist-three level. It is important to note that using only twist-two DFs and FFs and taking into account the order $|\mathbf{k}_T|/Q$ kinematic corrections, one also obtain the nonzero contributions to all these asymmetries [42]. This approximation was successfully used to describe the (twist-three) Cahn effect in unpolarized SIDIS [44] and provide predictions for the $\cos(\phi_h)$ dependence of SIDIS A_{LL} asymmetry [45]. Within this approximation, the remaining four structure functions are defined as:

$$F_{LT}^{\cos(\phi_s)} \quad \propto \quad \frac{M}{Q} g_{1T}^q \otimes D_1^{q \to h}, \tag{2.77}$$

$$F_{LT}^{\cos(2\phi_h - \phi_s)} \quad \propto \quad \frac{M}{Q} g_{1T}^q \otimes D_1^{q \to h}, \tag{2.78}$$

$$F_{UT}^{\sin(\phi_s)} \quad \propto \quad \frac{M}{Q} \left(h_1^q \otimes H_1^{\perp \, q \to h} + f_{1T}^{\perp q} \otimes D_1^{q \to h} \right), \tag{2.79}$$

$$F_{UT}^{\sin(2\phi_h - \phi_s)} \quad \propto \quad \frac{M}{Q} \left(h_{1T}^{\perp \, q} \otimes H_1^{\perp q \to h} + f_{1T}^{\perp q} \otimes D_1^{q \to h} \right). \tag{2.80}$$

Note that the convolutions in these equations include different combinations of intrinsic transverse momentum of quarks in nucleon. The complete definition of all convolutions presented here can be found in [40].

For the target transverse polarization dependent azimuthal modulations given in Eqs. (2.72) - (2.80), except the usual spin independent cross-section, all terms are expressed with sin or cos terms with different combination of azimuthal angles. Those are expressed with a Fourier expansion. Thus they are naturally orthogonal functions and can be disentangled without interference between the terms.

2.4.1 Definition of asymmetries

All eight cross-sections corresponding to target transverse spin dependent azimuthal asymmetries defined earlier, are measurable quantities to provide data which can be interpreted, for example, within the QCD parton model. There are five single spin asymmetries or UT asymmetries and three double spin asymmetries or LT asymmetries. For a shorthand notation, lets consider the eight target transverse

spin dependent azimuthal asymmetries as:

$$w_1(\phi_h, \phi_s) = \sin(\phi_h - \phi_s), \tag{2.81}$$
$$w_2(\phi_h, \phi_s) = \sin(\phi_h + \phi_s), \tag{2.82}$$
$$w_3(\phi_h, \phi_s) = \sin(3\phi_h - \phi_s), \tag{2.83}$$
$$w_4(\phi_h, \phi_s) = \sin(\phi_s), \tag{2.84}$$
$$w_5(\phi_h, \phi_s) = \sin(2\phi_h - \phi_s), \tag{2.85}$$
$$w_6(\phi_h, \phi_s) = \cos(\phi_h - \phi_s), \tag{2.86}$$
$$w_7(\phi_h, \phi_s) = \cos(\phi_s), \tag{2.87}$$
$$w_8(\phi_h, \phi_s) = \cos(2\phi_h - \phi_s) \tag{2.88}$$

In general, the asymmetries are parameterized by the ratio of convolutions of spin-dependent to spin-independent DFs and FFs, which can be written separately for UT and LT asymmetries:

$$A_{UT}^{w_i(\phi_h,\phi_s)} \equiv \frac{F_{UT}^{w_i(\phi_h,\phi_s)}}{F_{UU,T}}, A_{LT}^{w_i(\phi_h,\phi_s)} \equiv \frac{F_{LT}^{w_i(\phi_h,\phi_s)}}{F_{UU,T}}. \tag{2.89}$$

The cross-section can be represented as:

$$d\sigma(\phi_h, \phi_s, ...) \quad \propto \quad (1 + |\mathbf{S}_T| \sum_{i=1}^{5} D^{w_i(\phi_h,\phi_s)} A_{UT}^{w_i(\phi_h,\phi_s)} w_i(\phi_h, \phi_s)$$
$$+ \quad P_{beam} |\mathbf{S}_T| \sum_{i=6}^{8} D^{w_i(\phi_h,\phi_s)} A_{LT}^{w_i(\phi_h,\phi_s)} w_i(\phi_h, \phi_s) + ...). \tag{2.90}$$

Here $D^{w_i(\phi_h,\phi_s)}$ represents the depolarization factor, which are calculated for all asymmetries from Eqs. (2.66) - (2.70). Thus calculated depolarization factors are:

$$D^{\sin(\phi_h-\phi_s)}(y) = 1, \tag{2.91}$$
$$D^{\sin(\phi_h+\phi_s)}(y) = D^{\sin(3\phi_h+\phi_s)}(y) = \frac{2(1-y)}{1+(1-y)^2}, \tag{2.92}$$
$$D^{\sin(2\phi_h-\phi_s)}(y) = D^{\sin(\phi_s)}(y) = \frac{2(2-y)\sqrt{1-y}}{1+(1-y)^2}, \tag{2.93}$$
$$D^{\cos(\phi_h-\phi_s)}(y) = D(y) = \frac{y(2-y)}{1+(1-y)^2}, \tag{2.94}$$
$$D^{\cos(2\phi_h-\phi_s)}(y) = D^{\cos(\phi_s)}(y) = \frac{2y\sqrt{1-y}}{1+(1-y)^2}. \tag{2.95}$$

The counting rate asymmetries extracted from the data as amplitudes of corresponding azimuthal modulations (raw asymmetries) are then given by

$$A_{UT,\,raw}^{w_i(\phi_h,\phi_s)} = D^{w_i(\phi_h,\phi_s)}(y)f|S_T|A_{UT}^{w(\phi_h,\phi_s)}, \quad (i=1,5), \tag{2.96}$$
$$A_{LT,\,raw}^{w(\phi_h,\phi_s)} = D^{w(\phi_h,\phi_s)}(y)fP_{beam}|S_T|A_{LT}^{w(\phi_h,\phi_s)}, \quad (i=6,8), \tag{2.97}$$

where f is the target polarization dilution factor. All these asymmetries are measured at COMPASS with a transversely polarized target. After a brief introduction about the COMPASS experiment in Chapter3, extraction of eight target transverse spin dependent asymmetries is discussed extensively in Chapter 4.

Chapter 3

The COMPASS Experiment

> "Experimental science is the
> queen of sciences and the goal of
> all speculation."
>
> Roger Bacon

COMPASS[1] [1] is a fixed target experiment on the M2 beam-line of the SPS[2] at CERN[3] (European Council for Nuclear Research), on the France-Switzerland border near Geneva. Fig. 3.1 gives an overview of the accelerator complex at CERN. A polarized beam and a polarized target are prerequisites to measure all the terms in DIS[4] cross-section. Some aspects of the polarized muon beam used in the COMPASS experiment are discussed in section 3.1 followed by an introduction to the setup of the polarized target in section 3.3. The overall design of the COMPASS spectrometer is described in section 3.4, whereas the detectors used for track reconstruction are discussed in section 3.5. The detectors used for particle identification are discussed in section 3.6. Section 3.7 explains the trigger system used in COMPASS. Readout concept and data analysis is discussed in sections 3.8 and 3.9 respectively. A detailed description of the COMPASS experiment can be found in [46].

3.1 The SPS 160 GeV polarized muon beam

The M2 beamline can provide different types of beams that are produced from the SPS protons. Pions, kaons, protons and muons can be used to perform different

---

[1]**CO**mmon **M**uon **P**roton **A**pparatus for **S**tructure and **S**pectroscopy
[2]**S**uper **P**roton **S**ynchroton
[3]**C**onseil **E**uropen pour la **R**echerche **N**uclaire
[4]**D**eep **I**nelasitc **S**cattering

measurements that are foreseen with the COMPASS experiment. The M2 beamline (Fig. 3.2) has always been a dedicated muon beamline but by removing the hadrons absorbers and re-tuning the magnets, the beamline can be used to transport secondary hadrons up to 300 GeV. The common origin for the muon beams and the hadron beams lies in the SPS at CERN as a source of high energy protons of up to 450 GeV. These protons are typically extracted from SPS into M2 beamline [47] during a 4.8 s extraction time ("spill") in a 16.8 s cycle.

The accelerated protons are transported to the T6 production target made of beryllium where charged pions and kaons are produced along with muons [48]. It is possible to set the intensity of the muon beam by adjusting the length of the production target. For an intensity of $2.8 \cdot 10^8$ μ^+ per spill a target length of 500 mm is used. Shorter targets are used in order to get low intensity beams [49].

The secondary charged pions and kaons which have been produced in the T6 target can be separated from protons by a set of bending magnets. The scrapers which are specially designed collimators made out of 5 m long magnetized iron blocks are used to deflect low momentum particles away from the beam, selecting a momentum band of about $\pm 10\%$ around a central value of $p_{\pi,K} = 177$ Gev/c. In the beam of about 177 GeV/c, the hadronic part consists of 65.9% protons, 3.4% K^+ and 30.7% π^+.

Among other particles, pions and kaons are produced, that decay into muons and neutrinos in the 600 m long decay channel equipped with alternatively focusing and de-focussing (FODO) quadruple magnets. The pions and kaons which remain after passing the decay channel are removed by a hadron absorber of length 9.9 m, which is made of beryllium. The absorber housed in the bending dipole B4, together with another dipole magnet B5 is responsible for bending the muon beam, which, at this point is at about 15 m underground towards the experimental hall situated on the surface of the earth. This procedure together with the following scrapper elements, selects muons with a momentum of p_μ=160 GeV/c with a momentum spread usually between $\pm 3\%$ and $\pm 5\%$ RMS.

The polarization of the muon is naturally obtained which is based on the parity violation in the weak decay of the charged pions or kaons [50]. The polarization of the muon depends on the decay angle in the pion or kaon rest frame with respect to its direction of motion in the lab frame (see Fig. 3.3).The sign and degree of the muon polarization can be chosen by selecting the corresponding muon energy [51]. In order to optimize flux and energy of the muon beam, forward muons were chosen for COMPASS, which are negatively polarized.

The polarization P_μ of the muon in the lab frame is given by

$$P_\mu = -\frac{m_{\pi,K}^2 + (1 - \frac{2E_{\pi,K}}{E_\mu})m_\mu^2}{m_{\pi,K}^2 - m_\mu^2}, \tag{3.1}$$

with m_μ and E_μ being mass and energy of the muon that has been produced in the decay, and mass $m_{\pi,K}$ and energy $E_{\pi,K}$ of the decaying pion and kaon [52, 53]. The spot size of the beam at the COMPASS target defines the diameter of the target cells, which should be as small as possible in order to avoid the multiple scattering of
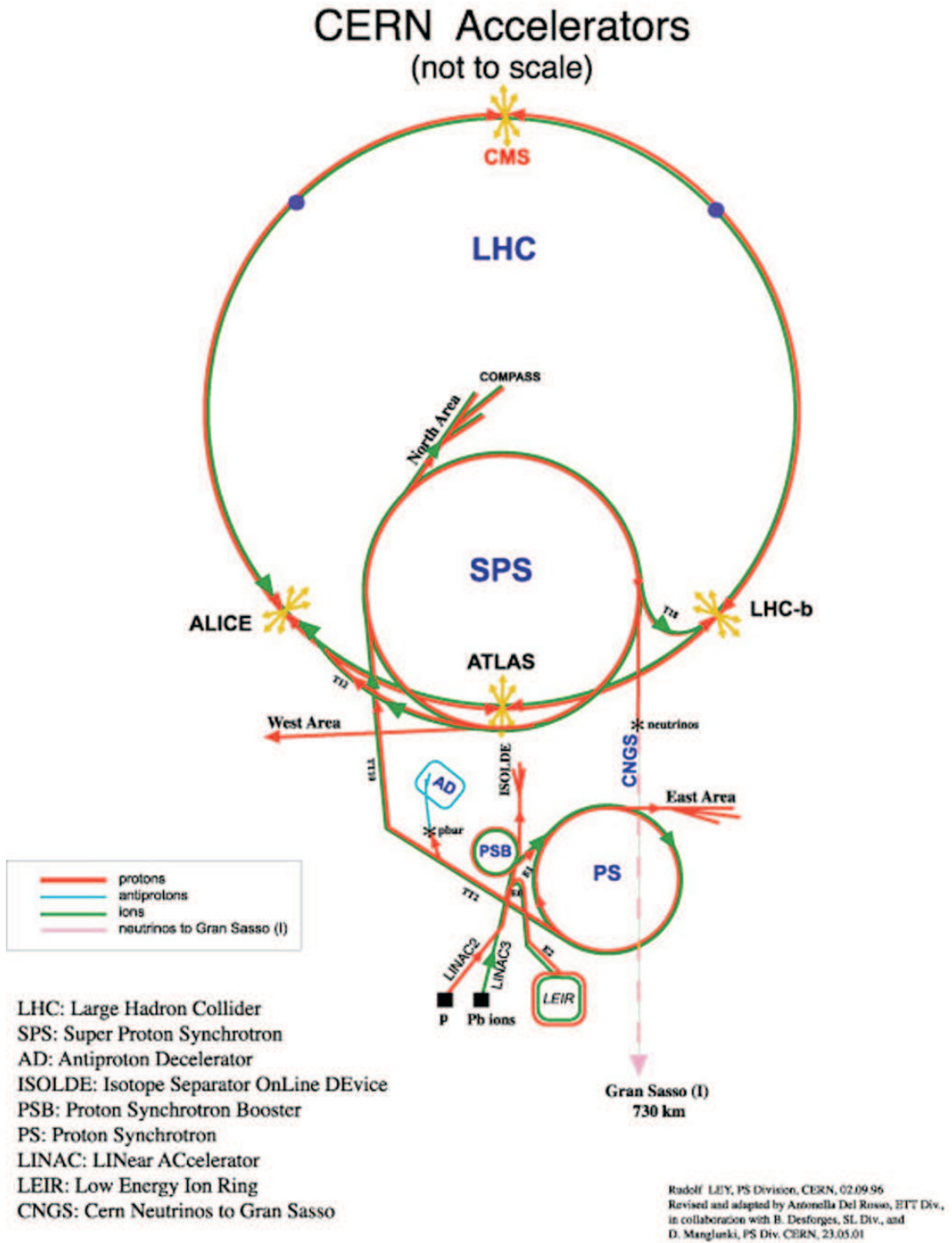
Figure 3.1: The CERN accelerator complex. LINAC 2 and 3 are the injectors for protons and ions respectively. Via PS booster and PS they are transferred to the SPS, where they are extracted to the north area for different experiments, like COMPASS.
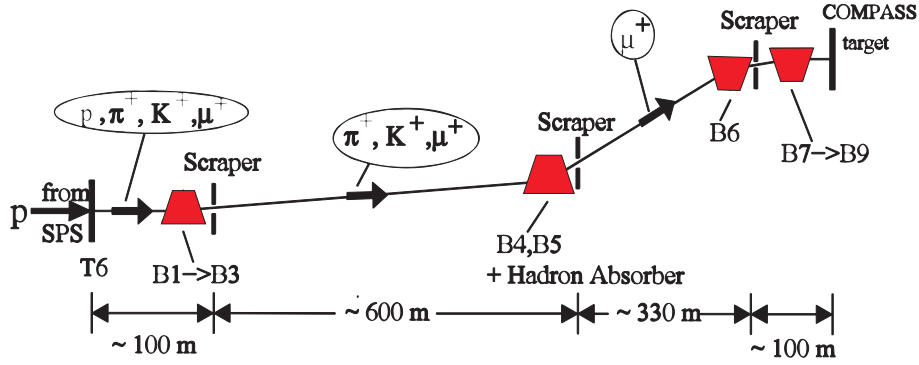
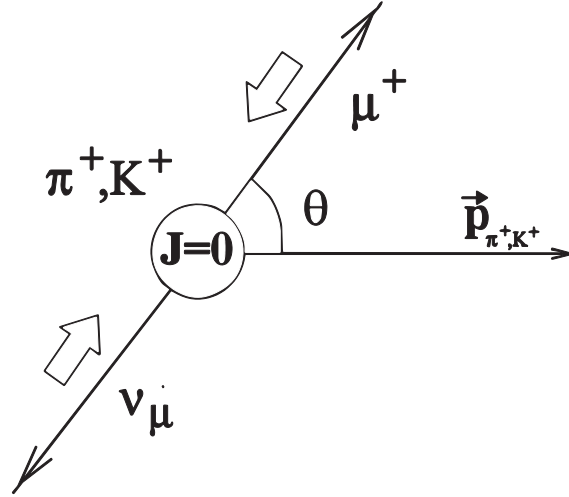Figure 3.2: The sideview of M2 beam-line that provides muon beam to COMPASS experiment

Figure 3.3: The decay of charged pions and kaons. Due to helicity conservation, lepton number conservation and the fact that neutrinos have helicity -1, positive muons, which were produced in the forward direction relative to the parent particle's momentum, are polarized anti parallel to their momentum in the lab frame

the produced particles for efficient mass reconstruction of the short living hadrons. The Typical beam size is about $\sigma_x \sim \sigma_y \sim 8$ mm, which has been considerably reduced compared to that in the SMC experiment($\sigma \sim 16$mm). The beam parameters for the year 2004 beam-time are summarized in the following Table. 3.1.

3.2   Measurement of the muon beam momentum

Measurement of the momentum of each individual muon is achieved by the Beam Momentum Station (BMS) situated about 100 m upstream of the COMPASS target.

Beam parameters	Measured
Beam momentum $(p_\mu)/(p_\pi)$	160 GeV/c/172 GeV/c
Proton flux on T6 per SPS cycle	$1.2 \cdot 10^{13}$
Focussed muon flux per SPS cycle	$2 \cdot 10^8$
Beam polarization	$(-80 \pm 4)\%$
Spot size at COMPASS target $(\sigma_x \times \sigma_y)$	8×8 mm^2
Divergence at COMPASS target $(\sigma_x \times \sigma_y)$	0.4×0.8 mrad
Muon halo within 15 cm from beam axis	16%
Halo in experiment $(3.2 \times 2.5$ m$^2)$ at $\lvert x, y\rvert > 15$ cm	7%

Table 3.1: Parameters and performance of the 160 GeV/c muon beam in 2004.

Fig. 3.2 shows the setup of the BMS. The three consecutive dipole magnets (B6) deflect and bring the muon beam close to the horizontal direction before entering the experimental hall. The B6 dipoles are surrounded by a set of four quadruples (Q29, Q30, Q31, Q32) and six beam momentum stations(BM01, BM02, BM03, BM04, BM05, BM06). Out of these, BMS stations BM01 - BM04 are scintillator
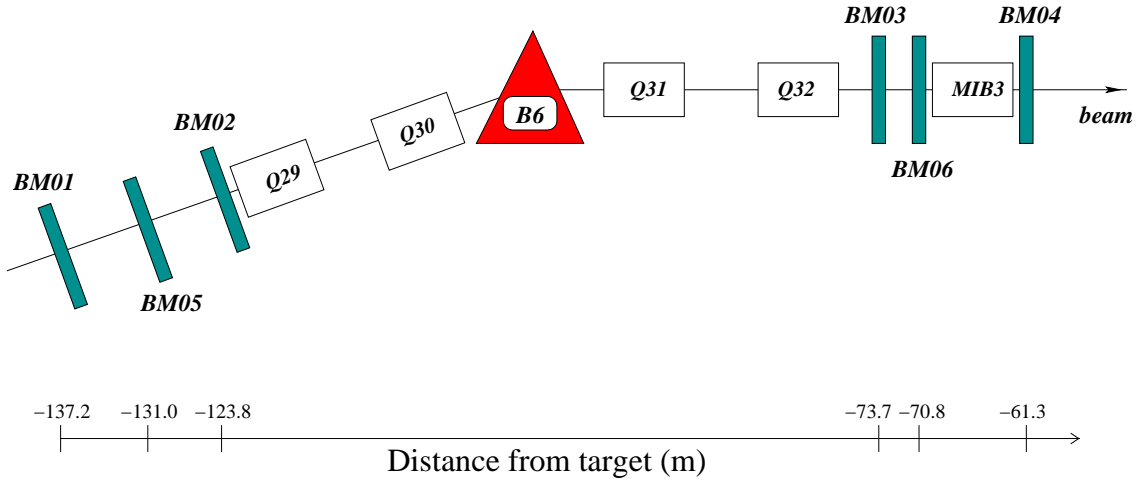
Figure 3.4: Layout of the Beam Momentum Station for the COMPASS muon beam.

hodoscopes with horizontal strips previously used in the SMC experiment. Each hodoscope is composed of 64 scintillator elements of 5 mm width in the dispersive (vertical plane) and 20 mm thickness ensuring a large output signal. In the central region, the scintillator strips are divided horizontally so that the particle flux per element does not exceed $1 \cdot 10^7$ s^{-1} even for the maximum intensity beam. The read out is done using single channel fast photomultiplier tubes with a time resolution of typically 0.3 ns. This setup was supplemented by two more planes namely BM05 and BM06 to resolve ambiguities. The BM05 station was mounted halfway between the stations BM01 and BM02, whereas BM06 was mounted between stations BM03 and BM04. These two extra planes provide the additional redundancy in the track

between the beam momentum stations and the detectors in front of the target.
The geometry of the BM05 plane is similar to that of the original planes apart from
the 2.5 mm pitch. It consists of 64 channels of two adjacent stacks of scintillating
fibre hodoscope. In addition, BM06 plane was included which possesses 128 chan-
nels, all made out of single stacks of scintillating fibre hodoscope. The design was
chosen such that the maximum rate per channel does not exceed $3 \cdot 10^6$ s^{-1}, with a
pitch of 1.25 mm. The two new stations use the same multi-anode photomultiplier
technology, similar to the one used for the scintillating fibre stations. There were
further modifications done to the setup for the data taken in 2004. Considering
the age of the initial BMS setup (BM01 - BM04), spare parts for the electronics
were no longer available, which lead to a refurbishment of the electronics of sta-
tions BM01 - BM04, increasing the overall beam detection efficiency. The purity of
the beam momentum station information and the efficiency were improved further
during the event reconstruction by backtracking the information obtained by the
tracking detectors located in front of the target.

3.3 The polarized target

With the small cross-section for muon scattering and the given beam intensity, the
high luminosity required for the physics programme of the COMPASS experiment
is achieved by using thick solids state targets.
The target material used for the measurements of the spin structure of proton and
deuteron are NH_3 and ^{6}LiD, but so far the COMPASS experiment has taken data
with the ^{6}LiD target material [54]. The ^{6}Li nucleus can be considered to large extent
as He+D system, see [55]. Therefore the ^{6}LiD might be described as two polarizable
(spin 1) deuterons and unpolarized (spin 0) helium core. The total amount of the
polarizable material is approximately 50% (4 out of 8 nucleons).
The polarization of the target material is achieved by using a special technique
called as Dynamic Nuclear Polarization (DNP) [56], where the electron polarization
is transferred to nuclear spins by means of a microwave field.

3.3.1 Construction and operation

The COMPASS polarized target, shown in Fig. 3.5, was previously used by the SMC
experiment [57] [58], refurbished with extra elements to meet the requirements for
COMPASS experiment. The target material is contained in two independently po-
larized cylindrical target cells of 60 cm length and 3 cm diameter, installed one after
the other along the beam inside the mixing chamber of a ^{3}He - ^{4}He dilution refrig-
erator [59]. The two target cells are exposed to the same muon flux, ensuring that
the measured asymmetries are independent of the flux. Thus in the measurement
of possible false asymmetries are reduced. The target cells are labeled according to
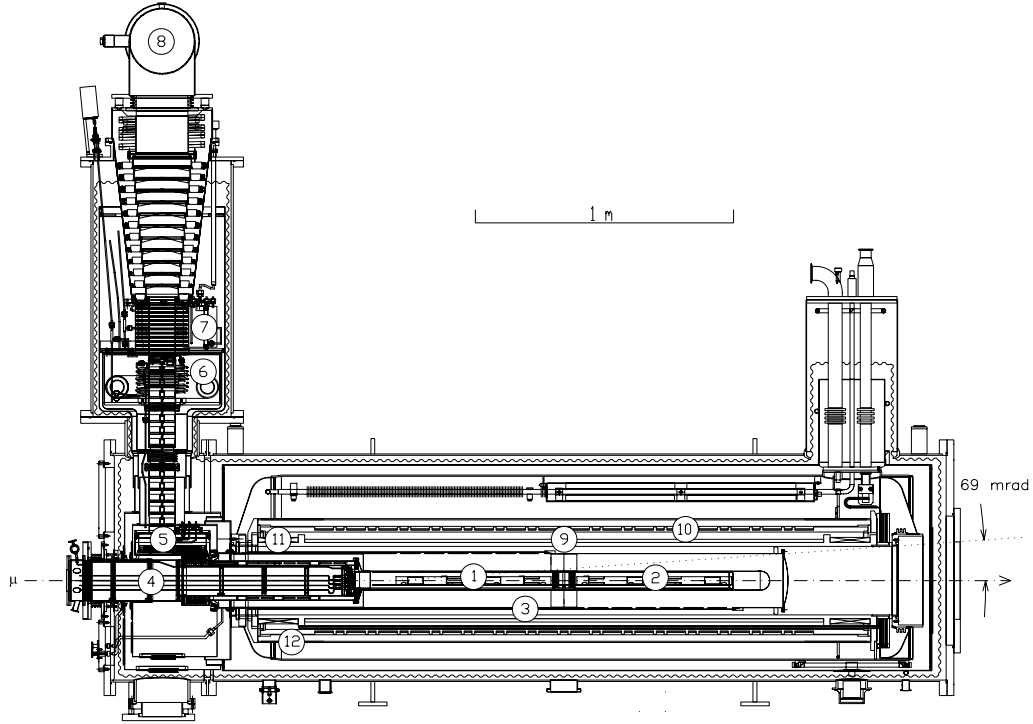their position relative to the beam direction as upstream and downstream cell.

Figure 3.5: Side view of the COMPASS polarized target: (1) upstream target cell and (2) downstream target cell inside mixing chamber, (3) microwave cavity, (4) target holder, (5) still (^{3}He evaporator), (6) ^{4}He evaporator, (7) ^{4}He liquid/gas phase separator, (8) ^{3}He pumping port, (9) solenoid coil, (10) correction coils, (11) end compensation coil, (12) dipole coil. The muon beam enters from the left. The two halves of the microwave cavity are separated by a thin microwave stopper.

During the DNP the dilution refrigerator provides a temperature of about 0.4 K. After the desired polarization state is achieved, the polarizing process is stopped and the spin configuration is frozen by cooling the target material to 50 mK. Taking advantage of the long relaxation time (exceeding 1000 h), the target can then be used with the desired polarization. A mixing chamber is placed inside a microwave cavity which provides the necessary radiation for DNP process. There are separate microwave systems available for each of the two target cells, because two different frequencies are needed for two target cells which are oppositely polarized. The polarization is constantly monitored by NMR coils along each of the cells. Typical polarizations are about 50%. Fig. 3.6 shows a typical average polarization in the upstream and downstream target cells during 20 days of the 2004 run.
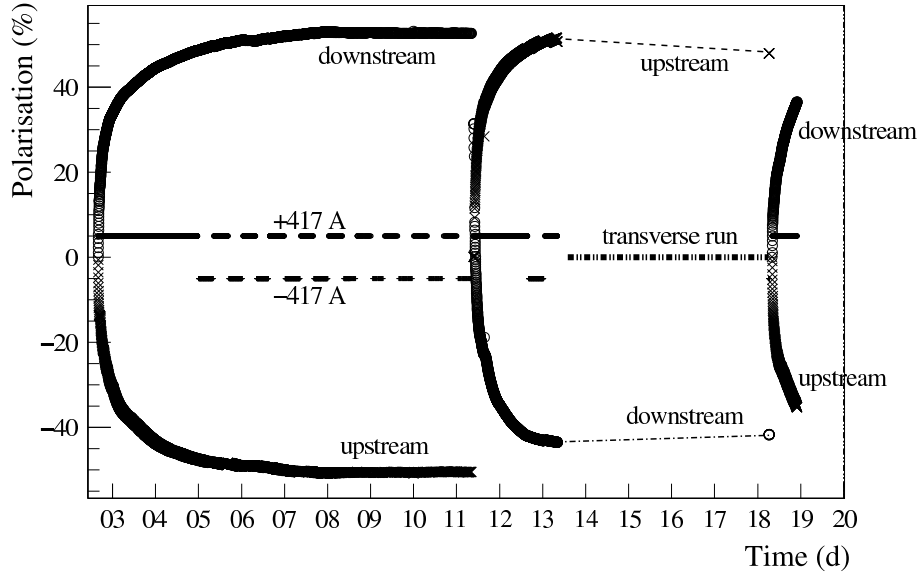
Figure 3.6: Typical average polarizations in the upstream and downstream target cells during 20 days of the 2004 run. After day 11, the polarizations in the target cells are reversed by changing the microwave frequencies. Data are taken in transverse mode from day 13 to day 18 and a new field reversal by microwaves is performed at the end of the period. The current of ± 417 A corresponds to an axial field of 2.5 T.

3.3.2 Transverse polarization

During data acquisition in transverse mode. the target material is kept in frozen spin mode below 90 mK and the spin direction is maintained by the 0,42 T transverse dipole field. The polarization is reversed by exchanging the microwave frequencies of the two cells.

The data for the measurement of the target transverse spin asymmetries analysis, discussed in Chapter 4 of this thesis, were taken in the transverse target configuration.

3.4 The COMPASS spectrometer

The COMPASS experimental setup consists of a two-stage forward magnetic spectrometer, a Large Angle Spectrometer (LAS) and a Small Angle Spectrometer (SAS), imposing capabilities of operation at high luminosity of high beam intensity, counting rates, large angular and dynamic acceptances, which are requirements for the proposed muon programme and other physics programmes.

The basic layout of the COMPASS spectrometer as it was used for obtaining 2004 data is shown in Fig. 3.7. Both the setup, LAS and SAS are located
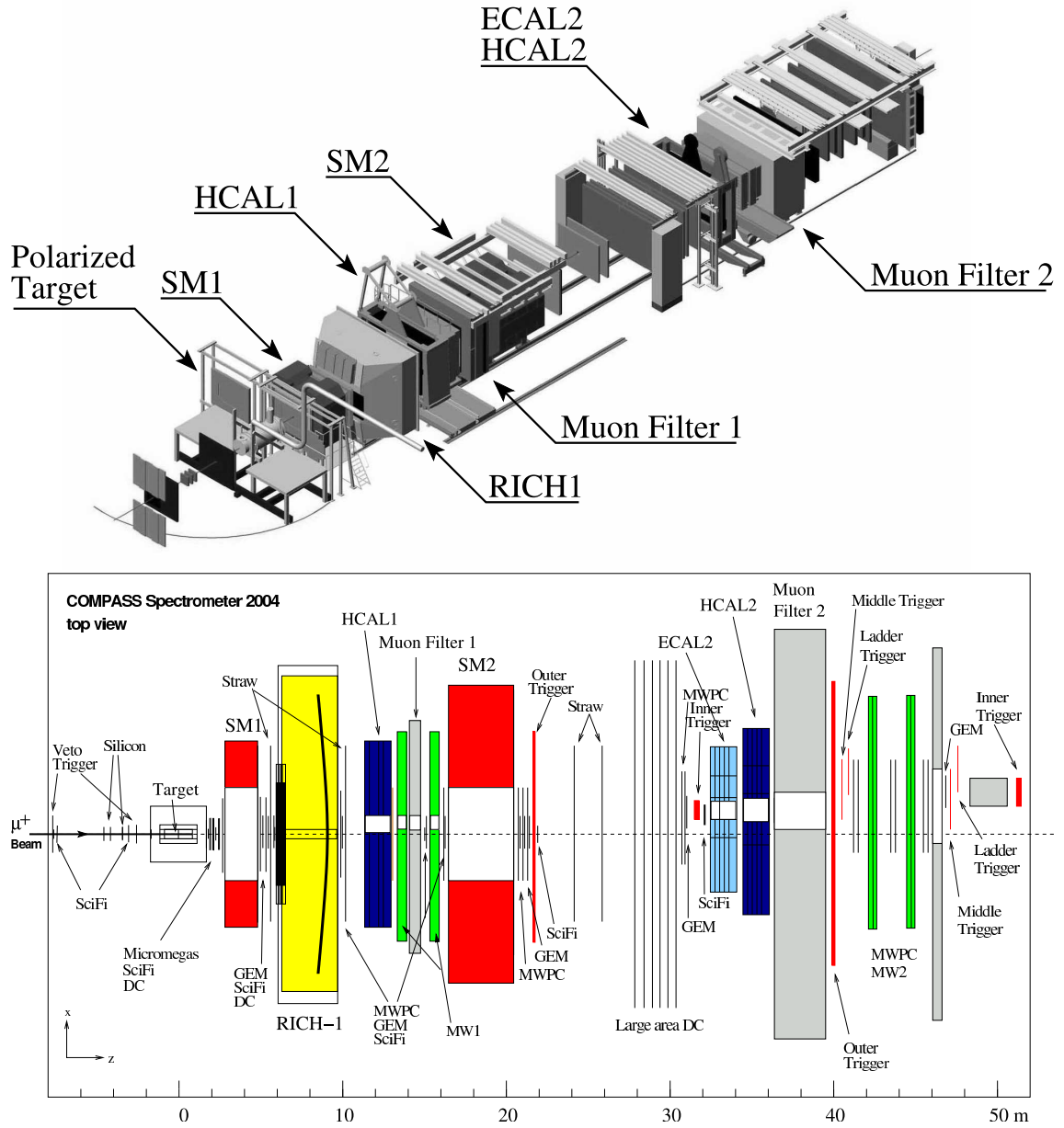
Figure 3.7: Compass 2004 muon setup (top) artistic view, (bottom) top view (for detector names, see text).

downstream of the target, extends over a total length of 50 m. Each of the two spectrometers is equipped with an analyzing magnet surrounded by tracking detectors and completed by a hadron calorimeter and by a muon filter for muon identification. Due to the flexibility required by the broad spectrum of the COMPASS physics programme, all the detectors involved are mounted on rails allowing to position them at variable distances from the target.

3.4.1 Large angle spectrometer

The Large Angle Spectrometer (LAS) has been designed for the detection of tracks with large angle up to about 180 mrad polar acceptance and with low momenta. It is built around the spectrometer dipole magnet SM1 surrounded by tracking detectors. SM1 is a dipole magnet situated 4 m downstream of the target. The pole tips of the SM1 magnet are wedge shaped, where the apex of the edge is facing the target making sure that the tracks pointing to the target are orthogonal to the field lines of the magnet.
The field integral of the magnet is measured to be 1.0 Tm, leading to a deflection of 300 mrad for particles with a momentum of 1 GeV/c. Considering the bending power of SM1, the tracking detectors involved in LAS need to have an angular acceptance of ± 250 mrad in the horizontal plane.
A RICH detector used for particle identification follows the SM1. It possess large transverse dimensions to match the LAS acceptance. It is used to identify the charged hadrons with momenta ranging from a few GeV/c to 43 GeV/c. It is followed by a hadron calorimeter with a central hole matching the second spectrometer magnet (SM2) acceptance. The LAS is completed by a muon filter, which is a device to distinguish between the hadronic products from the muons.

3.4.2 Small angle spectrometer

The Small Angle Spectrometer (SAS) setup detects the tracks with angles in the range of ± 30 mrad and with momenta of 5 Gev/c and higher. Similar to the LAS setup, the SAS is built around an another spectrometer dipole magnet SM2, located 18 m downstream of the target. SM2 has a total field integral of 4.4 Tm. SM2 is followed up with an electronic and a hadronic calorimeter and a muon filter which has a hole in the center covering the acceptance of the inner trigger.

3.5 Detectors for track reconstruction

In the overall spectrometer acceptance, the particle flux varies significantly in different regions. The detectors used for track reconstruction must possess a high particle

rate capability with an excellent space resolution. In order to avoid multiple scattering and secondary interactions, the amount of material used in every detector has to remain at minimum level. These requests are very severe in the upstream area of the SM1 magnet, where the particle flux is at maximum due to the large number of low energy secondary particles coming from the target. Whereas, for the detectors situated far from the beam, the space resolution constraint can be relaxed obtaining unchanged angular resolution but the area covered must be large.

As a result of the varying demands, a wide variety of detectors are deployed in COMPASS. The tracking detectors are grouped into three groups according to the angular range in which they operate.

- Very Small Area Trackers (VSAT) - situated directly in the beam area for the detection of the particles at very small angles. These detectors are small in size, require very good time-resolution and short dead-time because of the high flux they have to withstand. In addition, as they are in the area around the target, they must also possess a good spatial resolution of about 50 μm. These duties are taken care by eight scintillating fibre stations in and around the beam with excellent time resolution [60], and by three stations of double-sided silicon micro-strip detectors with high spatial resolution [61].

- Small Area Trackers (SAT) - used to detect particles deflected at slightly larger angles. These detectors must possess high space resolution but the requirement for good time resolution is relaxed. These requirements are satisfied by three Micromegas (Micromesh Gaseous Structure) stations [62, 63] and eleven GEM (Gas Electron Multipliers) stations [64, 65]. Both Micromeagas and GEM detectors have central dead zone with a diameter of 5 cm.

- Large Area Trackers (LAT) - particles deflected at greater angles are detected by these detectors. These detectors must have a good space resolution and must cover a large area defined by the experimental setup acceptance. Three drift chambers (DC), followed by three stations of straw drift tubes [66] and by 14 multi-wire proportional chamber (MWPC) stations, satisfy the requirements needed for large area tracking.

A detailed description of the various detectors mentioned above can be found in [46].

3.6 Detectors for particle identification

The various detectors discussed in previous sections were used to measure points in space and time, together with the information of particle tracks obtained from the fields of spectrometer magnets SM1 and SM2. However to be able to distinguish particles of different types, the information on their energy is needed. For that the COMPASS spectrometer includes several particle identification detectors. A RICH detector located in the first spectrometer separates outgoing hadrons into pions,

kaons and protons ranging up to a momenta as large as 43 GeV/c. Two hadron calorimeters, HCAL1 and HCAL2 measure the scattered hadron energy and initiate a trigger signal. An electronic calorimeter, ECAL2 measures the energies of the photons and electrons emitted at small angles. Finally the "Muon Wall" system namely MW1 and MW2 detects the scattered muons both in LAS and SAS.

3.6.1   The RICH detector

According to the Cerenkov effect, when a charged particle goes through a medium with a velocity greater than the velocity of light, it radiates photons. They are emitted at an angle θ_C relative to the direction of motion of the particle given by.

$$\cos\theta_C = \frac{1}{n\beta} = \frac{1}{n}\sqrt{1 + \frac{m^2c^2}{p^2}}. \tag{3.2}$$

Here n is the refractive of the medium crossed by the particle, $\beta = v/c$ is the speed of light *invacuo*. So if the momentum of that particular particle is known, its mass can be deduced by measuring θ_C. Form Eq. (3.2), the threshold condition for the Cerenkov effect can be calculated as,

$$\beta \geq \frac{1}{n}. \tag{3.3}$$

A Ring Imaging Cerenkov detector (RICH) takes advantage of the Cerenkov effect to identify charged particles. The COMPASS RICH detector [67] is capable of separating kaons, pions and protons in an energy domain between 5 GeV/c and 43 GeV/c
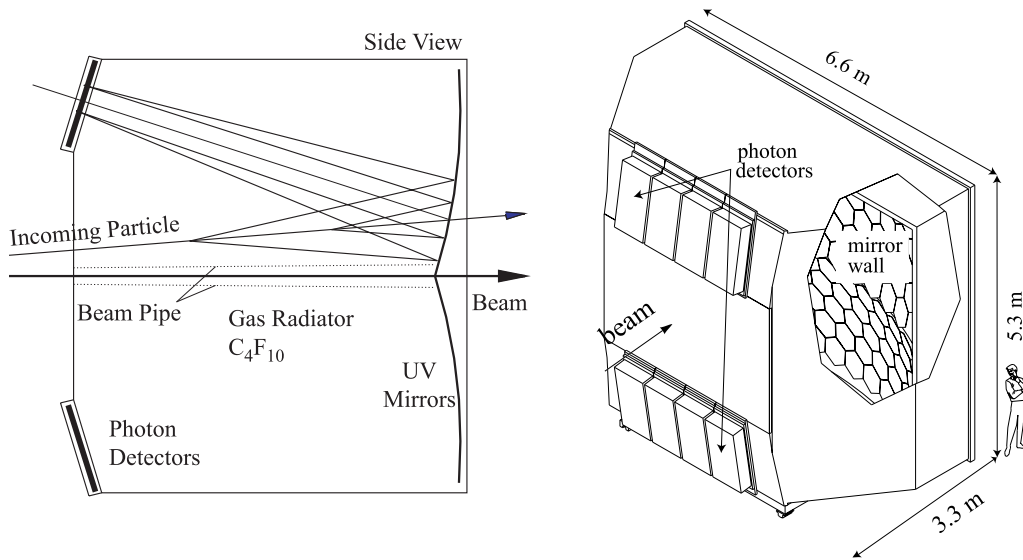
Figure 3.8: COMPASS RICH-1: principle and artistic view.

Fig. 3.8 shows, the RICH large volume vessel is approximately 3.3 m long in the beam direction, with a width of 6.6 m and a height of 5.3 m filled with C_4F_{10} radiator gas, with a refractive index of 1.00153 at 1 bar and 20°C. Under these conditions the threshold energy for the emission of Cerenkov light is 2.5 GeV/c for pions, 8.9 GeV/c for kaons and 17 GeV/c for protons [68, 69].
The intensity of Cerenkov photons radiated by a traveling particle increases with decreasing photon wavelength, thus it is useful to build a system which works in the very ultra-violet (VUV) range. The Cerenkov photons will have to travel several meters though the radiator gas, so the gas has to be transparent as possible. The produced photons in the radiator gas are reflected by two spherical mirror systems (with radius $R_m = 6.6$ m) and focussed onto photon detectors, giving a ring in the plane of the photon detectors. The radius of this ring (r) is related to the focal length of the mirror system and the Cerenkov angle

$$r = \theta_C \frac{R_m}{2}. \tag{3.4}$$

Thus the measurement of ring radius provides an access to calculate the Cerenkov angle. The photon emitted are reflected from the mirror system and focussed onto the front wall which is coated with phot-sensitive CsI divided into pixels. Thus the Cerenkov photons are converted to electrons in CsI layer, where the layer is situated on the cathode plane of a MWPC to detect the resulting electrons. The readout cathode of 8×8 mm^2 provide the sufficient resolution with a total active area of 5.3 m^2. The CsI photon converters have good quantum efficiency for wavelengths below 200 nm, which provides compatibility in the VUV domain of both the mirror system and the gas radiator. Quartz windows separate the radiator gas from the photon detector and provide a lower limit of the sensitive region of the RICH detector of 165 nm. The radiator gas system establishes continuous gas circulation in a closed loop, ensuring a optimum VUV transparency and maintaining a constant relative pressure in the vessel.

3.6.2 Calorimetry

The COMPASS spectrometer is equipped with two hadronic calorimeters and an electromagnetic calorimeter. The two hadronic calorimeters HCAL1 and HCAL2 are used to measure the energy of hadrons produced in the target and participate in triggering on inelastic muon scattering events. Both hadron calorimeters consists of several layers of iron and of scintillator plates. They are located before the muon filters (see Fig. 3.7).

The hadron calorimeter1 (HCAL1): The HCAL1 is situated before MW1 upstream of SM2. It consists of modular structure with each module consisting of 40 layers of iron (20 mm thick) and scintillator plates (5 mm thick). 480 such modules are used in HCAL1 which are assembled in a matrix of 28×20 (horizontal×vertical) with a rectangular window of 8×4 modules removed in the

centre of the matrix, to make a passage for the beam. The light from the scintil-
lator is collected by a flat light guide. The amount of light collected by a single
scintillator traversed by a minimum ionizing particle is good enough to produce 4 to
6 photoelectrons at the Photo Multiplier Tube (PMT) photocathode. The signals
from PMTs are sent via cables of about 140 m length to a fast analog to digital
converter. Small fractions of signals are fed into the fast summation system for
trigger purposes [70].

The HCAL1 has a spatial resolution of $\sigma_{x,y} = 14 \pm 2$ mm, with an active area of
4.2×3 m^2. The energy resolution of HCAL1 as a function of the energy for pions
can be parameterized by $\sigma(E)/E = (59.4 \pm 2.9)$ %$/\sqrt{E} \bigoplus (7.6 \pm 0.4)$ %, with the
energy E in units of GeV.

The hadron calorimeter2 (HCAL2): The HCAL2 is the second
calorimeter used in COMPASS spectrometer. It is placed downstream of SM2 and
in front of the second muon filter (see section 3.6.3). The HCAL2 takes the form of
a matrix of 22×10 modules, arranged on a mobile platform. Most of the modules
consists of 36 steel plates (25 mm thick) interleaved with scintillator sheets (5 mm
thick), which were used previously by NA12 experiment [71], however the method
of light collection from scintillator and high voltage bases for photomultipliers were
modified to meet the requirements for COMPASS experiment. The calorimeter has
a hole with the dimensions of 2×2 modules to pass the high intensity beam.

The readout of the scintillation light is done by wavelength shifting fibres of 1 mm
diameter placed in a circular groove in each scintillator sheet, the light collected
from those bundle of fibres from all the sheets are transferred to the photocath-
ode of a Photo Multiplier Tubes (PMTs). The energy resolution for HCAL2 is
$\sigma(E)/E = (66/\sqrt{E} \bigoplus 5)$ %, with the energy E in units of GeV.

The electromagnetic calorimeter2 (ECAL2): The ECAL2 is made
from 2972 modules of lead glass assembled in a matrix of 64×48. The ECAL2 used in
the COMPASS spectrometer was previously used in the GAMS-4000 spectrometer
[72]. When an gamma ray or an electron is incident on ECAL2, it develops an
electromagnetic shower inside the lead glass which eventually emits Cerenkov light
on its way through the glass. A PMT connected to each lead glass block measures the
intensity of the light emitted from that particular block, as the energy deposited on
each counter is proportional to the amount of Cerenkov light emitted. With one such
counter, about 1000 photoelectrons per GeV energy deposit can be obtained. All
the modules are installed inside a frame which can be moved both ways, horizontally
and vertically. ECAL2 has a hole of 10×10 modules in the centre to make a passage
for the beam. The energy resolution for ECAL2 is $\sigma(E)/E = 5.5\%/\sqrt{E} \bigoplus 1.5\%$ and
has a space resolution of $\sigma(x) = 6$ mm$/\sqrt{E} \bigoplus 0.5$ mm, with the energy E in units
of GeV.

3.6.3   Muon identification

The muon identification is accomplished by two detector systems. In the LAS region, the muon filtering system consists of two stations of Muon Wall 1 (MW1) separated by a 60 cm thick iron absorber (Muon Filter 1), whereas in the SAS region, the system consists of a 2.4 m thick concrete absorber (Muon Filter 2) followed up by two stations of Muon Wall 2 (MW2) and three stations of MWPC stations.

Muon Wall 1 (MW1) : The basic element used in building the MW1 is a gaseous wire detector called Mini Drift Tube (MDT). A particle detected in both detector layers is regarded as a scattered muon.
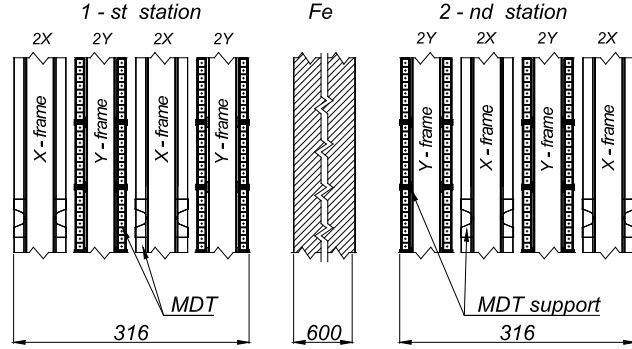
Figure 3.9: Schematic cross–sectional side view of MW1 all dimensions are given in millimeters. Vertically only part(255 mm) of the stations are shown.

Fig. 3.9 shows the schematic view of the MW1 system, consisting of two stations separated by the iron absorber. Each station consists of four detectors with two planes of MDTs on both sides. Vertical and horizontal tubes provide the X and Y coordinates respectively. Both planes X and Y have a hole in their center to match the acceptance of SM2. The active area covered by the X plane is of 4845×4050 mm^2 and 4730×4165 mm^2 by the Y plane respectively.

Muon Wall 2 (MW2) : The MW2, at the back of the SAS uses the same principle as in MW1. The MW2 consists of two identical stations with each station composed of 6 layers of drift tubes which are grouped into double layers. There are three double layers assembled in vertical, horizontal and inclined positions. The inclined tubes are at $-15°$ with respect to the vertical tubes. There are 1689 tubes used in building the two stations.

Minimally deflected muons which already flew through the beam hole in the first Muon Wall (MW1) can be detected here.

3.7 The trigger system

An complete physics event has to be formed with the tiny pieces of information provided by the individual detectors described above. For that a signal must be activated during the process and must be distributed to the read-out of all the detectors. A signal from the trigger system provides the command to process all data collected within a specified time window and also to suppress the recording of events which are not interesting. This trigger signal must be available as quickly as possible, since the buffering of data in the detector is limited (< 600 ns) especially in the case of the HCALs. To ensure the availability of the signal within the required time scale, the trigger system is based on fast hodoscopes and read out by photomultipliers. Based on their construction, position with respect to the beam and the kinematic regions covered, the trigger hodoscopes are categorized in different classes: Outer Trigger (OT), Inner Trigger (IT), Middle Trigger (MT) and Ladder Trigger (LT) [73]. As the scattered muon looses up to 20% of its original energy, the particle must be detected in two such detectors at different positions in z along the beam. Therefore each trigger system is divided into two hodoscope stations, the inner (H4I, H5I), the ladder (H4L, H5L), the middle (H4M, H5M) and the outer system (H3O, H4O), as shown in Fig. 3.10. The events selected by this trigger can be classified in two groups: Photon-gluon fusion events and inclusive deep inelastic scattering events.
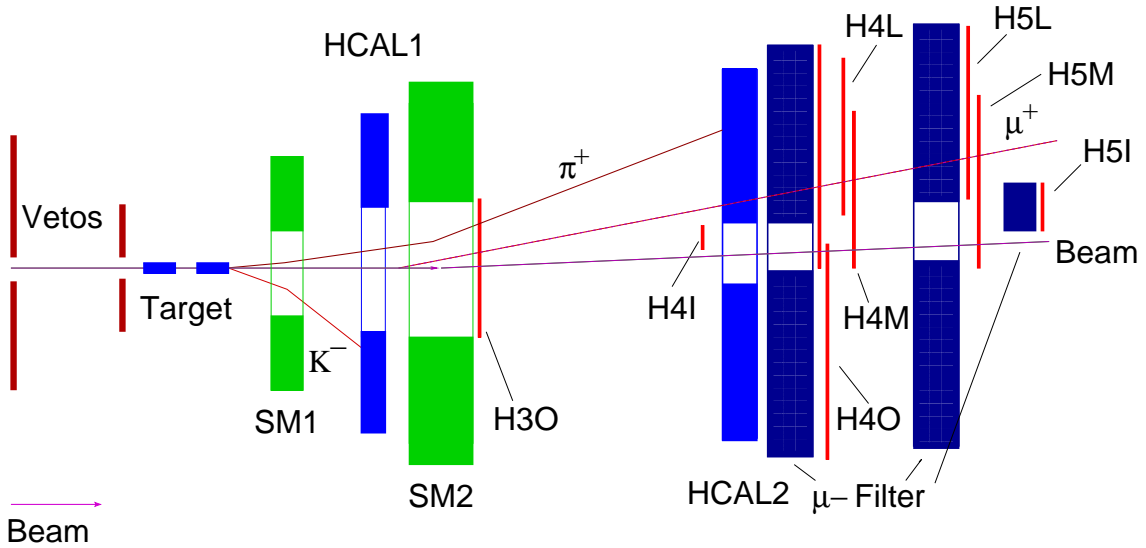
Figure 3.10: Location of the components relevant for the trigger.

3.7.1 Trigger on photon-gluon fusion events

Photon-Gluon Fusion (PGF) events are of great importance to the open charm measurement for the measurement of ΔG at COMPASS. Therefore it is important to make use of the entire photon spectrum, even down to quasi-real photons due to the flux increase at small Q^2. At low Q^2, the muon scattering angles are close to zero providing a first requirement for the trigger. A sufficient degree of polarization of the exchanged photon is required as it enters the data analysis in form of the depolarization factor D, which is approximately proportional to the relative energy of the photon, y. Therefore, the minimum requirement for the trigger was chosen to be $y > 0.2$. The scattered muons of differing energy are deflected in the
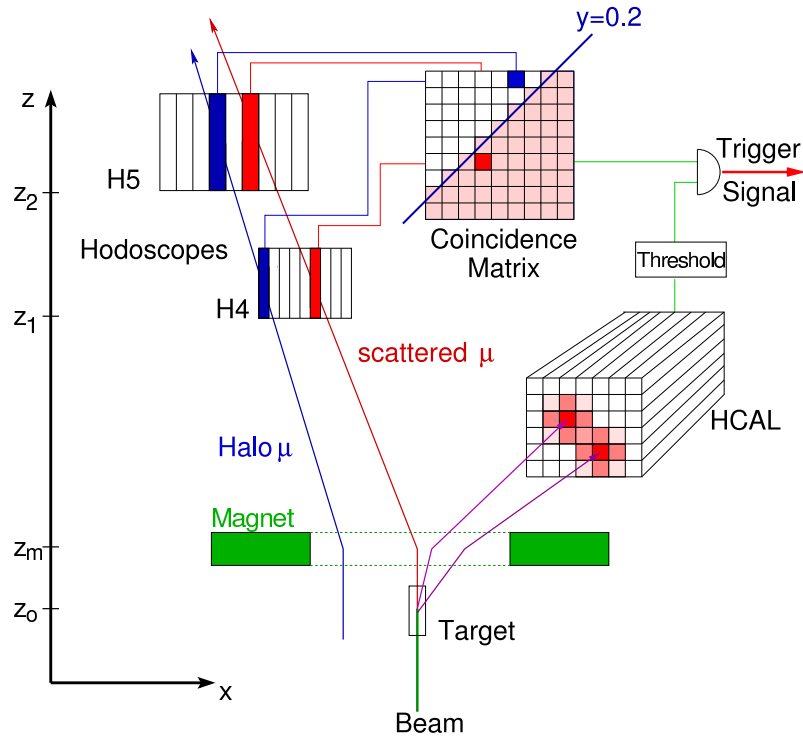
Figure 3.11: Concept of the trigger for quasi-real photoproduction with high energy loss. The scattered muon leads to a coincidence in the activated area of the coincidence matrix while the halo muon fails to do so. In addition, a minimum hadron energy can be required in the calorimeter.

field of the spectrometer magnets causing signals in different channels of the trigger hodoscopes. The signals are fed into a coincidence matrix which selects only those hit combinations which correspond to an energy loss of more than 20% (see Fig. 3.11). As there are a number of background processes, such as elastic scattering off target electrons and elastic and quasi-elastic radiative scattering off target nuclei present in the kinematical region of quasi-real photo production, the information from the hadronic calorimeter can be used to reject most of the background events and those triggered by beam halo. This way, the background events caused by halo

or beam muons that pass through the spectrometer with little energy loss can be suppressed.

3.7.2 Trigger on deep-inelastic scattering events

In contrast to the trigger on PGF events, a large momentum transfer, $Q^2 > 0.5 \text{ Gev/c}^2$ is required for deep-inelastic scattering events. The trigger classes selecting these events are Middle Trigger (MT) and Outer Trigger (OT). They consist of two hodoscope setups for each of the triggers (see Fig. 3.12). The hodoscopes used here
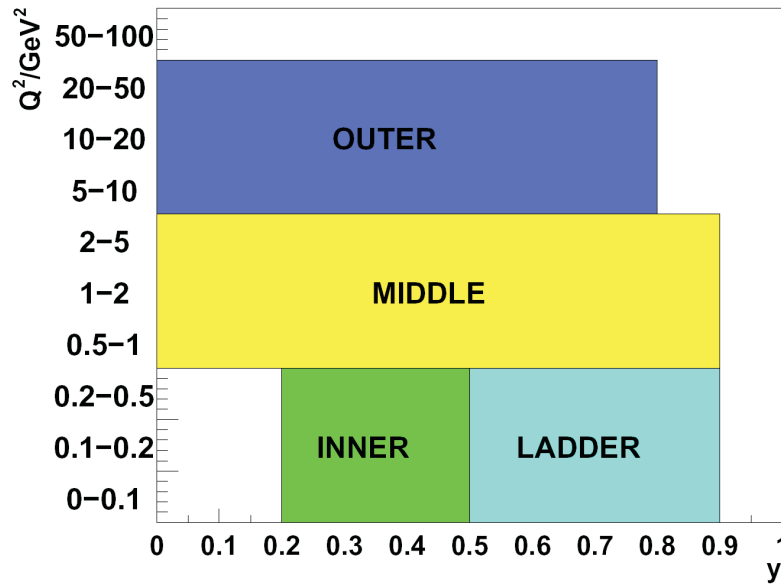
Figure 3.12: The kinematic regions in the $Q^2 - y$ plane covered by the different triggers.

consist of horizontally mounted plastic scintillator covering a wide range to each side of the beam. Information from the hadron calorimeter may not be demanded since this trigger setup is also used to detect the inclusive scattering reactions, in which no hadron is detected. Several veto counters are installed in the pre-target region to suppress signals from halo muons. The active area of these veto counters cover only the area outside the beam. If there is a signal registered in one of these counters, a halo muon is presumed and the event is discarded.

3.8 The read-out concept

With over 250 000 detector channels to be read out and to record a total amount of data up to 350 TByte per year demanded a special design of the Data Acquisition

system (DAQ). In the COMPASS experiment, the DAQ has to cope with the high particle fluxes of $2 \cdot 10^8$ μ per spill of 4.8 s with trigger rates of about 10 kHz for the muon beam. To meet those demanding tasks, an entirely new read-out concept was designed [74].
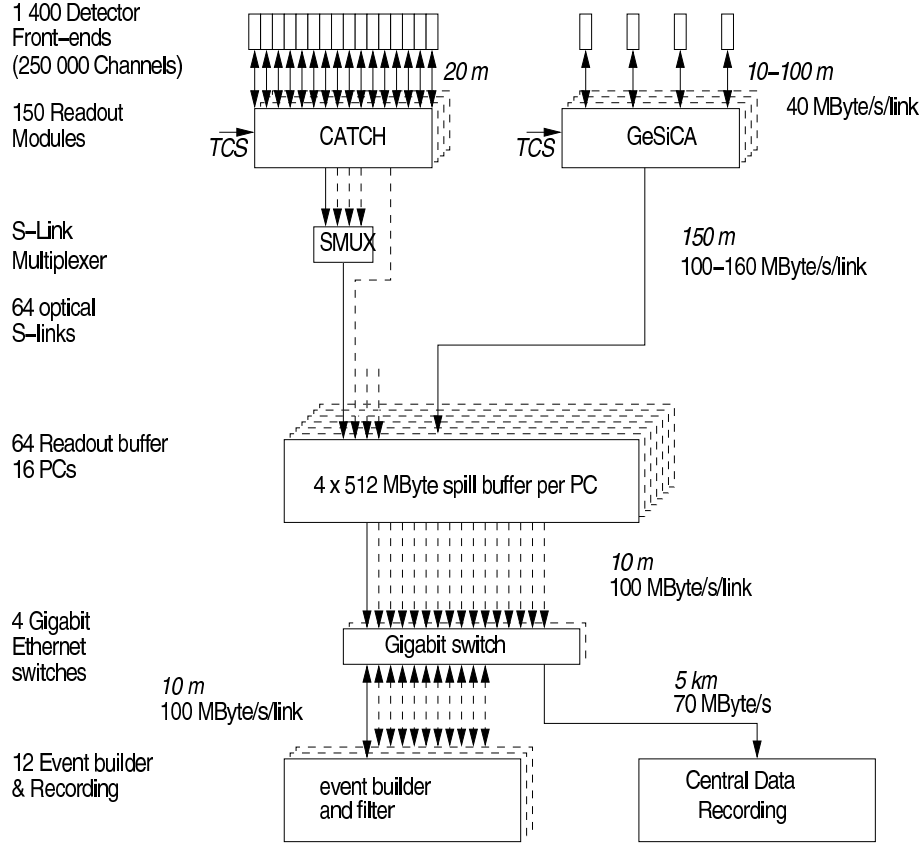
Figure 3.13: General architecture of the DAQ system. Digitised data from the detector front-ends are combined on the readout modules named CATCH and GeSiCA close to the detectors. The storage of the data during the spill and the event building is performed locally. The data are recorded at the CERN computer centre.

An overview of the data flow is shown in Fig. 3.13. As the preamplifiers and discriminators are located near to every detector, the data is constantly digitized and buffered with the help of custom designed TDC[5] and ADC[6] modules. The synchronization of the various digitized readout units is performed by the Trigger Control System (TCS). As soon as the trigger signal is activated the data are transferred via fast links to readout-driver modules named CATCH[7] and GeSiCA[8]. These modules are also responsible to distribute the trigger signals to the front-ends and initialize them during the system startup. The readout-driver modules combine

---

[5]**T**ime-to-**D**igital **C**onverter
[6]**A**nalog-to-**D**igital **C**onverter
[7]**COMPASS** **A**ccumulate **T**ransfer and **C**ontrol **H**ardware
[8]**GE**m and **SI**licon **C**ontrol and **A**cquisation

the data from the front-end cards and transmit the sub event to readout buffer via optical S-Link at a speed of 160 MByte/s. The data coming from each link are stored in 512 MByte spill buffer cards in the central Read-Out Buffers (ROBs).

The data are distributed from the ROBs to twelve *event − builders* working in parallel, where they are combined to global events. In 2004 the total data transmitted during the spill to the readout buffers correspond to 230 MByte/s. Finally these data are recorded on tape remotely at the CERN central data recording facility located in the CERN computer center.

3.9 Data-analysis at COMPASS

A huge amount of data (nearly about 350 TB per year) is collected by the experiment. This requires the availability of sufficient computing power to reconstruct the events at a rate comparable to the data acquisition rate. The demanded CPU power is provided by 200 Linux Dual-CPU PCs at CERN. First step in handling of the data is called the *Production* process, where the raw data are used to reproduce particles and their tracks. After this process is completed, the data is ready to use for different physics analyses.
Raw data from COMPASS experiment are stored in the Central Data Recording (CDR) system at the end of every run and transferred to the COMPASS Computing Farm (CCF) where the data are stored for a certain period of time before being written to tape. Data access from tape is established through the CASTOR[9] system where the user is provided with a directory structure and commands for writing, reading, opening and closing of the files. When a file is being requested by an user, CASTOR downloads a copy from the tape onto a local disc for access.

3.9.1 Event reconstruction

The Event reconstruction is performed by a fully object oriented program called CORAL[10]. This is designed with a modular architecture with collection of class libraries written in C++ programming language. A schematic representation of the reconstruction program is shown in Fig. 3.14.

The input given to the reconstruction procedure is either the raw data collected by the experiment or the output from Monte Carlo simulation software. Only the reconstruction of real data is explained here. Before the raw information from the detectors is sent to the track finding algorithm, two initial processing phases

---

[9]**CERN A**dvanced **STOR**age
[10]**CO**MPASS **R**econstruction and **A**na**L**ysis
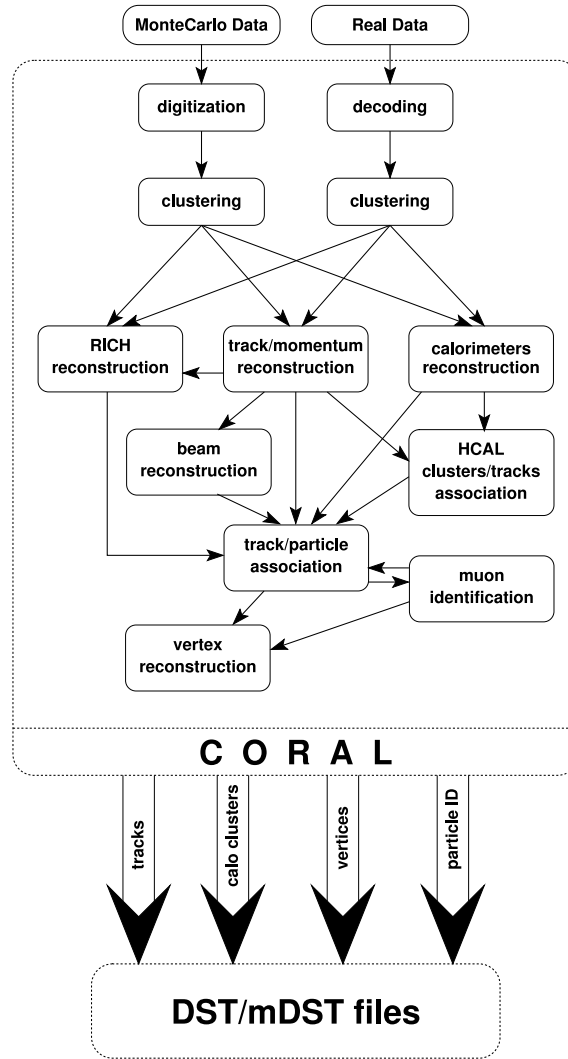
Figure 3.14: Schematic representation of the COMPASS reconstruction software.

are required. **Decoding :** In this first phase, the information from the fired detector is extracted from the raw data. **Clustering :** In the second phase, the information from the detector channels that have fired by the same particle are grouped together. Finally the different steps of the data reconstruction are performed, like track and vertex reconstruction and also the hadron identification by RICH reconstruction which are explained in the following part.

Track reconstruction: The spectrometer is divided into three regions by the two spectrometer magnets SM1 and SM2 respectively. This is done by the track reconstruction algorithm named TRAFFIC/TRAFFDIC. The three phases of reconstruction corresponds to: a) pattern recognition, where, the track segments are identified in the various zones of the spectrometer then, b) the track segments from several distant zones are connected to build full tracks (Bridging) and finally c) the best estimators for the parameters of the reconstructed tracks are computed (Fitting).

Vertex reconstruction: Various tracks that have a common point suggest the existence of an interaction point or a vertex. Here the aim is to get the best estimator of the three coordinates of the vertex position from each track that is assumed to originate from there. All tracks surviving the initial phase are used to estimate the parameters of the vertex and the relative χ^2 fit is performed, which acts as a measure of probability of a particular vertex. The approximation of the primary vertex is possible by computing the average Point Of Closest Approach (POCA) between one beam track and all possible outgoing tracks.

Particle identification: The particle identification is performed inside CORAL by a package named RICHONE. The raw information from the RICH detector provides the coordinates of the photon detector pads with a signal above threshold. This information combined with the particle trajectory from track reconstruction is used to calculate the probability that the particle is of a particular type.

After the reconstruction phase, the information such as track parameters, vertices, calorimeter clusters, PID probabilities, detector hit patterns, etc are stored into output ROOT trees called as mini Data Summary Tapes (mDST). The data reduction factor between the input raw data and the output mDST is about 100.

3.9.2   PHAST

PHAST[11] [75] is an internally developed program. It is the main tool for physics data analysis at COMPASS. This program reads in all objects from the mDSTs. It provides dedicated classes and functions based on the CERN ROOT packages [76]. Using these common routines, various physics analysis can be performed. The data analysis explained in Chapter 4 was performed with PHAST.

---

[11]**PH**ysics **A**nalysis **S**oftware and **T**ools

Chapter 4

Extraction of transverse spin asymmetries at COMPASS

> "What we observe is not nature itself, but nature exposed to our method of questioning."
>
> Werner Heisenberg

One of the main objectives of the COMPASS experiment is to gain more knowledge on target transverse spin dependent asymmetries especially the transverse quark distribution function $\Delta_T q$. About 20% of the total running time has been spent on target transverse spin measurements in the years 2002, 2003 and 2004, with 11 days of data acquisition in 2002, 9 days in 2003 and 14 days in 2004. The following sections are devoted to the extraction of target transverse spin dependent asymmetries from the data obtained from the the 2002, 2003 and 2004 beam-times at COMPASS. RICH detector information has been available only for the 2003 and 2004 beam-times. Therefore, the results of extracted transverse spin dependent asymmetries for identified pions and kaons for the years 2003 and 2004 are discussed first, followed by the results for the unidentified hadrons for the years 2002, 2003 and 2004.

4.1 Transverse data and their production

Measurements with transverse target polarization during each beam time were taken in a period with the target cells polarized oppositely. In principle, the asymmetry could be calculated from the difference in the counting-rates from the two target cells. This method is subject to systematic effects coming from the different acceptance

of the two cells. In order to avoid such effects as far as possible, the polarization of the cells is reversed between two periods. The counting rate asymmetry is then calculated for the two target cells separately in two periods (period 1 and period 2) with opposite spin configurations (see Fig. 4.1), these being described as either $down - up$ or $up - down$ periods according to the spin configuration of the target cells.
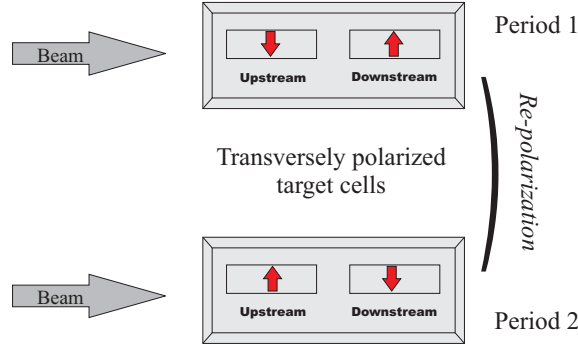
Figure 4.1: Schematic depiction of the target cells in transverse mode with longitudinally polarized muon beam. Measurements are always performed with opposite polarizations in the two target cells. The polarization is reversed in both cells between periods.

The spin orientation of the polarization of the COMPASS target cannot be flipped by inverting the magnetic field, because the acceptance would change. Therefore the polarization reversal is done by exchanging the microwave frequencies of upstream cell and downstream cell in the target. The duration of this process is typically two days in order to achieve $\sim 50\%$ polarization. Once the target is polarized the data is taken for several days (typically 5 days) before a polarization reversal is done. Data is taken again with the target polarized after a spin flip for 5 more days.

4.1.1 Data production

The data production process described in section 3.9 was performed for all the periods. During data acquisition, some changes in the spectrometer can occur. These changes influence data reconstruction accuracy. Therefore for each period special calibration and alignment runs are taken. Later each period is processed separately. Typically, one physics run occupies about 70 gigabytes of disk space. During storage, one physics run is divided into chunks. One chunk is usually of 1 Gbyte and contains about 25 000 events. Fig. 4.2 shows a schematic view of the reconstruction and analysis system to which the data flows after they are stored centrally.
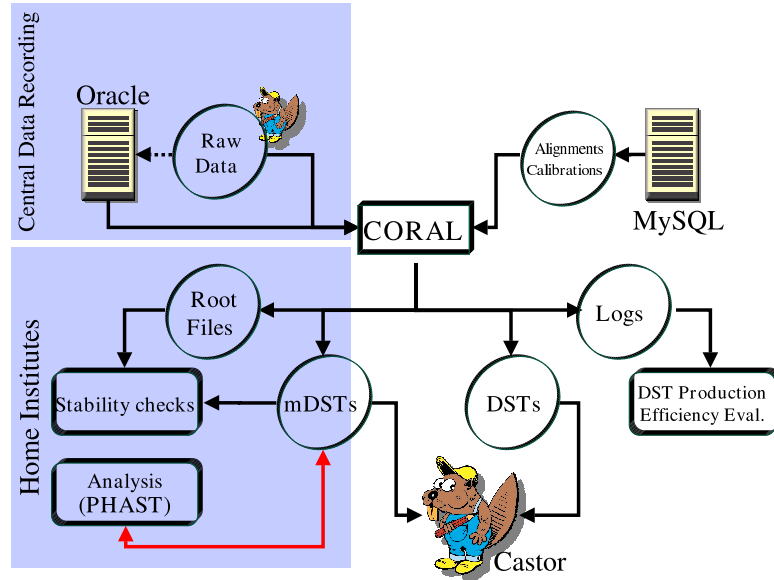
Figure 4.2: Schematic view of the off-line system and reconstruction and analysis flow

Once the production algorithms and the necessary files such as calibration and alignment files are finally settled, a pre-selection of the data suitable for production is made on the basis of criteria recorded in the online log-book such as beam stability, number of spills, target polarization and the magnetic fields of SM1 and SM2. Not all runs of the given period are processed, the number of "good runs" was taken by excluding the runs in which for whatever reason several detectors had malfunctioned. The production is performed on a run-by-run basis. One production script starts about 70 (parallel) jobs, each one is to process one chunk of the data. The typical processing time for one event is about 0.5-1.0 sec, so processing of a run may takes 3-6 hours. After the production, the size of the mDST is about 1% of the original raw data, later this mDST's are used to perform physics analysis by means of another program called PHAST (see section 3.9.2). In the 2002 to 2004 data acquisition periods, the experiment benefited of about $12 \cdot 10^5$ spills in which COMPASS collected about 30 billion events, corresponding to a total sample of more than 1PByte $(1 \cdot 10^{12})$.

The COMPASS beam-time in 2002 had three periods in which the measurements were taken with transverse target polarizations - P2B, P2C and P2H, one polarization reversal took place between the periods P2B and P2C, and second in the middle of P2H, breaking the period further down into P2H1 and P2H2. In the beam-time in 2003, there were two periods - P1G and P1H, whereas in 2004 there were four periods - W33, W34, W35, W36. Two polarization reversal took place, first between W33 and W34 and second between W35 and W36. Table. 4.1 gives

an overview of the periods with transverse target polarization

Year	Period	Target polarization
2002	P2B	⇓⇑
2002	P2C	⇑⇓
2002	P2H.1	⇓⇑
2002	P2H.2	⇑⇓
2003	P1G	⇓⇑
2003	P2H	⇑⇓
2004	W33	⇑⇓
2004	W34	⇓⇑
2004	W35	⇓⇑
2004	W36	⇑⇓

Table 4.1: The transversity data acquisition periods the 2002, 2003 and 2004 beam-time at COMPASS. The target polarization of the two cells, upstream and down-stream are shown.

4.1.2   Data quality checks

To make sure that the data produced is in fact ready for the physics analysis, some production efficiency checks are performed. During the processing of each run, log files are produced and are used to check how many chunks have been successfully completed. In some cases it may occur that some data contained in a chunk were corrupt, these corrupted chunks are skipped while processing and this will not affect the production of the runs further.

The performance of the apparatus before and after the target spin reversal between the sub periods is monitored. The reliability of the data taken over an entire period is tested with various parameters by using the histogram files produced during the production. Using the histograms produced during the event reconstruction, the detector performance stabilities were checked by looking at the shape of the hit distribution in about 360 detector planes. The time stability of the detector and reconstruction efficiencies were also checked. Further details about various data quality checks can be found in [77].

Runs showing some instability were not used for the physics analysis. The runs rejected by this criterion are 9 for the 2002 data, 28 (out of a total of 458) for the 2003 data and 44 (of 462) for the 2004 data, corresponding to about 5% and 4% of the initial raw event sample.

4.2 Event selection

For the calculation of the target transverse spin dependent asymmetries, deep-inelastic scattering events in which at least one hadron is produced are required. In the following sections, the applied kinematic and other cuts used in the data analysis are discussed.

4.2.1 Q^2 reduction

Several physics analyses performed at COMPASS, such as that to determine the gluon polarization ΔG, deal with events in the whole kinematic range of Q^2. For transversity analysis, only events in deep-inelastic regime are of interest. The condition $Q^2 > 1$ Gev/c is defined to select events in this regime. This cut is responsible for a considerable reduction of data. The Q^2 reduction is performed separately on a run-by-run basis and the reduced data files are saved to tape. Due to the reduction of data size after Q^2 cut, computing power required for the further steps of the analysis is considerably reduced.

4.2.2 Cuts on the primary vertex and muons

Primary Vertex : The muon interaction point called as "primary vertex" is defined by one beam particle and one scattered muon. The primary vertex is reconstructed by CORAL (explained in section 3.9.1). If more than one primary vertex is reconstructed in one event, then the PHAST defined "best primary vertex" is taken to select a primary vertex. The PHAST defines the best primary vertex on the basis of their reduced χ^2 and the number of outgoing particles used in the reconstruction. These reconstructed primary vertices lie in the COMPASS coordinate system in z either in the upstream cell (-100 cm and -40 cm) or in the downstream cell (-30 cm and $+30$ cm). All vertices outside these regions are discarded. Fig. 4.3 shows the distribution of the primary vertex z-coordinate before any cut has been applied.

Due to the additional dipole field the target cells are displaced in transverse running mode with respect to the longitudinal case. Therefore the target position was independently deduced for the transverse running. Fig. 4.4 shows how the target position was deduced. A distribution of the primary vertices is plotted for various positions along the beam axis. In these plots, the position of the target cylinder with the radius of 1.5 cm can be located, so the displacement in x and y can be extracted. As the magnetic field orientations do not change during the transverse running mode, all these measurements can be combined. For each year, the displacement in x and y is plotted against the position along the beam axis. No displacement along z was observed, therefore the standard positions (-100 cm $z_{\text{up}} - 40$ cm ; -30 cm $z_{\text{down}} + 30$ cm) were used.
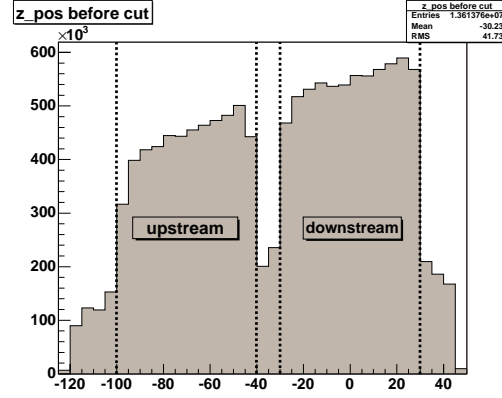
Figure 4.3: Distribution of the primary vertex z-coordinate
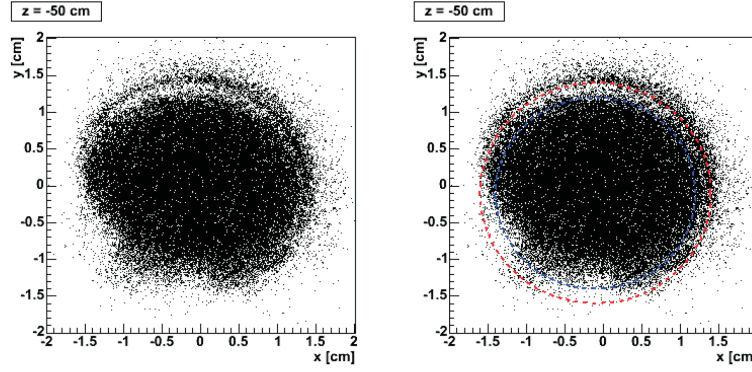
Figure 4.4: Left: Distribution of the primary vertices at the most upstream part of the target. The target cylinder can be easily identified. Right: Same distribution with red circle refers to the shape of the cylinder, whereas the blue circle indicates the region accepted by the radial cut of r = 1.3 cm.

To make sure the primary vertex is well inside of the target material, the PHAST routine **PaAlgo::InTarget** is used. The applied cuts using **PaAlgo::InTarget** routine were the radial cut of $r_t < 1.3$ cm. A further cut was applied to ensure an identical beam intensity in both target cells, ensuring a nearly identical luminosity. Only those events were accepted, where the projection of the incoming muon beam lies within the same cuts at the most upstream end of the target cell at ($z = -100$ cm) and the most downstream end of the target cell at ($z = 30$ cm). This cut was achieved by another PHAST routine **PaAlgo::CrossCells**.

Beam Muons : The beam muon associated in the mDST with the best primary vertex is taken as the beam particle. A cut on a maximum momentum of $p_{beam} < 200$ GeV is applied. A total χ^2 is calculated for each track when the mDST data are produced. The calculated χ^2 fit expresses the summed probability that each hit assigned to the track does belong to it. Now the reduced χ^2 can be

constructed be the relation,

$$\chi^2_{red} = \frac{\chi^2_{tot}}{N_{hits} - 5}. \tag{4.1}$$

Here N_{hits} is the number of hits along the track and the reduction by five appears due to the number of degrees of freedom emerging from the five parameters which are extracted from the track. For incoming muons, the reduced χ^2 greater than 10 leads to the event being discarded. The beam momentum distribution for W35/W36 data sample is shown in Fig. 4.5.
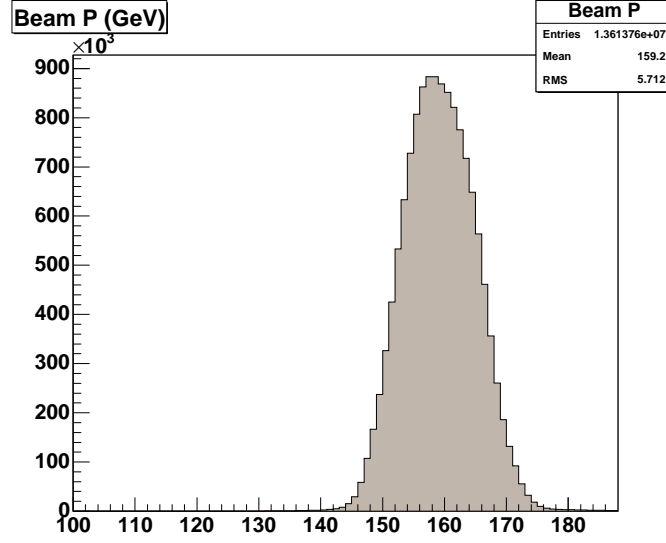
Figure 4.5: Momentum distribution of the reconstructed incoming muons for W35/W36 data sample.

Scattered Muon : The scattered muon μ' of the best primary vertex flagged by PHAST is taken if it fulfills the same criterion regarding χ^2_{red} as the beam muon. To achieve a clean muon identification, the amount of material traversed in the spectrometer had to be larger than 30 radiation lengths. Due to the fact that COMPASS trigger hodoscopes do not cover the full kinematics range in large-angle spectrometer, the muons scattered at large-angle are not taken into account as such. To overcome this problem, additional muons are recovered by the assumption that any outgoing particle from the best primary vertex which causes more than four hits in plane 1 and more than six in plane 2 of Muon Wall1 (MW1) is considered, provided they also satisfy the conditions $\chi^2_{red} < 10$ and $nX/X_0 > 30$ as applied to the flagged scattered muons. To be noted that the two planes in the muon wall 1 are separated by a thick iron absorber. Applying the following criteria an event is discarded:

- If more than one "recovered" muon is found in an event,

- If a flagged μ' and a "recovered" μ' are found in the same event,

- If more than one flagged μ' is found in an event.

4.2.3 Cuts on the variables y and W

A further cut is applied on events with very large and very small values of the kinematic variable y. By applying the cut $y > 0.9$, the events with low μ' momentum are discarded. This cut is used to discard the events for which large radiative corrections are expected. An additional cut with $y < 0.1$ is applied to discard the events belonging to the elastic region. It also removes events with poorly reconstructed scattered muons or beam halo muons misidentified as scattered muons. Cuts on y leads to a further reduction of the sample size. A cut on the center of mass energy W is applied. $W > 5$ GeV cut removes the sample events in the region of the nucleon resonances. The y and W distributions before the cuts were applied is shown in Fig. 4.6. It should be noted that there is a large overlap of events being discarded with these two cuts.
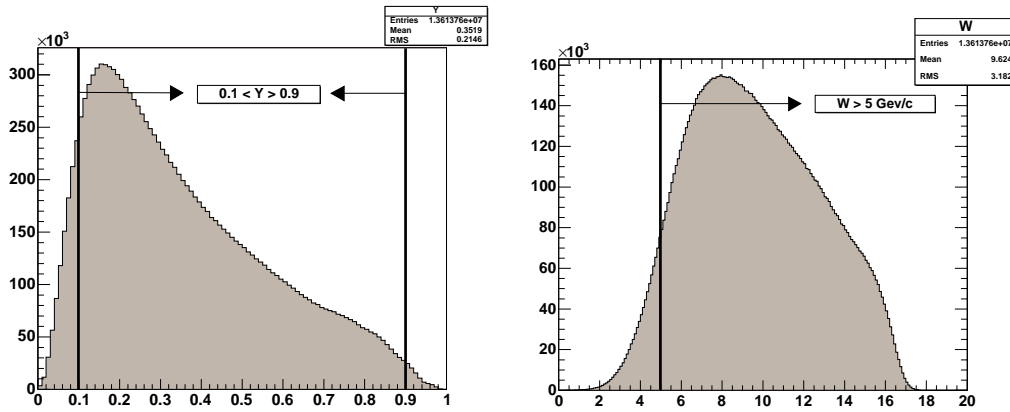
Figure 4.6: The y distribution (left) and the W distribution (right) before the applied cuts

4.2.4 Hadron identification

The flavor of the outgoing quark in the fragmentation process largely determines what type of hadron is produced with the largest momentum or energy. The production of a π^+ or a π^- contains a differing contribution from the transverse u and d quark distributions. In order to get information on both charges, from this point the analysis is performed for positive and negative hadrons i.e. events containing a positively-charged hadron and those in which the hadron has negative charge.
All outgoing particles from the best primary vertex which are neither flagged nor recovered muons are considered to be hadrons. As general condition applies, every

track must have at least one hit after the magnet SM1. Hence all tracks reconstructed only in the fringe field are rejected. This condition is satisfied by a cut on the last measured coordinate ($z_{last} > 350$ cm), where z_{last} is the z position of the last measured hit associated with the track. A hadron must satisfy $\chi^2_{red} < 10$ and a maximum nuclear interaction length $nX/X_0 < 10$ is also required. In addition a minimum energy deposition in any cluster associated with the hadron in HCAL1 or HCAL2 is required, specifically $E^{HCAL1} > 5$ GeV for 2002,2003 data acquisition periods and $E^{HCAL1} > 4$ GeV for 2004, $E^{HCAL2} > 8$ GeV for 2002,2003 data acquisition periods and $E^{HCAL2} > 4$ GeV for 2004. The correlation between the energy measured in HCAL and that measured by the spectrometer is shown in Fig. 4.7. The hadron is accepted even when no calorimeter cluster is found and the event is not discarded whereas an event is discarded when clusters in both calorimeters are associated.
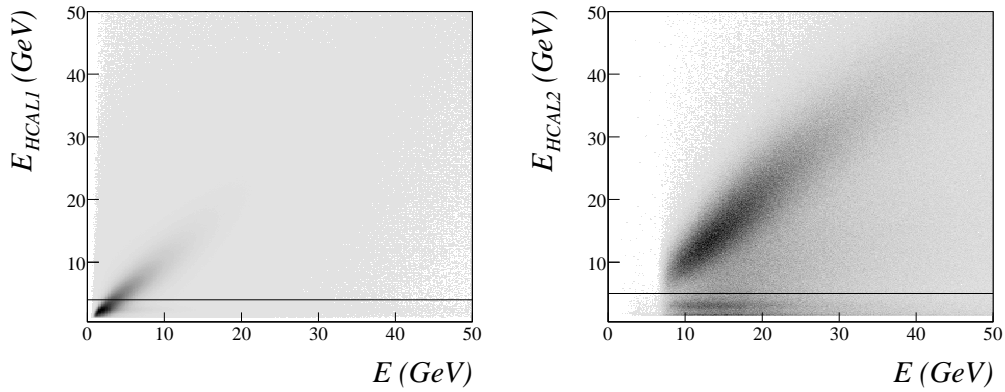
Figure 4.7: Correlation between the energy measured in HCAL1 (left) and HCAL2 (right) and the energy measured by the spectrometer for the 2004 data [77].

4.2.5   Kinematic cuts on all hadrons : z, p_t

The kinematic variable z gives the fraction of the photon energy transferred to the struck quark and consequently to the hadron produced in the fragmentation. At lower values of z, impurities occur through the secondary interactions of the original hadron with the target material, which can lead to the false identification of the hadron. A cut on z is applied to ensure that only the events with at least one hadron with $z > 0.2$ are used. The COMPASS kinematics are skewed down to lower values of z and a cut $z > 0.2$ ensures that the events are lost within an acceptable bound. The higher the energy of the identified hadron, the greater is the probability that it is the hadron initially produced at the start of the fragmentation process.
An additional cut on the transverse momentum (p_t) of the particle with respect to the virtual photon direction is applied, which has to be larger than 0.1 GeV/c.

This special cut is introduced to assure a good resolution in the measured azimuthal angle. The z and p_t distribution before the cuts were applied are shown in Fig. 4.8
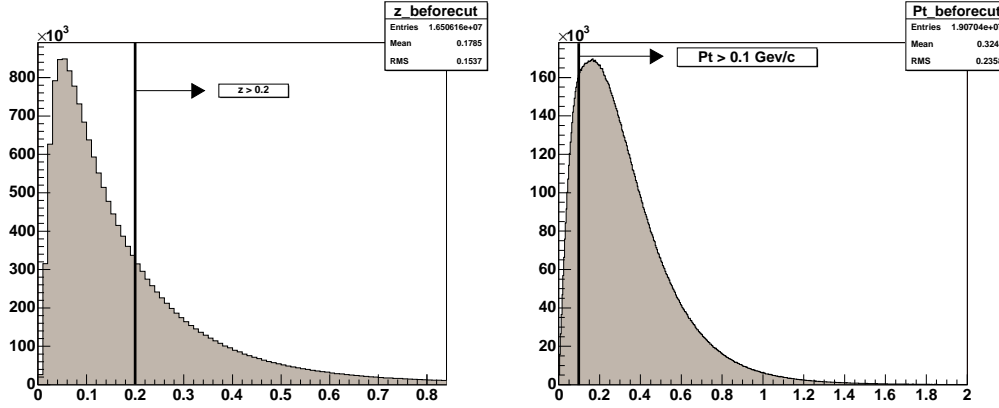
Figure 4.8: The z distribution (left) and the p_t distribution (right) before the applied cuts

4.2.6 Extra cut on y and z distribution

After applying all the cuts defined above, there is a peak present at high y in the y distribution of the positive hadrons appearing in the last z bin $(0.8 < z < 1)$ and an excess of events is also visible in the z distribution of the first x bin. The peak is also visible in the distribution of the energy of positive hadrons at high z and in the distribution of the momentum of the scattered muon.

One fact that is clearly visible is that none of these peak problems appeared for negative hadrons. This gave a lead to suspect a problem with hadron identification. The "scattered" muons giving origin to the peak in y distribution (identified by selecting events with $y > 0.8$ and $z > 0.8$) are particles which have passed through more than 100 X_0 and with a distribution of x and y coordinates that does not show evidence of holes in the muon wall (Fig. 4.9 (left)) and therefore are well identified positive muons even if they are not the true scattered muon. Moreover these tracks come from the primary vertex of the event. They should be muons coming from π or K decays, i.e. the decay product of a hadron coming from the vertex.

The positive hadrons with $z > 0.8$ belonging to events in the y-peak show one peculiarity, i.e. the distribution for the $x_l - y_l$ coordinates (last x and y coordinates of the reconstructed track) for these events is squeezed at very small values (a square of no more than 50 cm edge) even if the distribution of the last z_l coordinate is spread along the experiment. The $x_l - y_l$ distribution (Fig. 4.9 (right)) indicates the holes of the hadron absorber. By extrapolating "positive hadron" tracks till after the muon wall, we see, as expected, that for a large fraction of these events the number of X_0 passed is small, since they are passing through the hole
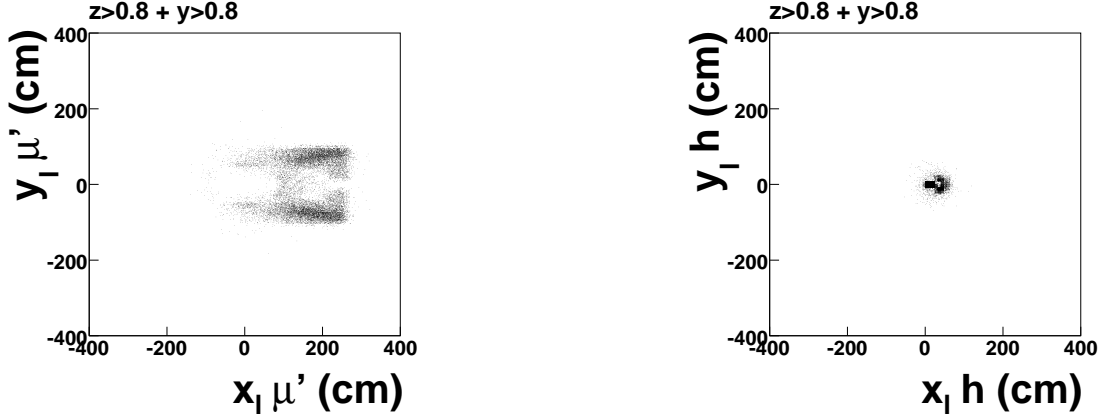
Figure 4.9: Left: $x_l - y_l$ distribution of scattered muons for positive hadrons with $z > 0.8$ and $y > 0.8$. Right: $x_l - y_l$ distribution for positive hadrons with $z > 0.8$ and $y > 0.8$.

in the iron absorber and do not trigger the event. The result is that the track of a muon falling in that region is associated with $nX_0 < 10$ and identified as a hadron by our selection rules.

- the scattered muon is identified as a positive hadron because it goes through the hole and does not cross large amount of the material,

- a positive muon from the primary vertex is reconstructed and wrongly considered as scattered muon.

The reconstruction of these events is wrong and they have to be rejected using the following cuts.
A cut in the x_l and y_l coordinates of the tracks or, even better, in the extrapolated x_e and y_e coordinates of the track after the iron absorber is used. By looking at the distribution of x_e and y_e for different intervals in z_l we see (Fig. 4.10) that the cut in these positions can be optimized. The adopted selection is:

1. $\sqrt{(x_e - 45 \text{ cm})^2 + y_e^2} < 10$ cm for $z_l < 2000$ cm;

2. $\sqrt{(x_e - 35 \text{ cm})^2 + y_e^2} < 15$ cm and ($|y_e| < 3$ cm and $|x_e - 55 \text{ cm}| < 13$ cm) for $2000 \text{ cm} < z_l < 4000$ cm;

3. $|y_e| < 25$ cm and $|x_e - 45 \text{ cm}| < 25$ cm for $4000 \text{ cm} < z_l < 5000$ cm

The loss of events due to this cut is negligible as it is less than 1% in the overall statistics.
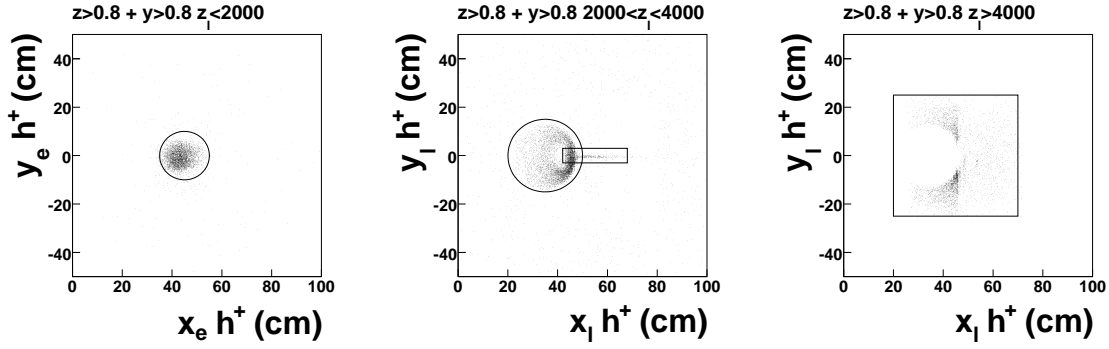
Figure 4.10: Distribution of positive hadrons versus $x_e - y_e$ extrapolated coordinates at 50 m for events with $y > 0, 8$ and $z > 0.8$, and tracks with $z_l < 20$ m $20 < z_l < 40$ m and $z_l > 40$ m. The applied cuts are also shown.

4.2.7 Final data-sample for unidentified hadrons

The final statistics entering the analysis after surviving all the cuts listed in the previous sections is shown in Table. 4.2. The table is consolidated to the 10 periods with transverse target spin in 2002, 2003 and 2004, for positively and negatively charged hadrons. The distribution of the important kinematic variables may be seen in Fig. 4.11 for W35/W36 period sample

Year	Period	Positive hadrons	Negative hadrons
2002	P2B/P2C	704840	594138
2002	P2H.1/P2H.2	472244	399692
2003	P1G/P1H	2429420	2029588
2004	W33/W34	2093759	1739317
2004	W35/W36	2716216	2258956
Sum		$8.4 \cdot 10^6$	$7.0 \cdot 10^6$

Table 4.2: Final Statistics for the years 2002,2003 and 2004 for hadrons with $z > 0.2$

4.3 RICH identified pions and kaons

The RICH information has been available only from the 2003 COMPASS beam-time and sustained for the 2004 beam-time. Asymmetries with identified pions and kaons are based on the P1G, P1H (2003) and W33, W34, W35, W36 (2004) data periods. The RICH detector is an important apparatus used within COMPASS detector setup. Since it is used for the hadron identification, some specific studies on the stability in time has to be done. RICH stability in time on a spill per spill basis has to be checked to avoid using data from bad spills in otherwise good runs. This analysis has been done after the rejection of the RICH bad runs. A detailed
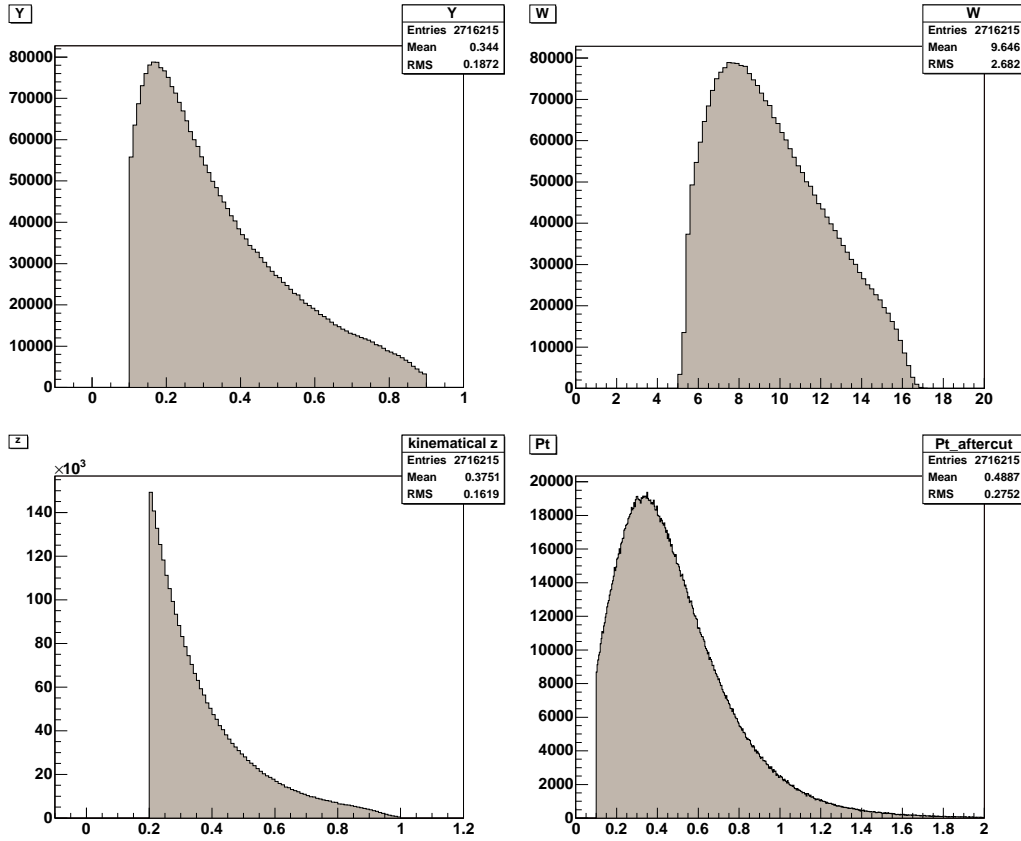
Figure 4.11: The distribution of the important kinematic variables in the final sample after applying appropriate cuts (top left: y distribution, top right: W distribution, bottom left: z distribution and bottom right: P_t distribution).

description on the RICH data quality checks such as monitoring bad runs and bad spills can be found in [78].

4.3.1 Likelihood analysis

Particle identification using the RICH detector is performed using a Likelihood method. Input to this analysis consists of the hits from the photon detectors of the RICH as well as the particle trajectories of the given events. In addition to this information the refractive index of the radiator gas is needed. The reconstruction of the RICH data starts with a clustering procedure. This procedure combines individual hits from the photon detectors to clusters, which are expected to correspond better to the real photon impact point. A transformation of the cluster coordinates to the $\theta - \phi$ plane is performed. Which is the plane of the polar and the azimuthal angles relative to the particle trajectory. In this plane the clusters from a given particle distribute along a fixed θ uniformly in ϕ, thus the ring search in the detector plane is equivalent to searching for a peak in the θ-projection.

Using the information, a likelihood is constructed for three mass hypotheses, namely pion, kaon and proton mass hypothesis, which is as follows:

$$L_N^i = \prod_{k=1}^{N_\gamma} \left[(1 - \epsilon)G(\theta_k^\gamma, \phi_k^\gamma, \theta_i^{ring}) + \epsilon B(\theta_k^\gamma, \phi_k^\gamma) \right] \qquad i \in \pi, K, p, \qquad (4.2)$$

where the product runs over all N^γ photons in the signal, θ_k^γ is the angle of the k-th photon in the ring, θ_i^{ring} is the expected Cerenkov angle for a given mass hypothesis i. ϵ is the background taken from the θ^γ distribution and $G(\theta_k^\gamma, \phi_k^\gamma, \theta_i^{ring})$ and $B(\theta_k^\gamma, \phi_k^\gamma)$ parameterize the signal and background contributions respectively.

The mass assignments are then done on the basis of the largest likelihood probability among the different mass hypothesis. A normalized version of the likelihood $L = \sqrt[N]{L_N}$ is then available for the analysis, in order to allow the comparison of different particles.

The signal contribution $G(\theta_k^\gamma, \phi_k^\gamma, \theta_i^{ring})$ to the likelihood can be conveniently described as a Gaussian centered at the expected angle θ_i^{ring} with a spread $\sigma_\theta^\gamma(\phi_k^\gamma)$. The advantage of using a likelihood method is that it takes into account the background contribution explicitly. Possible contributions to the background are electronic noise, photons from other particles belonging to the same event, but also photons from particles belonging to different events resulting from the memory of the photon chambers.

4.3.2 Cut for hadron identification

As it was explained before, the hadron identification using the RICH detector is based on a likelihood method [79, 80]. The hadrons are identified with a particular mass hypothesis if the likelihood corresponding to this mass hypothesis is the maximum one. To have a clear picture on the identification, some cuts on the hadron momentum and on two separate distributions $\frac{LH_{max}}{LH_{back}}$ and $\frac{LH_{max}}{LH_{2^{nd}max}}$ has been performed.

Cut on momentum : Corresponding to the 1.5σ separation between K and π, an upper limit for accepted momenta of 50 Gev/c has been chosen. A cut is applied little above the Cerenkov threshold (p_{th}) to avoid particles with no Cerenkov photons are emitted. The Cerenkov threshold p_{th} is calculated for a particular particle mass with the corresponding refractive index with the formula:

$$p_{th} = \frac{m}{\sqrt{n^2 - 1}}. \qquad (4.3)$$

The threshold is computed on a run-by-run basis. This cut is applied separately for pions and kaons.

Cut on Likelihood variables : Two variables, $\frac{LH_{max}}{LH_{back}}$ and $\frac{LH_{max}}{LH_{2^{nd}max}}$ are used. The first variable gives the separation to the background hypothesis: if the variable is near 1 then it means that the LH of the identified particle and that of the background have the same value. Therefore the distinction between particle and background

hypothesis is not straightforward. Whereas the second variable gives the separation to the 2nd maximum LH: if the variable value is near 1, it means that the LH of the identified particle and that of another mass hypothesis are equal.

4.3.3 Cuts applied for the identification of pions

With the calculated p_{th_π} and the two likelihood variables, $\frac{LH_\pi}{LH_{back}}$ and $\frac{LH_\pi}{LH_{2^{nd}_{max}}}$, the following cuts are applied for the identification of pions:

- $p > p_{th_\pi} + 0.5$ GeV/c for pions, $(p_{th_\pi} = 2.5$ GeV/c),
- $\frac{LH_\pi}{LH_{back}} > 1.03$,
- $\frac{LH_\pi}{LH_{2^{nd}_{max}}} > 1.002$.

4.3.4 Cuts applied for the identification of kaons

Similarly with the calculated p_{th_K} and the two likelihood variables, $\frac{LH_K}{LH_{back}}$ and $\frac{LH_K}{LH_{2^{nd}_{max}}}$, the following cuts are applied for the identification of kaons:

- $p > p_{th_K} + 1.0$ GeV/c for kaons, $(p_{th_K} = 9$ GeV/c),
- $\frac{LH_K}{LH_{back}} > 1.04$,
- $\frac{LH_K}{LH_{2^{nd}_{max}}} > 1.003$.

4.3.5 Final data sample for RICH identified pions and kaons

Table. 4.3 shows the final statistics entering the analysis after all the above cuts were applied, for all the periods in 2003 and 2004, for positively and negatively charged pions and kaons.

4.4 Asymmetry calculation

In this section, eight target transverse spin dependent asymmetries are defined. Experimental extraction of raw asymmetries using ratio product method is explained along with the discussion on how the raw asymmetries are corrected with the relevant scaling factors to give physics asymmetries.

Year	Period	Positive pions	Negative pions	Positive kaons	Negative kaons
2003	P1G/P1H	1707142	1485228	309563	203485
2004	W33/W34	1536076	1328755	272068	176838
2004	W35/W36	2024054	1752848	359420	234662
Sum		5267272	4566831	941051	614985

Table 4.3: Final statistics for the years 2003 and 2004 for all pions and kaons

4.4.1 Calculation of the raw asymmetries

As it can be seen from the main equation for polarized SIDIS cross section, Eq. (2.64), The complete expression for the transverse interaction cross-section can be written as

$$
d\sigma(\phi_h, \phi_s, ...) \quad \propto \quad \left[1 + |\mathbf{S}_T| \sum_{i=1}^{5} D^{w_i(\phi_h,\phi_s)} A_{UT}^{w_i(\phi_h,\phi_s)} w_i(\phi_h, \phi_s) \right.
$$

$$
\left. + \quad P_{beam} |\mathbf{S}_T| \sum_{i=6}^{8} D^{w_i(\phi_h,\phi_s)} A_{LT}^{w_i(\phi_h,\phi_s)} w_i(\phi_h, \phi_s) \right]. \tag{4.4}
$$

Here $|\mathbf{S}_T|$ is the transverse polarization of the target, $D^{w_i(\phi_h,\phi_s)}$ defines the respective depolarization factor, $A_{UT}^{w_i(\phi_h,\phi_s)}$ defines the asymmetries with unpolarized beam (U) and transversely polarized target (T) similarly $A_{LT}^{w_i(\phi_h,\phi_s)}$ defines the asymmetries with longitudinally polarized beam (L) and transversely polarized target (T). The respective eight azimuthal modulations are given by,

$$
w_1(\phi_h, \phi_s) = \sin(\phi_h - \phi_s), \tag{4.5}
$$
$$
w_2(\phi_h, \phi_s) = \sin(\phi_h + \phi_s - \pi), \tag{4.6}
$$
$$
w_3(\phi_h, \phi_s) = \sin(3\phi_h - \phi_s), \tag{4.7}
$$
$$
w_4(\phi_h, \phi_s) = \sin(\phi_s), \tag{4.8}
$$
$$
w_5(\phi_h, \phi_s) = \sin(2\phi_h - \phi_s), \tag{4.9}
$$
$$
w_6(\phi_h, \phi_s) = \cos(\phi_h - \phi_s), \tag{4.10}
$$
$$
w_7(\phi_h, \phi_s) = \cos(\phi_s), \tag{4.11}
$$
$$
w_8(\phi_h, \phi_s) = \cos(2\phi_h - \phi_s) \tag{4.12}
$$

Now we can write two separate cross-sections for UT and LT asymmetries described by eight modulations $w_i(\phi_h, \phi_s)$, where i runs from 1 to 8 leads to the counting rate asymmetries of the form:

$$
\frac{d\sigma^{0\Uparrow} - d\sigma^{0\Downarrow}}{d\sigma^{0\Uparrow} + d\sigma^{0\Downarrow}} = A_{UT,\,raw}^{w_i(\phi_h,\phi_s)} \qquad i = 1, .., 5 \tag{4.13}
$$

$$
\frac{d\sigma^{\rightarrow\Uparrow} - d\sigma^{\rightarrow\Downarrow}}{d\sigma^{\rightarrow\Uparrow} + d\sigma^{\rightarrow\Downarrow}} = A_{LT,\,raw}^{w_i(\phi_h,\phi_s)} \qquad i = 6, .., 8 \tag{4.14}
$$

Here, 0 defines unpolarized beam whereas $\rightarrow$ defines the longitudinally polarized beam and $\Uparrow$ ($\Downarrow$) defines up (down) target polarization.

These eight modulations are based on 5 combinations of azimuthal hadron (ϕ_h) and spin (ϕ_s) angles which are:

$$\Phi_1 = \phi_h - \phi_s \tag{4.15}$$
$$\Phi_2 = \phi_h + \phi_s - \pi \tag{4.16}$$
$$\Phi_3 = 3\phi_h - \phi_s \tag{4.17}$$
$$\Phi_4 = \phi_s \tag{4.18}$$
$$\Phi_5 = 2\phi_h - \phi_s \tag{4.19}$$

With the five combinations, there are two (Φ_2, Φ_3) which do appear only in sin modulation, while the other three appear in the combination of sin and cos modulations. Therefore, we can define the five Φ_j dependent modulations

$$W_1(\Phi_1) = A_{raw}^{w_1(\phi_h,\phi_s)} \sin(\Phi_1) + A_{raw}^{w_6(\phi_h,\phi_s)} \cos(\Phi_1) \tag{4.20}$$
$$W_2(\Phi_2) = A_{raw}^{w_2(\phi_h,\phi_s)} \sin(\Phi_2) \tag{4.21}$$
$$W_3(\Phi_3) = A_{raw}^{w_3(\phi_h,\phi_s)} \sin(\Phi_3) \tag{4.22}$$
$$W_4(\Phi_4) = A_{raw}^{w_4(\phi_h,\phi_s)} \sin(\Phi_4) + A_{raw}^{w_7(\phi_h,\phi_s)} \cos(\Phi_4) \tag{4.23}$$
$$W_5(\Phi_5) = A_{raw}^{w_5(\phi_h,\phi_s)} \sin(\Phi_5) + A_{raw}^{w_8(\phi_h,\phi_s)} \cos(\Phi_5) \tag{4.24}$$

For each subperiod of our measurement and each target cell, we can now describe the counting rate dependence N(Φ_j) by:

$$N_{u/d}^{\pm}(\Phi_j) = f_{u/d}^{\pm} n_{u/d}^{\pm} a_{u/d}^{\pm}(\Phi_j) \sigma (1 \pm W_j(\Phi_j)) \tag{4.25}$$

where +(-) stands for up (down) target polarization and u(d) for the upstream and downstream target cells. σ is the unpolarized cross-section, while $f_{u/d}^{\pm}$ is the flux and $n_{u/d}^{\pm}$ the target density in the given target cell while measuring with the indicated polarization. Finally, $a_{u/d}^{\pm}(\Phi_j)$ is the acceptance for the same configurations depending, naturally, on Φ_j.

4.4.2 Calculation of the azimuthal angles ϕ_s and ϕ_h

The cross-section is defined with eight azimuthal modulations which are based on five combinations of azimuthal hadron angle ϕ_h and azimuthal spin angle ϕ_s (see Eqs. (4.15) - (4.19)). These modulations are usually defined in the Breit frame of the muon deep-inelastic scattering and it is calculated from the relevant vectors (momentum of the hadron and the nucleon spin) in that reference system. The Breit frame is the reference system in which xz plane is the μ scattering plane and z is defined by the virtual photon direction, the y axis is chosen in order to have a righthanded frame. The vectors must be transformed from the laboratory reference system (LS) to the Breit system, this procedure is performed in three steps [81].

1. From Laboratory System (LS) to Incident Muon reference system (IMS) : In the LS, the z axis is the nominal beam direction, the y axis is in vertical direction pointing upwards and the x axis is defined to get the righthanded frame. In the IMS, the z' axis defines the incident muon direction. Therefore the transformation is performed by a rotation of an angle $\phi_{\mu 1}$ around z followed by another rotation of an angle $\theta_{\mu 1}$ around the y' axis. ($\mu 1$ is the incident muon and $\mu 2$ is the scattered muon)

2. From IMS to $\gamma^* N$ reference system (GNS) : Here the z'' axis is defined by the direction of the virtual photon γ^*. The x'', y'' plane is the muon scattering plane and y'' axis is chosen to get a right handed frame. The transformation to GNS is done by a rotation of an angle $\theta'_{\mu 2}$ around the z' axis followed by another rotation of an angle $-\theta'_{\gamma *}$ around the y' axis.

3. From GNS to Breit system : A Lorentz transformation along the z'' axis is done in order to get the relevant vectors (i.e. the momentum of the hadron and the nucleon spin) in the Breit system. Definition of the azimuthal angles ϕ_s and ϕ_h for semi-inclusive deep inelastic scattering in the Breit frame is shown in Fig. 4.12.
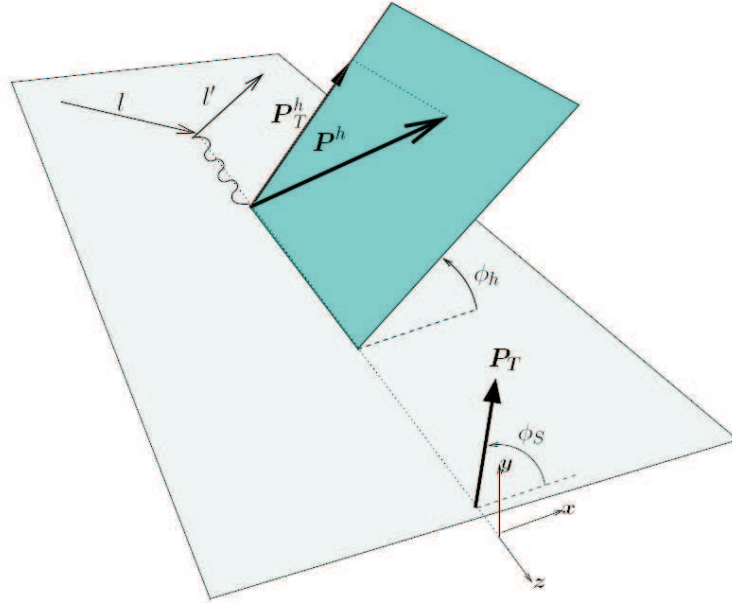
Figure 4.12: Definition of the azimuthal angles ϕ_s and ϕ_h for semi-inclusive deep inelastic scattering in the Breit frame

4.4.3 Determination of the raw asymmetries

As described in the section 4.1, the counting rate asymmetry is calculated between two periods with opposite polarization. In our case for the trasnversity data periods, the counting rate asymmetry is calculated between, the 2002 data acquisition periods: P2B and P2C, P2H.1 and P2H.2, the 2003 data acquisition periods: P1G and P1H, the 2004 data acquisition periods: W33 and W34, W35 and W36. A "ratio product method" is used to calculate all the raw asymmetries (described in the immediate section).

4.5 One-dimensional analysis

4.5.1 Ratio product method

In order to estimate the raw asymmetries from the measured number of events, a ratio product method has been used. This method minimizes the effect of possible acceptance variations. Using the Eq. (4.25), a double ratio can be constructed simultaneously with the information of both target cells (u, d) for two sub-periods and it is given by,

$$A(\Phi_j) = \frac{N_u^+(\Phi_j)N_d^+(\Phi_j)}{N_u^-(\Phi_j)N_d^-(\Phi_j)}, \tag{4.26}$$

with the respective error propagation:

$$\sigma_{A(\Phi_j)} = [A(\phi_j)] \cdot \sqrt{\frac{1}{N_u^+(\Phi_j)} + \frac{1}{N_d^+(\Phi_j)} + \frac{1}{N_u^-(\Phi_j)} + \frac{1}{N_d^-(\Phi_j)}}. \tag{4.27}$$

While testing this method, it was understood that for low statistics, the fit was biased i.e. the value $A(\Phi_j)$ of the ratio product method can exhibit large deviation from 1 due to large statistical fluctuations. Therefore to avoid any effect due to this bias, the value $A(\Phi_j)$ is replaced by 1. Now the formula to calculate the error can be written as

$$\sigma_{A(\Phi_j)} = \sqrt{\frac{1}{N_u^+(\Phi_j)} + \frac{1}{N_d^+(\Phi_j)} + \frac{1}{N_u^-(\Phi_j)} + \frac{1}{N_d^-(\Phi_j)}}. \tag{4.28}$$

Expanding Eq. (4.26) using Eq. (4.25), one gets:

$$A(\Phi_j) = \frac{f_u^+ n_u^+ a_u^+(\Phi_j)\sigma(1 + W_j(\Phi_j)) \cdot f_d^+ n_d^+ a_d^+(\Phi_j)\sigma(1 + W_j(\Phi_j))}{f_u^+ n_u^+ a_u^+(\Phi_j)\sigma(1 - W_j(\Phi_j)) \cdot f_d^+ n_d^+ a_d^+(\Phi_j)\sigma(1 - W_j(\Phi_j))}. \tag{4.29}$$

or

$$A(\Phi_j) = C_f \cdot C_a \cdot \frac{(1 + W_j(\Phi_j))(1 + W_j(\Phi_j))}{(1 - W_j(\Phi_j))(1 - W_j(\Phi_j))}. \tag{4.30}$$

Where

$$C_f = \frac{f_u^+ \cdot f_d^+}{f_u^- \cdot f_d^-}, \tag{4.31}$$

$$C_a = \frac{a_u^+(\Phi_j) \cdot a_d^+(\Phi_j)}{a_u^-(\Phi_j) \cdot a_d^-(\Phi_j)}. \tag{4.32}$$

We assume the reasonable assumption [77]:

$$\frac{a_u^+(\Phi_j)}{a_d^-(\Phi_j)} = \frac{a_u^-(\Phi_j)}{a_d^+(\Phi_j)} \tag{4.33}$$

i.e. that the ratio of acceptances between the upstream and downstream cells stays constant after spin reversal. Therefore C_a is equal to 1. The beam flux is expected to stay constant, therefore C_f is equal to 1. Therefore the asymmetries can be deduced from the double ratio using:

$$A(\Phi_j) = const \frac{(1 + W_j(\Phi_j))(1 + W_j(\Phi_j))}{(1 - W_j(\Phi_j))(1 - W_j(\Phi_j))}. \tag{4.34}$$

The double ratio is calculated in 16 equal bins over the range of Φ_j. The moments of Φ_j can now be deduced by individually performing two parameter fits. This method was implemented in the extraction of Collins ($\sin(\phi_h + \phi_s - \pi)$) and Sivers ($\sin(\phi_h - \phi_s)$) moments in [77].
For the sin modulation the fit is made with:

$$A(\Phi_j) = par(0)(1 + 4par(1)\sin\Phi_j). \tag{4.35}$$

and for the cos modulation:

$$A(\Phi_j) = par(0)(1 + 4par(1)\cos\Phi_j). \tag{4.36}$$

In the cases, where $W_j(\Phi_j)$ depends on both, sin and cos modulations, it can be easily seen, that also a 3 parameter fit can be performed to extract both moments simultaneously:

$$A(\Phi_j) = par(0)(1 + 4par(1)\sin\Phi_j + 4par(2)\cos\Phi_j). \tag{4.37}$$

In both cases, par(0) is the above mentioned constant and par(1) (as well as par(2) for the 3 parameter fit) give the raw "asymmetries".

4.5.2 From the raw asymmetry to the corrected asymmetry

The objective is to gain from the raw asymmetries, an insight into the real physics asymmetries. The final eight TMD asymmetries which are related to the relevant raw asymmetries with their respective scaling factor are discussed below. The scaling factors are namely the dilution factor f, the target polarization $|P_T|$, the beam polarization P_{beam} and the depolarization factor $D^{w_i}(y)$. A short description of those correction factors are discussed in the immediate sections.

- $A_{UT}^{\sin(\phi_h+\phi_s-\pi)}$ **asymmetry (Collins) :** The Collins asymmetry is extracted from the raw asymmetry through the expression

$$A_{UT}^{\sin(\phi_h+\phi_s-\pi)} = \frac{A_{UT,raw}^{\sin(\phi_h+\phi_s-\pi)}}{D^{\sin(\phi_h+\phi_s)}(y) \cdot f \cdot |P_T|}. \tag{4.38}$$

- $A_{UT}^{\sin(3\phi_h-\phi_s)}$ **asymmetry :** Similar to Collins asymmetry, this asymmetry is extracted from the raw asymmetry through the expression

$$A_{UT}^{\sin(3\phi_h-\phi_s)} = \frac{A_{UT,raw}^{\sin(3\phi_h-\phi_s)}}{D^{\sin(3\phi_h+\phi_s)}(y) \cdot f \cdot |P_T|}. \tag{4.39}$$

- $A_{UT}^{sin(\phi_h-\phi_s)}$ **asymmetry (Sivers):** Sivers asymmetry is extracted from the raw asymmetry through the expression

$$A_{UT}^{\sin(\phi_h-\phi_s)} = \frac{A_{UT,raw}^{\sin(\phi_h-\phi_s)}}{D^{\sin(\phi_h-\phi_s)}(y) \cdot f \cdot |P_T|}. \tag{4.40}$$

- $A_{LT}^{\cos(\phi_h-\phi_s)}$ **asymmetry :** This asymmetry is extracted from the raw asymmetry through the expression

$$A_{LT}^{\cos(\phi_h-\phi_s)} = \frac{A_{LT,raw}^{\cos(\phi_h-\phi_s)}}{D^{\cos(\phi_h-\phi_s)}(y) \cdot f \cdot |P_T| \cdot |P_{beam}|}. \tag{4.41}$$

- $A_{UT}^{\sin(\phi_s)}$ **asymmetry :** This asymmetry is extracted from the raw asymmetry through the expression

$$A_{UT}^{\sin(\phi_s)} = \frac{A_{UT,raw}^{\sin(\phi_s)}}{D^{\sin(\phi_s)}(y) \cdot f \cdot |P_T|}. \tag{4.42}$$

- $A_{UT}^{\sin(2\phi_h-\phi_s)}$ **asymmetry :** This asymmetry is extracted from the raw asymmetry through the expression

$$A_{UT}^{\sin(2\phi_h-\phi_s)} = \frac{A_{UT,raw}^{\sin(2\phi_h-\phi_s)}}{D^{\sin(2\phi_h-\phi_s)}(y) \cdot f \cdot |P_T|}. \tag{4.43}$$

- $A_{LT}^{\cos(\phi_s)}$ **asymmetry :** This asymmetry is extracted from the raw asymmetry through the expression

$$A_{LT}^{\cos(\phi_s)} = \frac{A_{LT,raw}^{\cos(\phi_s)}}{D^{\cos(\phi_s)}(y) \cdot f \cdot |P_T| \cdot |P_{beam}|}. \tag{4.44}$$

- $A_{LT}^{\cos(2\phi_h-\phi_s)}$ **asymmetry :** This asymmetry is extracted from the raw asymmetry through the expression

$$A_{LT}^{\cos(2\phi_h-\phi_s)} = \frac{A_{LT,raw}^{\cos(2\phi_h-\phi_s)}}{D^{\cos(2\phi_h-\phi_s)}(y) \cdot f \cdot |P_T| \cdot |P_{beam}|}. \tag{4.45}$$

4.6 Target polarization P_T

A direct measurement of target polarization at COMPASS is not possible in transverse mode. The polarization is measured in the longitudinal 2.5 T field at the beginning and the end of each transverse data acquisition period. Measured values for the COMPASS target polarization in the transverse data acquisition periods are given in Table. 4.4

Period	Runs	Upstream	Downstream
P2B	21178-21207	-49.79	54.58
P2B	21333-21393	-47.79	47.40
P2B	21407-21495	-47.09	46.33
P2C	21670-21765	52.50	-44.09
P2C	21777-21878	50.36	-43.06
P2H.1	23490-23575	-49.83	52.11
P2H.2	23664-23839	47.45	-41.41
P1G	30772-31038	-49.70	+52.78
P1H	31192-31247	+49.39	-42.60
P1H	31277-31524	+51.31	-44.63
W33	38991-39168	+50.70	-43.52
W34	39283-39290	-44.80	+45.97
W34	39325-39430	-38.60	+40.35
W34	39480-39545	-46.14	+47.41
W35	39548-39780	-46.44	+47.44
W36	39850-39987	+49.89	-42.76

Table 4.4: Target polarization values for 2002 - 2004 transversity data acquisition periods

4.7 Dilution factor f

The dilution factor f is introduced to estimate how much material in the target can be polarized. In the case of the COMPASS ^{6}LiD target, four nucleons out of eight can be polarized (see section 3.3). Thus the maximal fraction of the polarizable material to the total material is $f = 0.5$. As the current COMPASS target was inherited from the SMC experiment, calculations from SMC regarding the real dilution factor could be modified for the COMPASS kinematics [82]. The factor is found to vary slightly with x, with a value in the relevant range of just under 0.4. For the analysis, a constant value of $f = 0.38$ was assumed

4.8   Depolarization factor

The depolarization factor is calculated from the kinematics of each event in the data sample. According to the run it occurs in and the target cell where the vertex is found, depolarization factor is then multiplied by the appropriate value for the polarization from Table. 4.4. It is then used to weight the event. In total there are eight raw asymmetries extracted and six different depolarization factors are evaluated as two asymmetries have the same depolarization factor. The evaluated depolarization factors depend only on y for the transverse case (see section 2.4.1) and are given by

$$D^{\sin(\phi_h - \phi_s)}(y) = 1, \tag{4.46}$$

$$D^{\sin(\phi_h + \phi_s)}(y) = D^{\sin(3\phi_h + \phi_s)}(y) = D_{NN}(y) = \frac{2(1-y)}{1 + (1-y)^2}, \tag{4.47}$$

$$D^{\sin(2\phi_h - \phi_s)}(y) = D^{\sin(\phi_s)}(y) = \frac{2(2-y)\sqrt{1-y}}{1 + (1-y)^2}, \tag{4.48}$$

$$D^{\cos(\phi_h - \phi_s)}(y) = D(y) = \frac{y(2-y)}{1 + (1-y)^2}, \tag{4.49}$$

$$D^{\cos(2\phi_h - \phi_s)}(y) = D^{\cos(\phi_s)}(y) = \frac{2y\sqrt{1-y}}{1 + (1-y)^2}. \tag{4.50}$$

4.9   Binning

All the eight TMD asymmetries are calculated separately in different kinematic regions in x, z and p_t. The bins chosen over the range of x, z and p_t are given below.

$0.003 <$	x_{Bj}	< 0.008				$0.10 <$	p_t	≤ 0.20
$0.008 \leq$	x_{Bj}	< 0.013	$0.20 \leq$	z	< 0.25	$0.20 <$	p_t	≤ 0.30
$0.013 \leq$	x_{Bj}	< 0.020	$0.25 \leq$	z	< 0.30	$0.30 <$	p_t	≤ 0.40
$0.020 \leq$	x_{Bj}	< 0.032	$0.30 \leq$	z	< 0.35			
$0.032 \leq$	x_{Bj}	< 0.050	$0.35 \leq$	z	< 0.40	$0.40 <$	p_t	≤ 0.50
$0.050 \leq$	x_{Bj}	< 0.080	$0.40 \leq$	z	< 0.50	$0.50 <$	p_t	≤ 0.60
$0.080 \leq$	x_{Bj}	< 0.130	$0.50 \leq$	z	< 0.65	$0.60 <$	p_t	≤ 0.75
$0.130 \leq$	x_{Bj}	< 0.210	$0.65 \leq$	z	< 0.80	$0.75 <$	p_t	≤ 0.90
$0.210 \leq$	x_{Bj}	< 1.000	$0.80 \leq$	z	< 1.00	$0.90 <$	p_t	≤ 1.30
						$1.30 <$	p_t	$\leq$ end.

Calculated asymmetries are then plotted against x, z and p_t accordingly.

4.10 Results for the extracted eight TMD asymmetries

Eight TMD Asymmetries with unidentified hadrons, RICH identified pions and kaons were extracted. Asymmetries with unidentified hadrons are with the COMPASS 2002 -2004 data sample whereas asymmetries with RICH identified pions and kaons are with the COMPASS 2003 - 2004 data sample [83]. The asymmetries were extracted using information from both target cells for the paired periods P2B/C, P2H.1/H.2, P1G/H, W33/4 and W35/6. Therefore they should be combined with an appropriate weighting. The final weighted asymmetry for RICH identified pions and kaons for the paired periods P1G/H, W33/4 and W35/6 is calculated with the formula:

$$A_W = \frac{\left[\left(\frac{1}{\sigma_{P1G/H}^2} \cdot A_{P1G/H}\right) + \left(\frac{1}{\sigma_{W33/4}^2} \cdot A_{W33/4}\right) + \left(\frac{1}{\sigma_{W35/6}^2} \cdot A_{W35/6}\right)\right]}{\left[\frac{1}{\sigma_{P1G/H}^2} + \frac{1}{\sigma_{W33/4}^2} + \frac{1}{\sigma_{W35/6}^2}\right]}. \quad (4.51)$$

The statistical error σ_W on the weighted asymmetry can be calculated accordingly from the statistical error on the period asymmetries :

$$\sigma_{A_W} = \frac{1}{\sqrt{\frac{1}{\sigma_{P1G/H}^2} + \frac{1}{\sigma_{W33/4}^2} + \frac{1}{\sigma_{W35/6}^2}}}. \quad (4.52)$$

Similar formalism is used to calculate weighted asymmetry for unidentified hadrons including the data periods in 2002 (P2B/C and P2H.1/P2H.2). The weighted asymmetry A_W and its respective statistical error σ_{A_W} is calculated for each bin (see section 4.9) in x, z and p_t accordingly. This calculation is performed for all eight TMD asymmetries for unidentified hadrons (positive and negative), identified pions (positive and negative) and identified kaons (positive and negative).

Figs. 4.13 - 4.20 shows the extracted eight TMD asymmetries for unidentified hadrons, pions and kaons. All asymmetries are plotted as a function of x, z and P_T^h. The red circles shows the results for positive hadrons, (pions and kaons) whereas blue triangles shows the results for negative hadrons, (pions and kaons). The error bars shown in all the plots are statistical only. In all the plots the blue triangles are slightly shifted horizontally with the respect to the measured value.

Collins asymmetry with COMPASS data
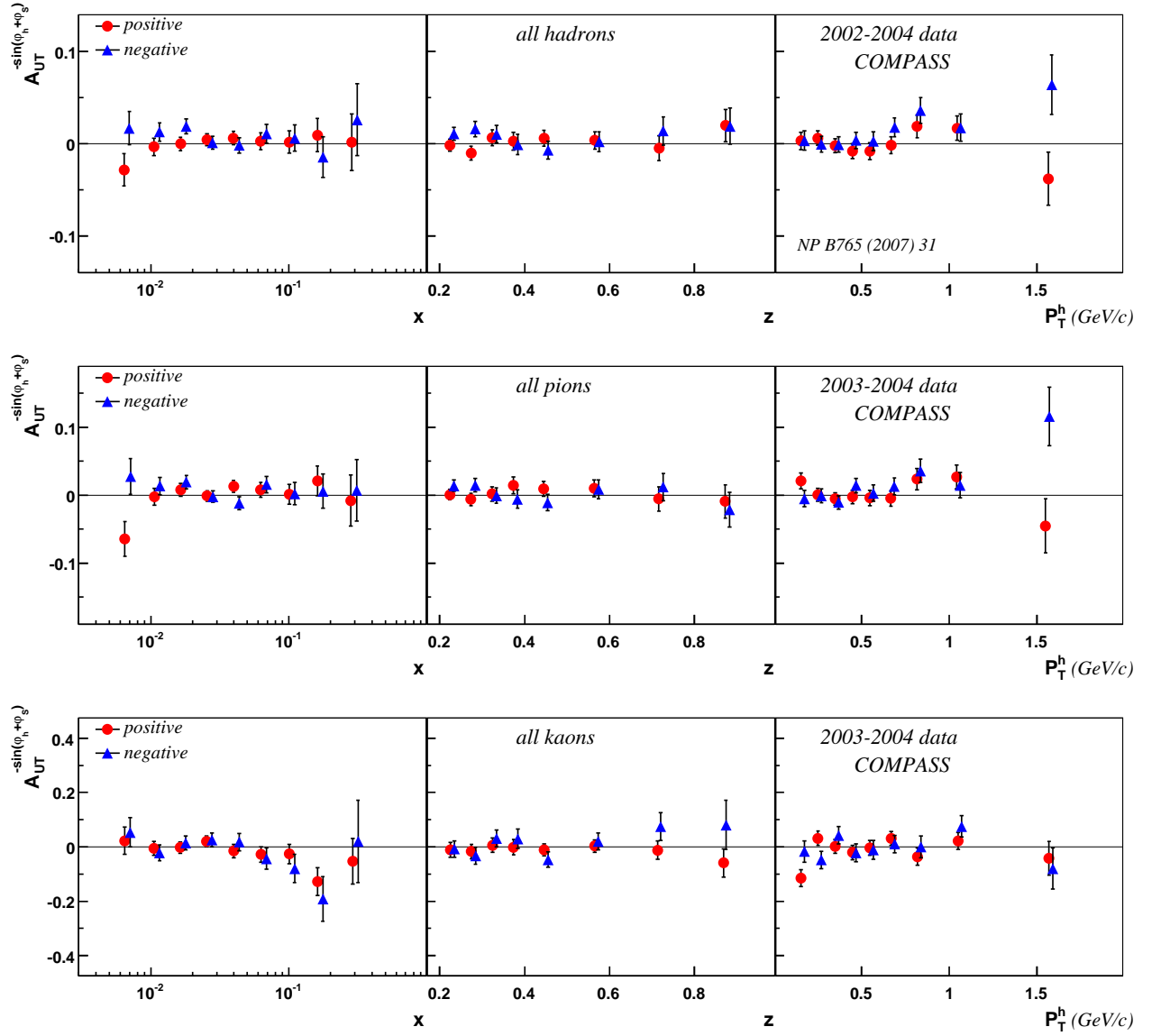
Figure 4.13: Extracted Collins asymmetry ($A_{UT}^{\sin(\phi_h + \phi_s - \pi)}$) for unidentified hadrons (top row), pions (middle row) and kaons (bottom row) as a function of x, z and P_T^h

Sivers asymmetry with COMPASS data
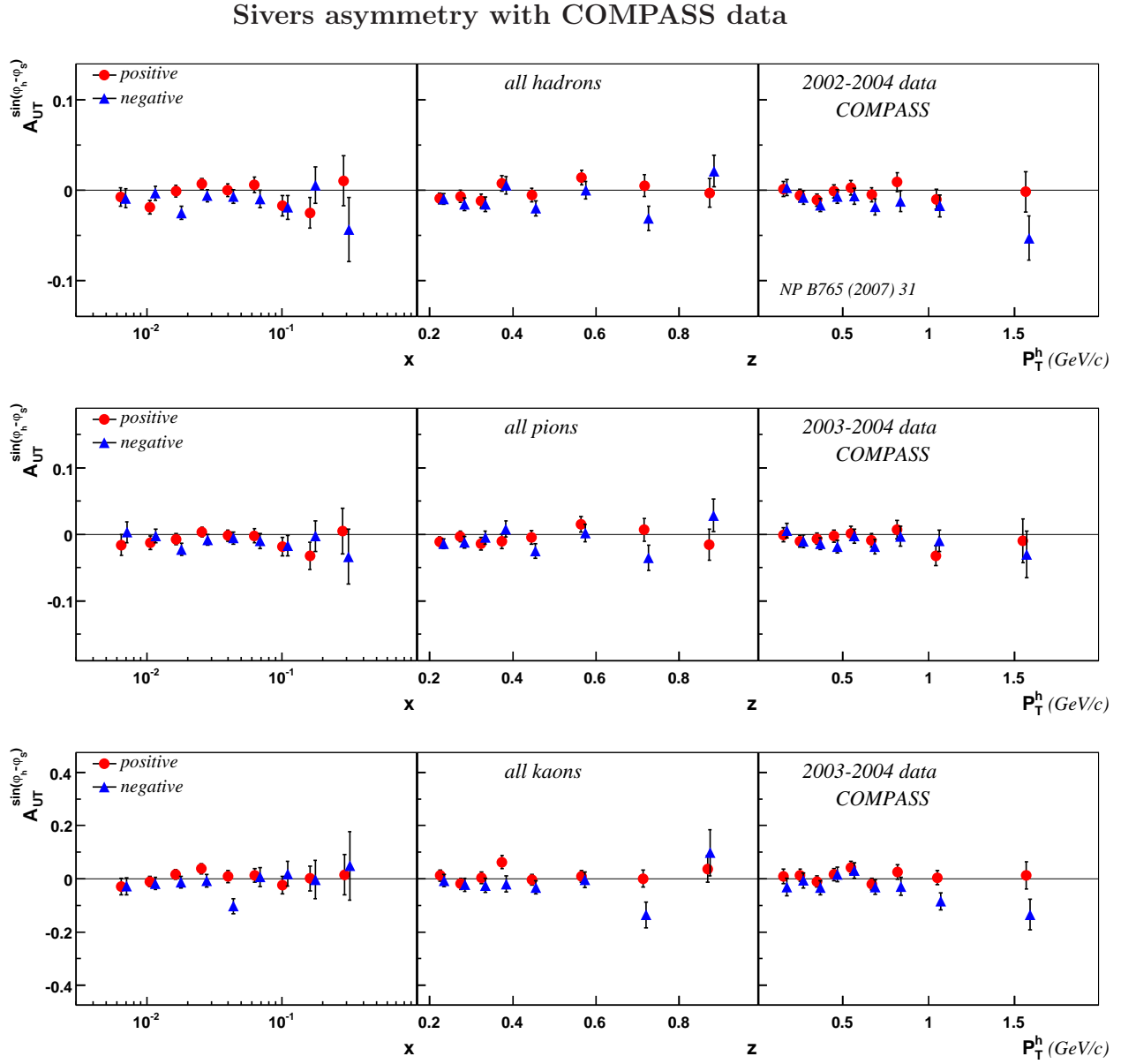
Figure 4.14: Extracted Sivers asymmetry ($A_{UT}^{sin(\phi_h - \phi_s)}$) for unidentified hadrons (top row), pions (middle row) and kaons (bottom row) as a function of x, z and P_T^h

$A_{LT}^{\cos(\phi_h - \phi_s)}$ **asymmetry with COMPASS data**
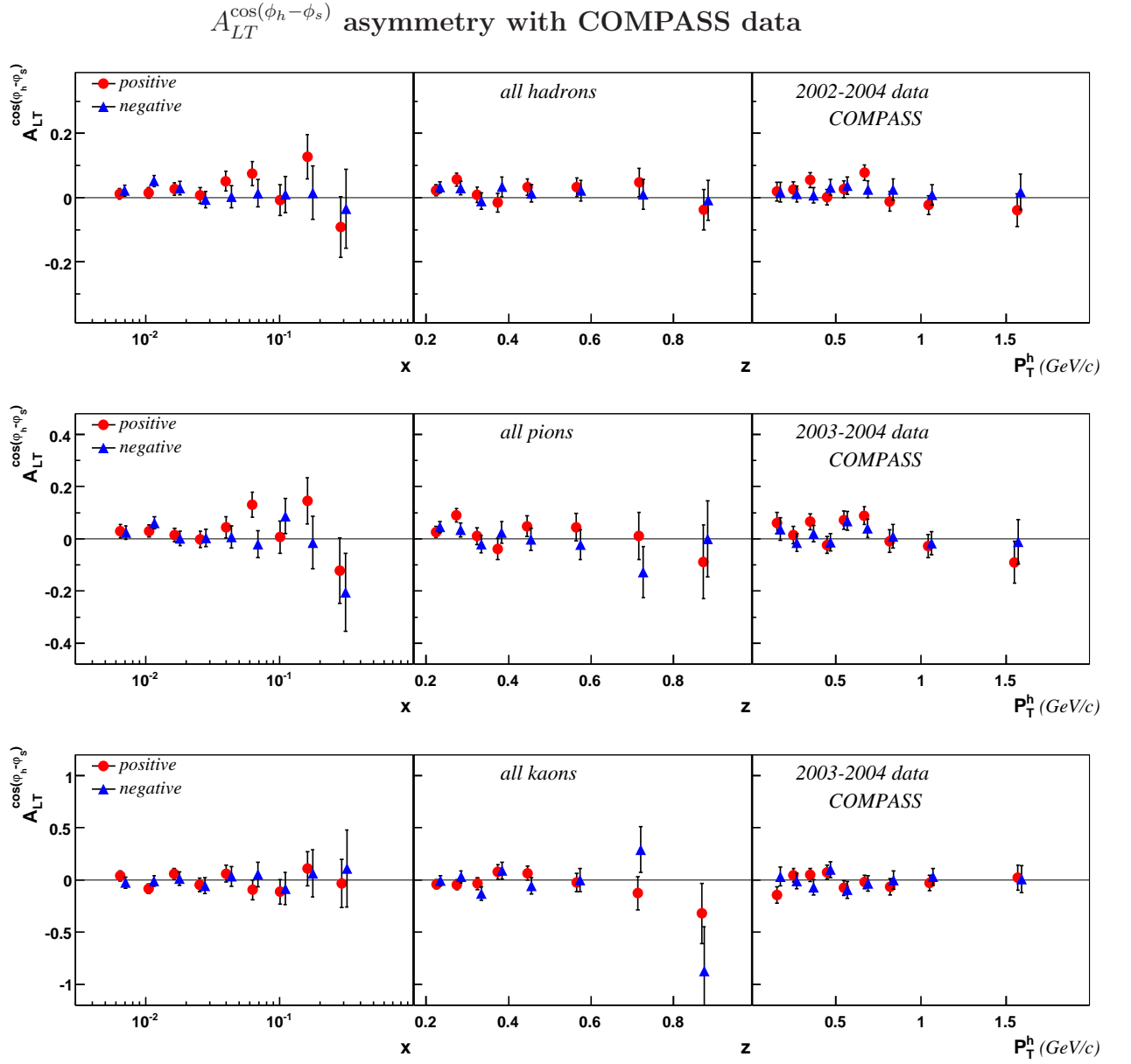
Figure 4.15: Extracted $A_{LT}^{\cos(\phi_h - \phi_s)}$ asymmetry for unidentified hadrons (top row), pions (middle row) and kaons (bottom row) as a function of x, z and P_T^h

$A_{UT}^{\sin(3\phi_h - \phi_s)}$ **asymmetry with COMPASS data**
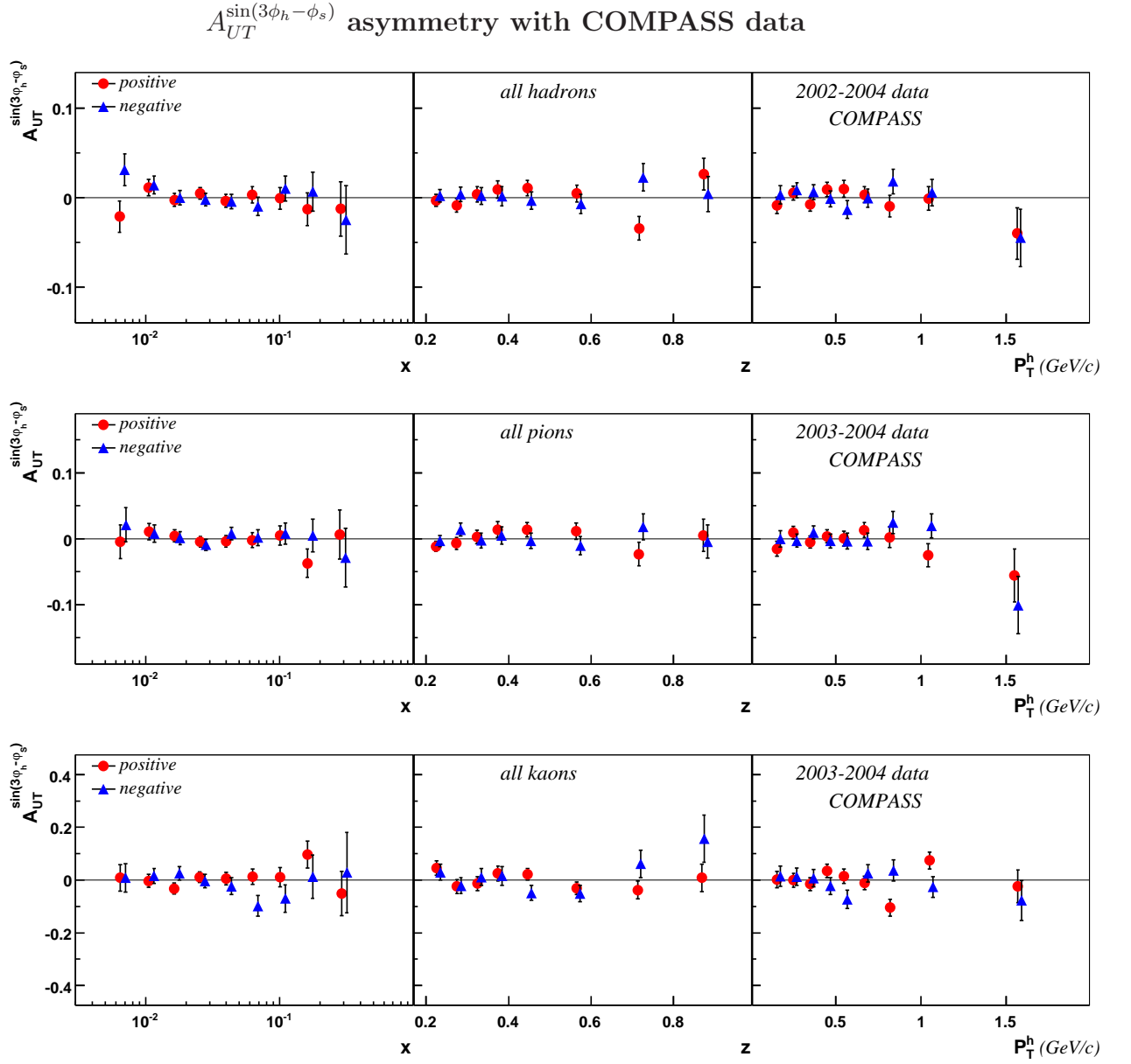
Figure 4.16: Extracted $A_{UT}^{\sin(3\phi_h - \phi_s)}$ asymmetry for unidentified hadrons (top row), pions (middle row) and kaons (bottom row) as a function of x, z and P_T^h

$A_{UT}^{\sin(\phi_s)}$ **asymmetry with COMPASS data**
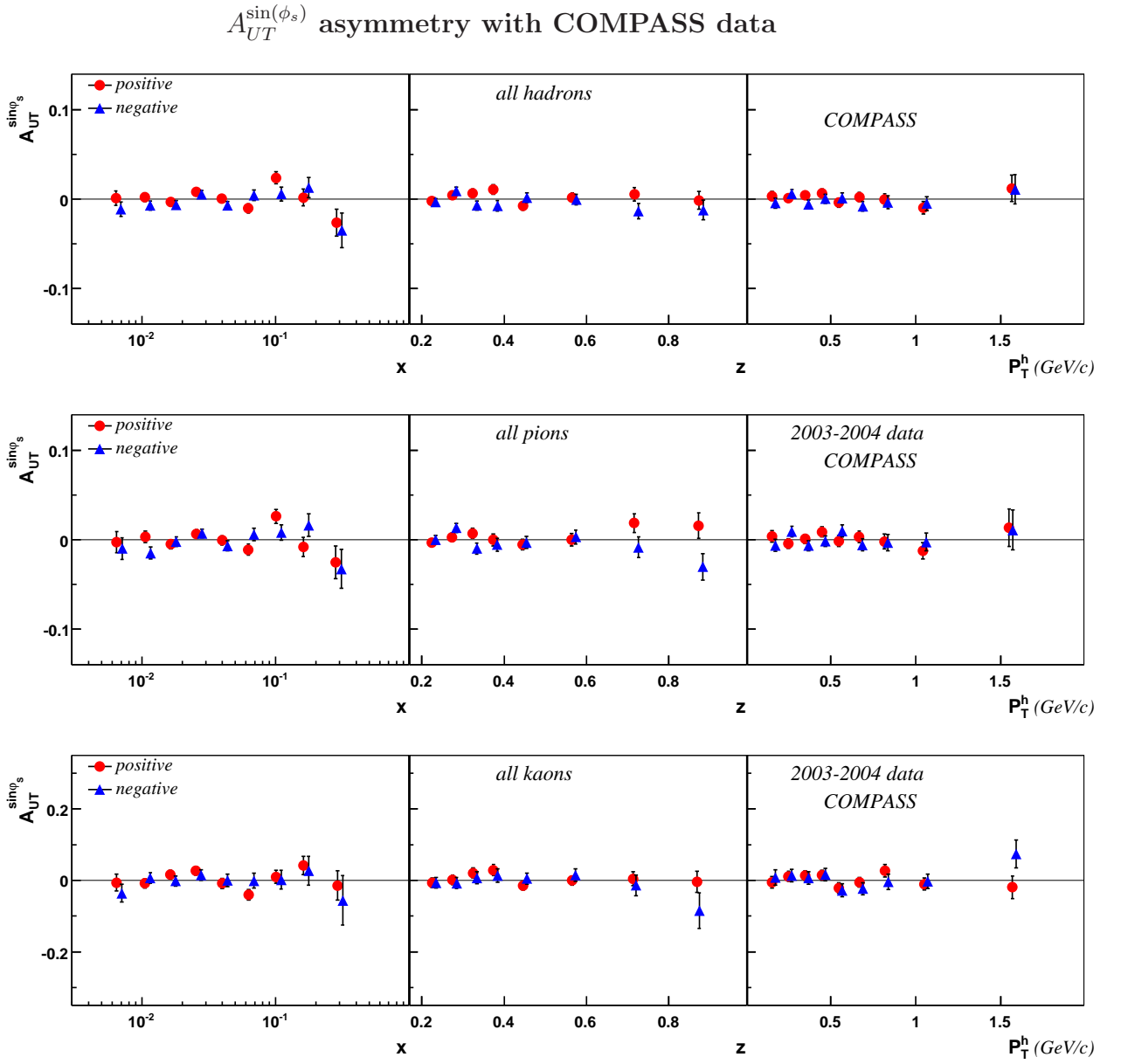
Figure 4.17: Extracted $A_{UT}^{\sin(\phi_s)}$ asymmetry for unidentified hadrons (top row), pions (middle row) and kaons (bottom row) as a function of x, z and P_T^h

$A_{UT}^{\sin(2\phi_h-\phi_s)}$ **asymmetry with COMPASS data**
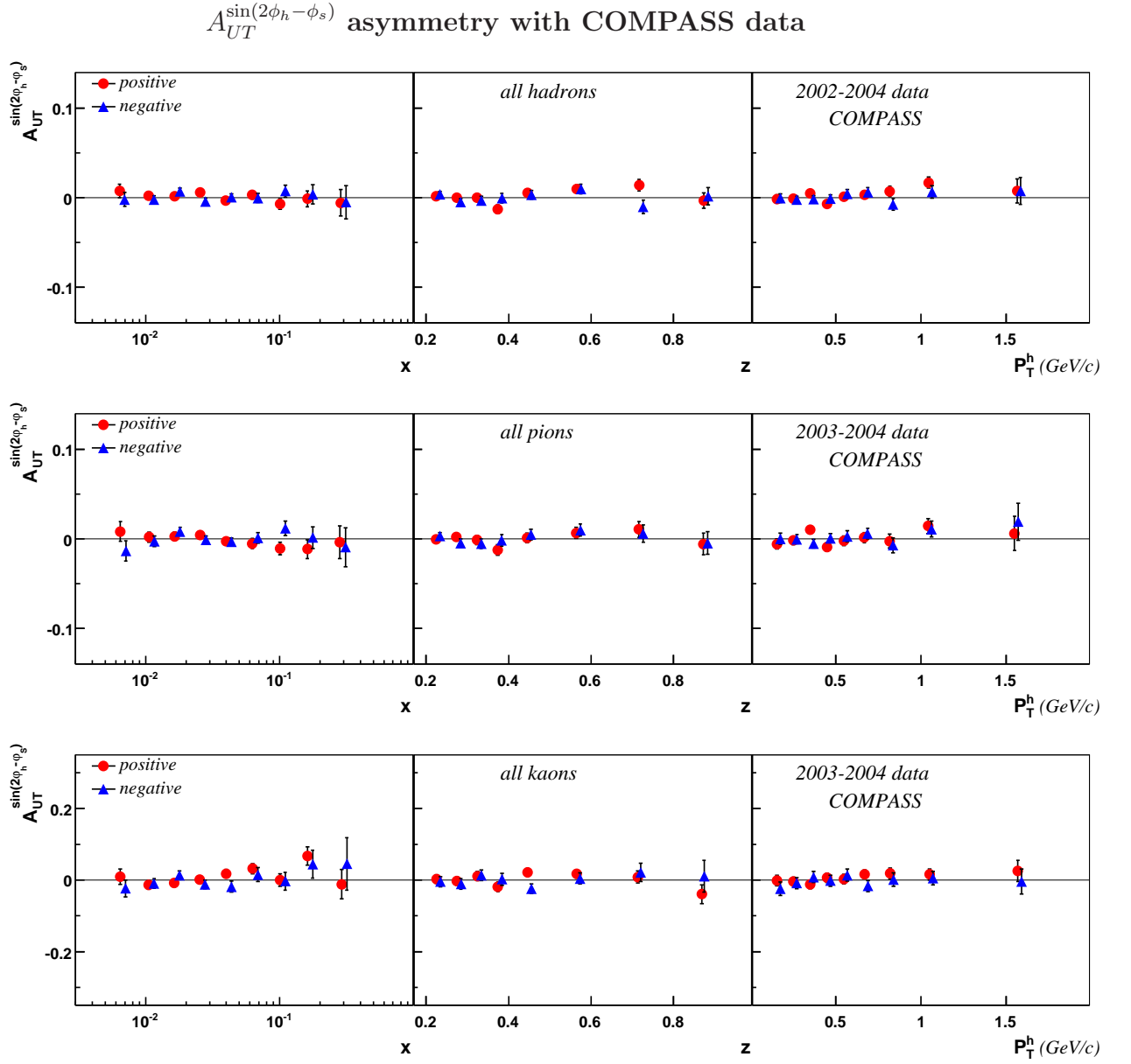
Figure 4.18: Extracted $A_{UT}^{\sin(2\phi_h-\phi_s)}$ asymmetry for unidentified hadrons (top row), pions (middle row) and kaons (bottom row) as a function of x, z and P_T^h

$A_{LT}^{\cos(\phi_s)}$ **asymmetry with COMPASS data**
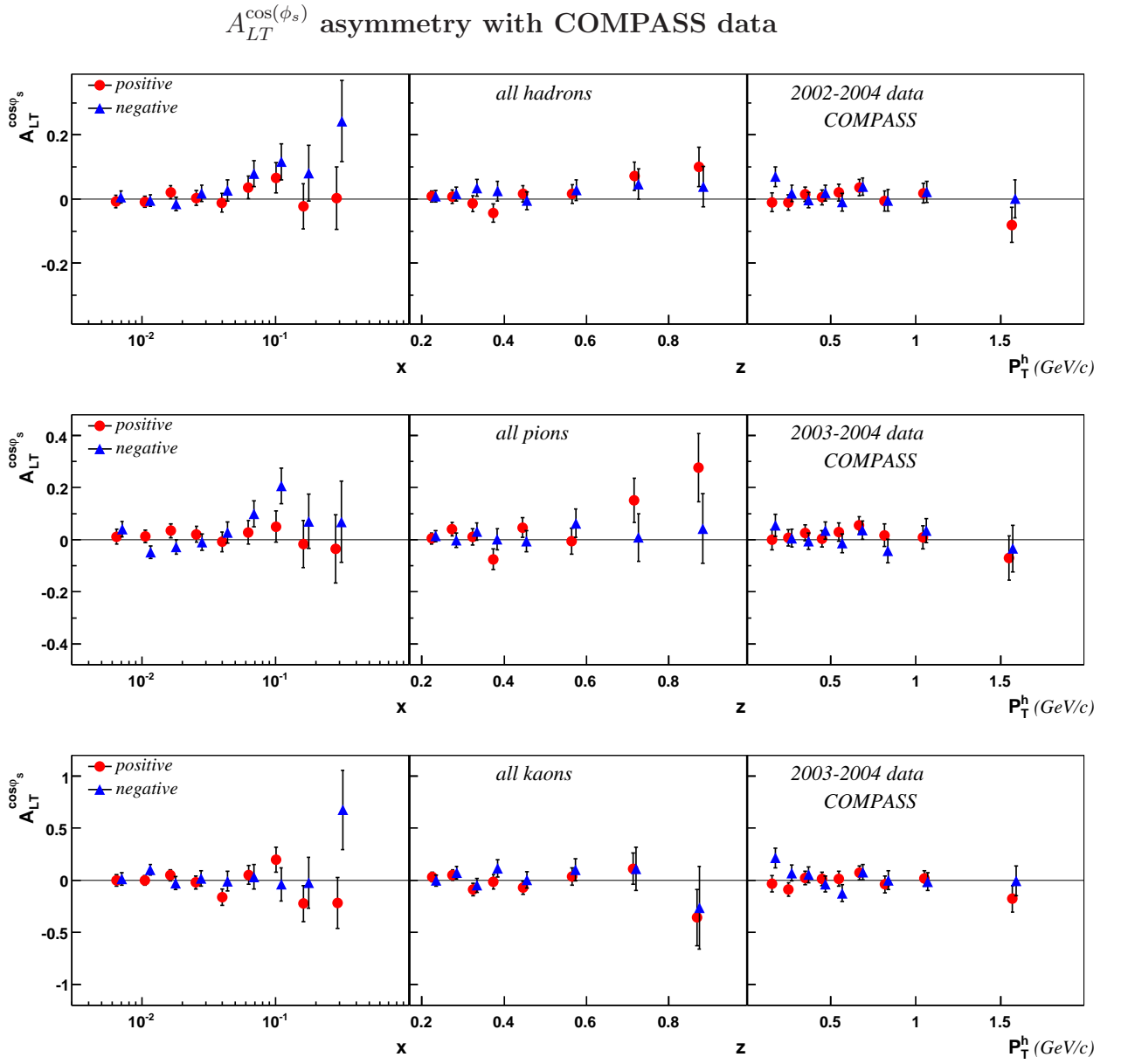
Figure 4.19: Extracted $A_{LT}^{\cos(\phi_s)}$ asymmetry for unidentified hadrons (top row), pions (middle row) and kaons (bottom row) as a function of x, z and P_T^h

$A_{LT}^{\cos(2\phi_h - \phi_s)}$ **asymmetry with COMPASS data**
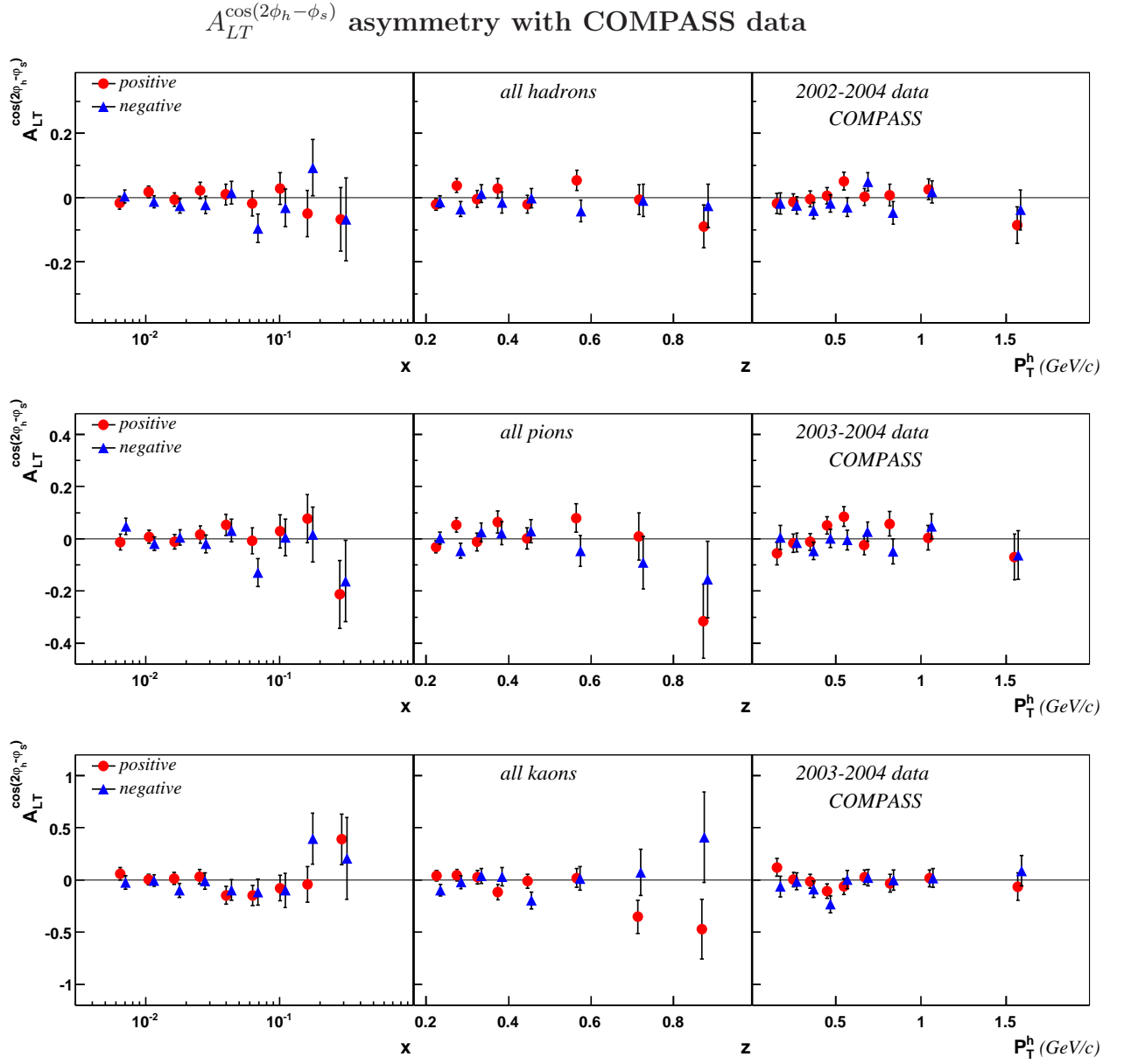
Figure 4.20: Extracted $A_{LT}^{\cos(2\phi_h - \phi_s)}$ asymmetry for unidentified hadrons (top row), pions (middle row) and kaons (bottom row) as a function of x, z and P_T^h

4.11 Estimation of the systematic errors

Several tests were performed to test the stability of the detector essential for our data analysis. The main objective here is to evaluate the sources and to quantify the size of our systematic errors. The tests performed are, checking the compatibility of the results obtained from different periods, checking the stability of the acceptance ratios and finally estimating the value of free parameter par(0) used in the fitting function.

The following systematic studies were performed for unidentified hadrons with the COMPASS 2002 - 2004 data sample and for identified pions and kaons with the COMPASS 2003 - 2004 data sample, but only the results performed for identified pions and koans with COMPASS 2003 - 2004 data sample is presented as the systematic studies performed for unidentified hadron sample shows similar trends.

4.11.1 Compatibility of the results from different periods

The compatibility of the final asymmetries in each x, z and p_t bin obtained in three data acquisition periods from 2003-2004 has been checked by building the "pulls" distribution.

$$\frac{A_i - <A>}{\sqrt{\sigma_i^2 - \sigma_{<A>}^2}} \tag{4.53}$$

where i $= 1$ to 3 for 3 periods, A_i are the asymmetries and $<A>$ is the corresponding weighted mean. In the denominator we have used the variances to take into account the correlation between A_i and $<A>$. As expected, these pulls follow within the errors of a standard normal distribution. Figure. 4.21 is a "pulls" distribution to show the compatibility of results from different periods with x, z and p_t. Figure. 4.22 is an overall pulls distribution of asymmetries for all different measurements, such as all the eight asymmetries with positive and negative pions and kaons, x, z, p_t for three data acquisition periods. The number of entries involved in estimating the overall pulls distribution are 2496. Combining the bins for x, z and p_t will give in total of 26 bins (9 bins in x + 8 bins in z + 9 bins in p_t). In total there are eight asymmetries (26 x 8 = 208) calculated for two charged particles (pions and kaons) (208 x 2 = 416), it is estimated for positive and negative particle (416 x 2 = 832), finally for three paired data periods P1G/H, W33/4, and W35/6 (832 x 3 = 2496).

As expected, pulls shown in Figs 4.21 and 4.22 follow a standard normal distribution within errors. This confirms that the results obtained with different data acquisition periods are compatible.

4.11.2 Stability of acceptance ratios

A stringent test on the Φ_j dependence of the acceptance ratio is performed. For the ratio test the count rates used to calculate the asymmetries in the double ratio
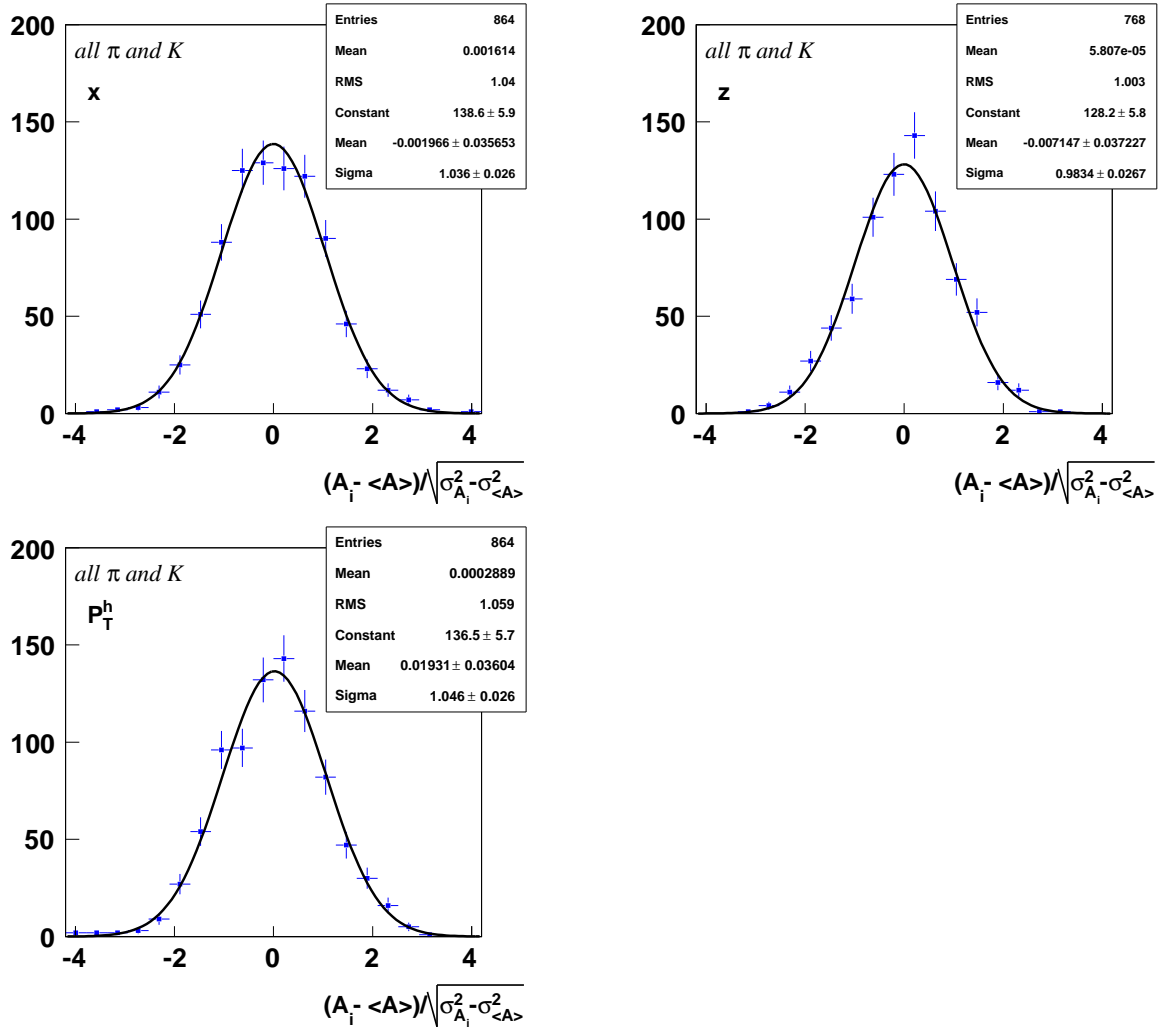
Figure 4.21: Compatibility of the results from different periods: "pulls" distribution to see the compatibility of results from different periods with x(top left), z(top right) and p_t(bottom).

method (see Eq. (4.34)) is:

$$A(\Phi_j) = \frac{N_u^+(\Phi_j)N_d^+(\Phi_j)}{N_u^-(\Phi_j)N_d^-(\Phi_j)}. \tag{4.54}$$

The above equation is rearranged in such a way that we create a ratio:

$$R(\Phi_j) = \frac{N_u^+(\Phi_j)N_d^-(\Phi_j)}{N_u^-(\Phi_j)N_d^+(\Phi_j)}. \tag{4.55}$$

Assuming the absolute value of the target polarization to be the same in each cell before and after reversal, at the first order it is:

$$R(\Phi_j) \simeq \frac{f_u^+ \cdot f_d^-}{f_u^- \cdot f_d^+} \cdot \frac{a_u^+(\Phi_j) \cdot a_d^-(\Phi_j)}{a_u^-(\Phi_j) \cdot a_d^+(\Phi_j)} \tag{4.56}$$
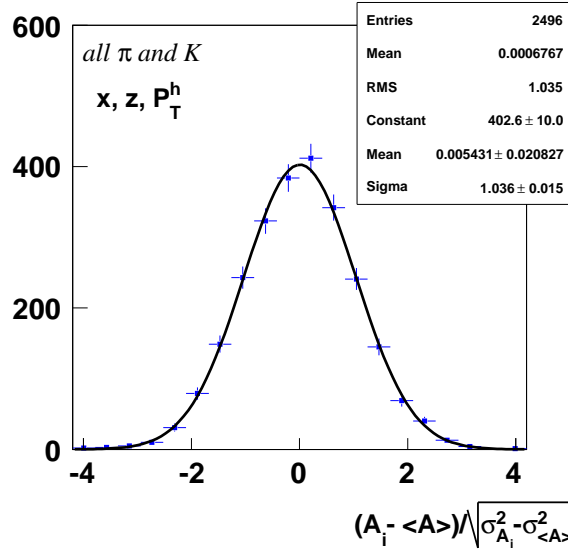
Figure 4.22: Compatibility of the results from different periods: "pulls" distribution of asymmetries for all different measurements, such as all 8 asymmetries with positive and negative pions and kaons, x, z, p_t, for 3 data taking periods..

In the very likely case in which

$$\frac{a_u^+(\Phi_j)}{a_d^-(\Phi_j)} = \frac{a_u^-(\Phi_j)}{a_d^+(\Phi_j)} \tag{4.57}$$

then,

$$R(\Phi_j) \quad \simeq \quad \frac{f_u^+ \cdot f_d^-}{f_u^- \cdot f_d^+} \cdot \left(\frac{a_u^+(\Phi_j)}{a_u^-(\Phi_j)}\right)^2 \tag{4.58}$$

$$\simeq \quad \frac{f_u^+ \cdot f_d^-}{f_u^- \cdot f_d^+} \cdot \left(\frac{a_d^-(\Phi_j)}{a_d^+(\Phi_j)}\right)^2 \tag{4.59}$$

Thus the constancy in Φ_j of $R(\Phi_j)$ is a stronger assumption than the required reasonable assumption (see Eq. (4.33)), and it implies for each cell the ratio of the acceptances before and after the reversal to be constant in Φ_j. Ensures that the spectrometer was stable during the running period. The ratio was calculated in each bin of x, z and p_t variables of all the 8 asymmetries separately for pions and kaons. Figs. 4.23 and 4.24 show an example of the R-values for $(3\phi_h - \phi_s)$ modulation vs. x for positive pions and kaons for the period W35/W36. The line shows the result of a constant fit.

The quality of these fits are very good. To test this, the χ^2 of each fit was determined. Fig. 4.25 show the distribution of the χ^2 values of the constant fits on $R(\Phi_j)$ values evaluated for "all" positive and negative pions and kaons, all kinematical bins from all data taking periods for $(3\phi_h - \phi_s)$ modulation, and it is
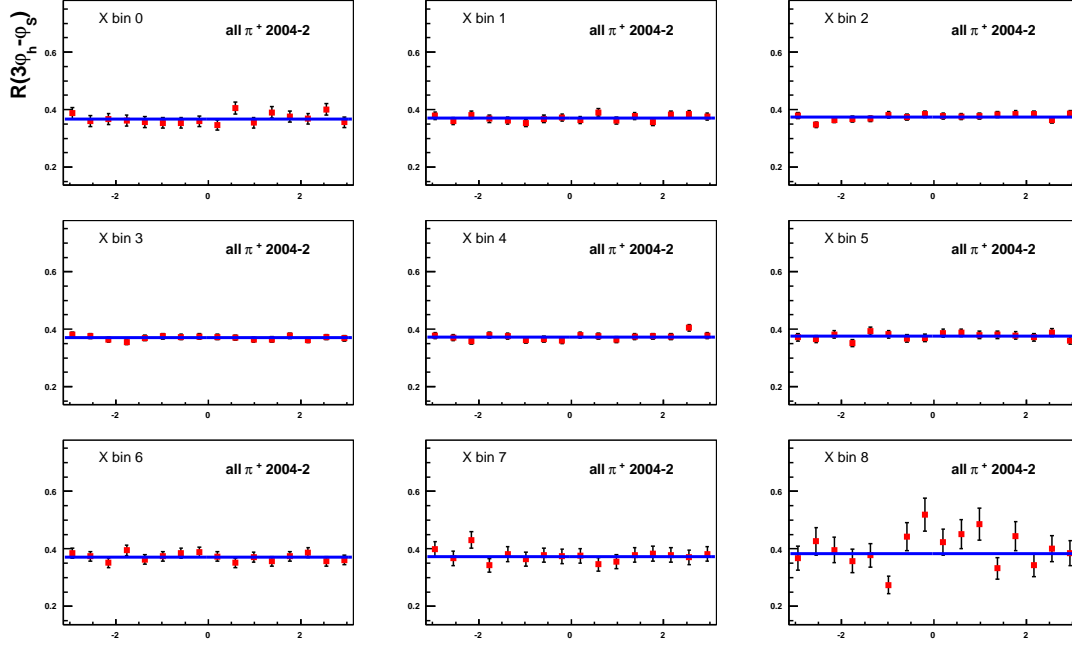
Figure 4.23: Distribution of the R-values vs x in $(3\phi_h - \phi_s)$ modulation for the period W35/W36 for positive pions.

compared with the expected χ^2 distribution for $\nu = 15$ degrees of freedom (constant fit on 16 Φ bins) normalized to the number of entries. A nearly perfect agreement of data and expected behavior is observed.

For comparison, Fig. 4.26 shows the χ^2 distribution of the two parameter fit on the asymmetry $A(\Phi_j)$ values for $(3\phi_h - \phi_s)$ modulation. Here the curve gives the expected χ^2 distribution for 14 degrees of freedom. A perfect agreement can be observed.

To summarize, this performed test on the effects of acceptance gave results statistically compatible with what expected in the absence of systematic effects.

4.11.3 par(0) calculation

The parameter par(0) is the free parameter used in the fitting procedure for both one-dimensional (see Eqs. (4.35), (4.36) and (4.37)) and two-dimensional case (explained in next section). par(0) should remain constant with the value 1 proving if our assumptions of the double ratio method are true. The value for par(0) is deduced, as we did for other parameters for all the five $W_j(\Phi_j)$ modulations (see Eqs. (4.20) - (4.24)), all positive and negative pions and kaons, for all the periods and all x, z
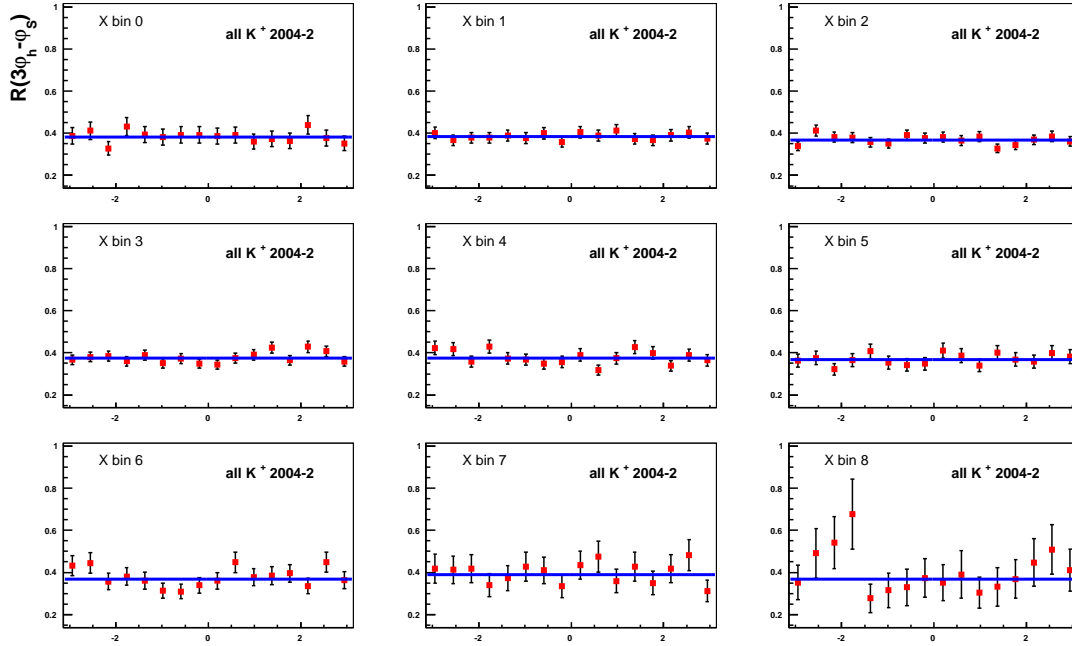
Figure 4.24: Distribution of the R-values vs x in $(3\phi_h - \phi_s)$ modulation for the period W35/W36 for positive kaons.
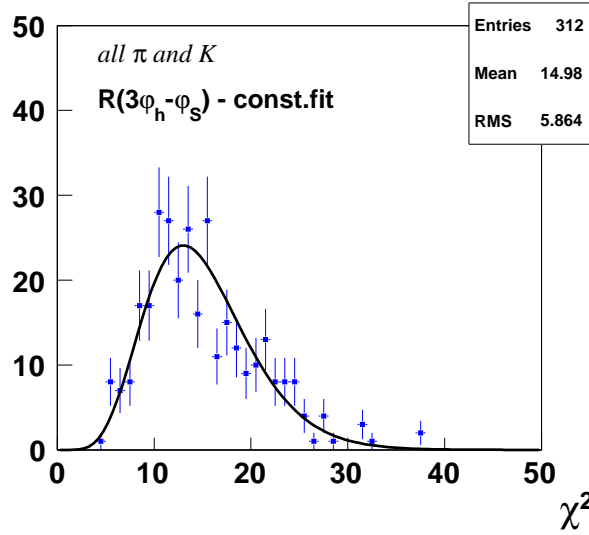
Figure 4.25: χ^2 distribution of the constant fit on $R(\Phi)$ values for $(3\phi_h - \phi_s)$ modulation compared to the normalized χ^2 distribution for $ndf = 15$ for all pions and kaons. Theoretical χ^2 distribution is normalized by the number of entries in the histogram.
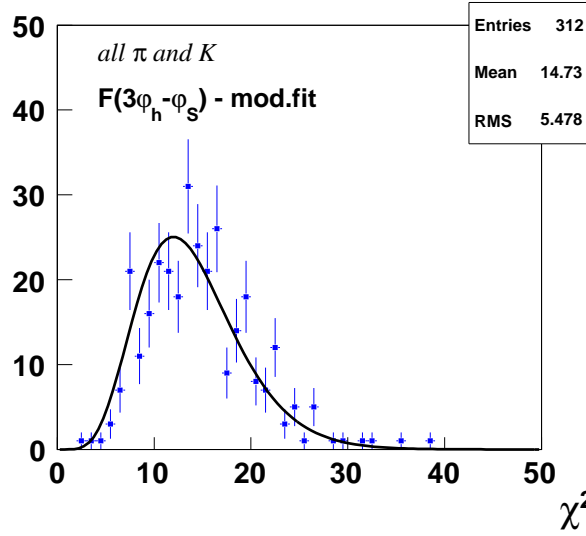
Figure 4.26: χ^2 distribution of the two parameter fit on $F(\Phi)$ values for $(3\phi_h - \phi_s)$ modulation compared to the normalized χ^2 distribution for $ndf = 14$ for all pions and kaons. Theoretical χ^2 distribution is normalized by the number of entries in the histogram.

and p_t kinematical bins. The number of entries is 1560. Combining the bins for x, z and p_t will give in total of 26 bins (9 bins in x + 8 bins in z + 9 bins in p_t). In total there are five modulations (26 x 5 = 130) calculated for two charged particles, pions and kaons (130 x 2 = 260), it is estimated for positive and negative particles (260 x 2 = 520), finally for three paired data periods P1G/H, W33/4, and W35/6 (520 x 3 = 1560). Fig. 4.27 reveals a Gaussian distribution for the parameter par(0) which has a narrow peak near 1 proving our assumption.

After performing these tests, there is no indication for any systematic effects. The conclusion is that the systematic errors due to acceptance and efficiency effects are considerably smaller than the statistical errors.
The asymmetry scale uncertainty due to the uncertainties on the target polarization P_T is of 5% and the error on the dilution factor f due to the uncertainty on the target composition is of the order 6%. Therefore, when combined in quadrature, the global scale uncertainty is of the order 8%.

4.12 Cross-check between two independent analyses

It is a general COMPASS collaboration policy that any result with COMPASS data for the publication has to be cross-checked between two independent analyses. In parallel to the analysis contained in this thesis, independent analysis of COMPASS
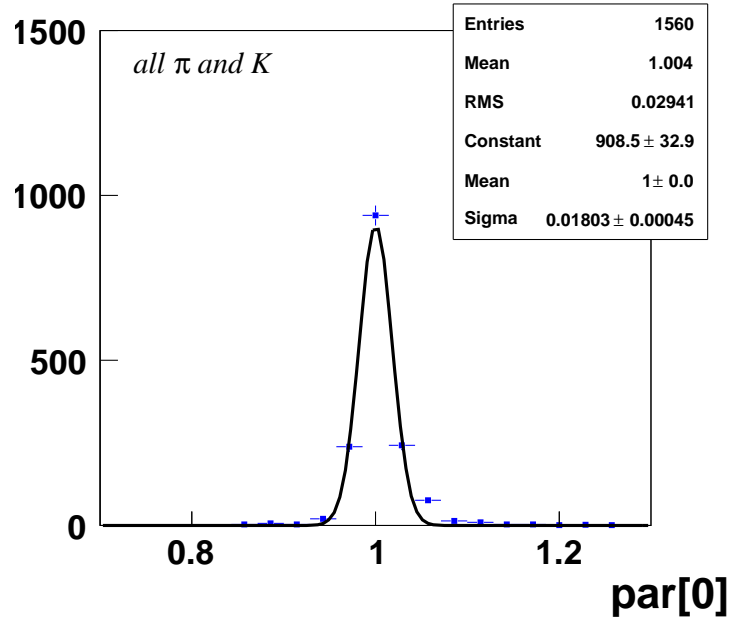
Figure 4.27: Gaussian distribution of the $par(0)$ values for all the five modulations of all the periods.

transverse data (2002 - 2004) was performed in University of Torino (Italy). Results of all the eight asymmetries extracted via the procedure explained in Section. 4.4 have been cross-checked using two independent analyses labeled as Bonn and Torino. As an example, Figs. 4.28 and 4.29 show the cross check between Bonn and Torino analysis for $A_{UT}^{\sin(3\phi_h - \phi_s)}$ asymmetry for pions and kaons for the weighted mean of 2003–2004 data. Just one asymmetry is taken as an example as all the other results shows an excellent agreement. Even though the two analysis agreed upon applying identical cuts, there are some differences, for example, the procedure of evaluating the asymmetries. Therefore slightly different values of the asymmetries are expected.

In order to have an insight about the difference between two independent results, a gaussian distribution is calculated with the formula

$$\frac{A_{To} - A_{Bn}}{\sigma_{To}}. \tag{4.60}$$

Here A_{To} is the asymmetry extracted by Torino group and A_{Bn} is the asymmetry extracted by Bonn group. The difference is then divided by the statistical error calculated by Torino (or Bonn). This value is calculated for each asymmetry for each bin in x, z and p_t and finally a Gauss fit is performed. This way the repetition of cross check plots can be avoided. Figs. 4.30 and 4.31 show the gaussian distributions for all the eight asymmetries for pions and kaons (combined). All gaussian yields RMS value approximately of 0.0004. This is a confirmation that the difference between two independent analyses in extracting the eight asymmetries is minimal.
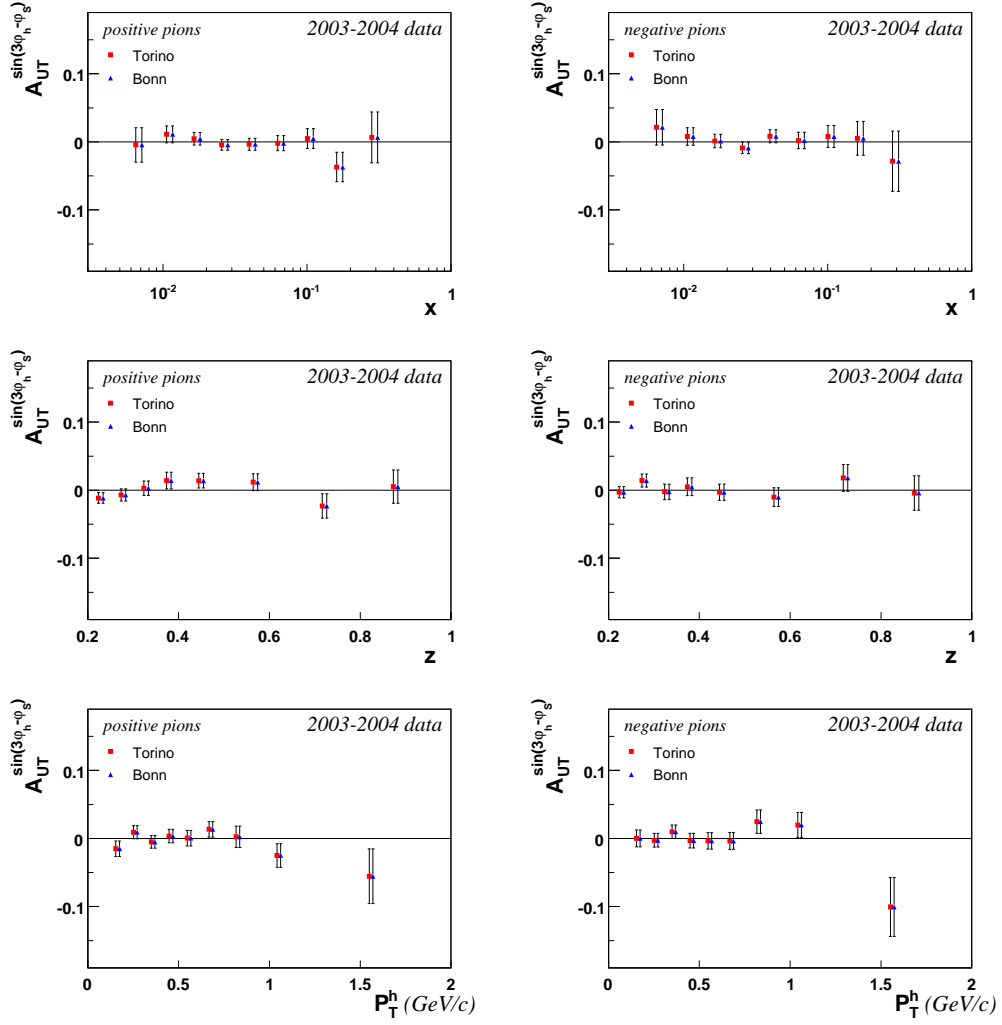
Figure 4.28: Cross check between Bonn and Torino analysis for $A_{UT}^{sin(3\phi_h - \phi_s)}$ asymmetry for all periods(2003 - 2004), all positive pions vs. x, z and p_t(left) and all negative pions vs. x, z and p_t(right).

Figure 4.29: Cross check between Bonn and Torino analysis for $A_{UT}^{sin(3\phi_h - \phi_s)}$ asymmetry for all periods(2003 - 2004), all positive kaons vs. x, z and p_t(left) and all negative kaons vs. x, z and p_t(right).

Figure 4.30: Cross check between Bonn and Torino analysis with one-dimensional fitting procedure: "pulls" distribution of the differences in the asymmetries by the statistical error for $A_{UT}^{-sin(\phi_h+\phi_s)}$(top left), $A_{UT}^{sin(\phi_h-\phi_s)}$(top right), $A_{UT}^{sin(3\phi_h-\phi_s)}$(bottom left), $A_{LT}^{cos(\phi_h-\phi_s)}$(bottom right).
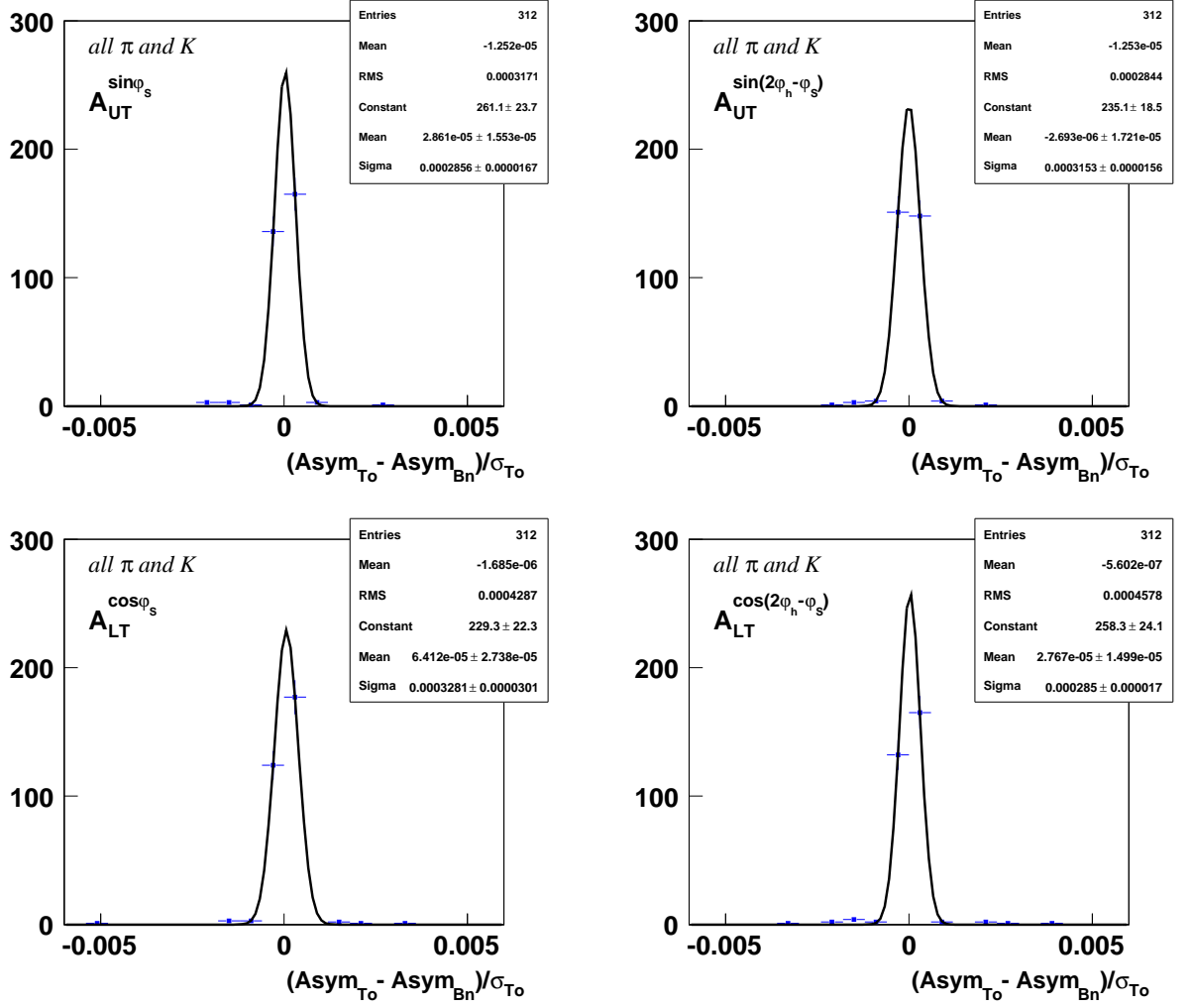
Figure 4.31: Cross check between Bonn and Torino analysis with one-dimensional fitting procedure: "pulls" distribution of the differences in the asymmetries by the statistical error for $A_{UT}^{sin(\phi_s)}$(top left), $A_{UT}^{sin(2\phi_h-\phi_s)}$(top right), $A_{LT}^{cos(\phi_s)}$(bottom left), $A_{LT}^{cos(2\phi_h-\phi_s)}$(bottom right).

4.13 Two-dimensional analysis

All eight TMD asymmetries were extracted with another procedure using two-dimensional method. Traditionally one-dimensional fitting procedure has been used to extract Collins and Sivers asymmetry. The extracted asymmetries were published in [84] and [77]. But in a recent COMPASS internal report [85] it has been understood that the extraction of SIDIS asymmetries using ratio product method with one-dimensional fitting procedure has an acceptance effect. Specifically the dependence on azimuthal angle ϕ_s was considered which eventually gives a distorted result. In SIDIS, we deal with six-dimensional phase space and look for dependence of some asymmetries on given variable(s), and integrate the counting rates over remaining ones. For example the number of counts for each target polarization is given by:

$$N^{\pm}_{u/d}(x, y, z, P^h_T, \phi_h, \phi_s) \propto A(\phi_h, \phi_s)\sigma^{\pm}_{u/d}(x, y, z, P^h_T, \phi_h, \phi_s). \quad (4.61)$$

Here, the acceptance function $A(\phi_h, \phi_s)$ now depends only on the azimuthal angles, but in Sec. 4.4, it has been shown that the SIDIS cross-section depends on five combinations of azimuthal angles (see Eqs. (4.15) - (4.19)).

$$\Phi_1 = \phi_h - \phi_s \quad (4.62)$$
$$\Phi_2 = \phi_h + \phi_s - \pi \quad (4.63)$$
$$\Phi_3 = 3\phi_h - \phi_s \quad (4.64)$$
$$\Phi_4 = \phi_s \quad (4.65)$$
$$\Phi_5 = 2\phi_h - \phi_s \quad (4.66)$$

Let us consider the ratio product method used in one-dimensional analysis (see Eq. (4.26)) now as a function of variable $v = x, y, z, P^h_T$:

$$A(v, \Phi_j) = \frac{N^+_u(v, \Phi_j)N^+_d(v, \Phi_j)}{N^-_u(v, \Phi_j)N^-_d(v, \Phi_j)}. \quad (4.67)$$

Here, $N^{\pm}_{u/d}(v, \Phi_j)$ is the counting rate dependence obtained by integrating over all phase space variables except v and Φ_j. To perform this integration the azimuthal variables have to be changed from $(\phi_h, \phi_s) \rightarrow (\phi_h, \Phi_j)$ and then be integrated over ϕ_h. To find the x-dependence, the integral looks like:

$$N^{\pm}_{u/d}(x, \Phi_j) \propto \int_{-\pi}^{\pi} d\phi_h \int dy dz dP^h_T A(\phi_h, \phi_{sj}(\phi_h, \Phi_j))\sigma^{\pm}_{u/d}(x, y, P^h_T, \phi_h, \phi_{sj}(\phi_h, \Phi_j)),$$
$$(4.68)$$

where j runs from 1 to 5. Now $\phi_{sj}(\phi_h, \Phi_j)$ can be written as:

$$\phi_{s1}(\phi_h, \Phi_1) = \phi_h - \Phi_1 \quad (4.69)$$
$$\phi_{s2}(\phi_h, \Phi_2) = \phi_h + \Phi_2 - \pi \quad (4.70)$$
$$\phi_{s3}(\phi_h, \Phi_3) = 3\phi_h + \Phi_3 \quad (4.71)$$
$$\phi_{s4}(\phi_h, \Phi_4) = \Phi_4 \quad (4.72)$$
$$\phi_{s5}(\phi_h, \Phi_5) = 2\phi_h - \Phi_5 \quad (4.73)$$

It should be noted that, the acceptance function is entering in Eq. (4.68) as an integrand which can only be factorized if the acceptance is uniform, since integral of product of two functions is not equal to product of integrals of these two functions. In general different terms in the cross-section have different dependencies on this unobserved variable and if acceptance is not uniformly dependent on this variable, then it will not be canceled in asymmetry, as it was explained in the context of the reasonable assumption (see Eq. (4.33)). This spurred the idea of using two-dimensional fitting procedure to extract asymmetries. Since we are not integrating over the azimuthal angle ϕ_h, the acceptance cancels out in each two-dimensional (ϕ_h, ϕ_s) bin.

Two-dimensional fitting procedures prove to be a powerful method to extract simultaneously all the eight asymmetries explained in section 4.5.2. In addition one can deduce the correlation coefficients between any two asymmetries. First a two-dimensional ϕ_h, ϕ_s histogram is filled for each bin in x_{Bj}, z and p_t. A typical two dimensional distribution of number of counts versus (ϕ_h, ϕ_s) for W35 data sample is shown in Fig. 4.32. It should be noted that the Fig. 4.32 shows a nonuniform
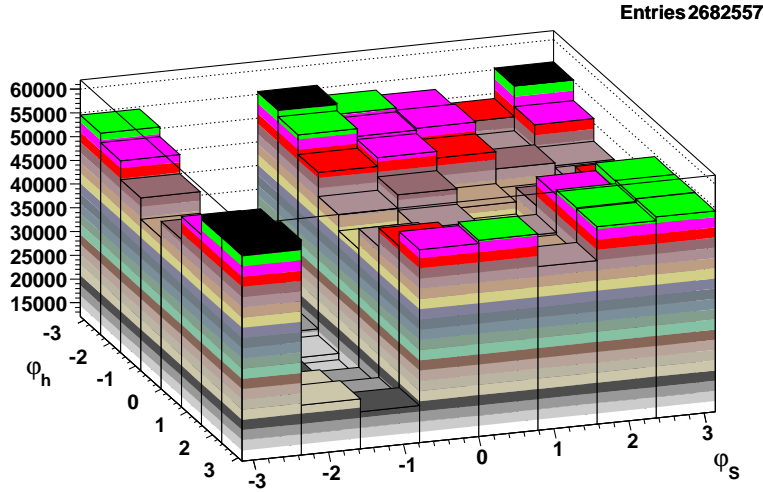
Figure 4.32: Two dimensional distribution of number of counts versus (ϕ_h, ϕ_s) for the target polarization (+) and $(\phi_h, \phi_s + \pi)$ for the target polarization (-) of the W35 data sample.

acceptance i.e. a deep valley in ϕ_s is visible due to a dip in the acceptance. For each subperiod of our measurement and each target cell, we can now describe the counting rate dependence, but this time with the two dimensional distribution of ϕ_h, ϕ_s. Similar to Eq. (4.25), the counting rate dependence $N_{u/d}^{\pm}(\phi_h, \phi_s)$ can be written as:

$$N_{u/d}^{\pm}(\phi_h, \phi_s) = F_{u/d}^{\pm} n_{u/d}^{\pm} a_{u/d}^{\pm}(\phi_h, \phi_s)\sigma\{1 \pm \sum_{i=1}^{8} A_{raw}^{w_i(\phi_h,\phi_s)} w_i(\phi_h, \phi_s)\}. \qquad (4.74)$$

Similar to the method described in the section 4.5.1, a double ratio can be constructed using Eq. (4.13).

$$A(\phi_h, \phi_s)_{ex} = \frac{N_u^+(\phi_h, \phi_s) N_d^+(\phi_h, \phi_s)}{N_u^-(\phi_h, \phi_s) N_d^-(\phi_h, \phi_s)}, \tag{4.75}$$

with the respective error propagation:

$$\sigma_{A(\phi_h, \phi_s)_{ex}} = \sqrt{\frac{1}{N_u^+(\phi_h, \phi_s)} + \frac{1}{N_d^+(\phi_h, \phi_s)} + \frac{1}{N_u^-(\phi_h, \phi_s)} + \frac{1}{N_d^-(\phi_h, \phi_s)}}. \tag{4.76}$$

Here, $A(\phi_h, \phi_s)_{ex}$ refers to the asymmetry extracted via the experimentally measured values, whereas $\sigma_{A(\phi_h, \phi_s)_{ex}}$ refers to the corresponding error calculated with the experimentally measured values. The ratio is then calculated in 8×8 equal bins over the range of (ϕ_h, ϕ_s). Using the similar assumption made in section 4.5.1, the ratio product equation for two-dimensional method can be expanded using Taylor expansion. At the first order, through these measured points a 9 parameter theoretical fit is performed. The fitting function looks like:

$$A(\phi_h, \phi_s)_{th} = par(0)[1 + 4[par(1)\sin(\phi_h + \phi_s - \pi) + par(2)\sin(3\phi_h - \phi_s) +$$
$$par(3)\sin(\phi_h - \phi_s) + par(4)\cos(\phi_h - \phi_s) + par(5)\sin(\phi_s) +$$
$$par(6)\sin(2\phi_h - \phi_s) + par(7)\cos(\phi_s) + par(8)\cos(2\phi_h - \phi_s)]]. \tag{4.77}$$

Here the parameters $par(1)$ to $par(8)$ give the "raw asymmetries" corresponding to the eight TMD moments, whereas $par(0)$ represents the constant term and is expected to be ≈ 1, which has been already proved in section 4.11.3.

To quantify the level of agreement between the experimentally measured values and a hypothesis, a *goodness − of − fit statistic* can be defined [86]. This can be done by calculating the χ^2 probability distribution function. In this case the χ^2 is calculated by the formula:

$$\chi^2 = \sum_{i=1}^{N} \left[\frac{\left(A(\phi_h, \phi_s)_{ex(i)} - A(\phi_h, \phi_s)_{th(i)}\right)^2}{\sigma_{A(\phi_h, \phi_s)_{ex(i)}}^2} \right] \tag{4.78}$$

Here i runs from 1 to N, where he measured ratio products are calculated in N $= n_h n_s$ bins of (ϕ_h, ϕ_s). For this nonlinear least square fit [87], the calculated χ^2 distribution is minimized, as the minimum value of the χ^2 represents the level of agreement between the measurements and the fitted function. The χ^2 minimization is done with the program MINUIT [88]. MINUIT is a tool to find the minimum value of a multi parameter function and analyze the shape of the function around the minimum, with the best fit parameter values and uncertainties, including correlation between the parameters. By minimizing the χ^2 distribution the MINUIT produces an 9 x 9 *error matrix* $M_{[i,j]}$ corresponding to the 9 parameters used in the fitting function. The errors based on the MINUIT error matrix take account of all the parameter correlations. After minimization, Minuit provides the raw asymmetry

results for the eight moments used in the fitting function. Those raw asymmetries can be corrected with the corresponding scaling factors, similarly as it was done for the raw asymmetries obtained with one-dimensional fitting procedure.

The ratio products are calculated in $N = n_h n_s$ bins of (ϕ_h, ϕ_s), initially with $n_h = 16$, $n_s = 16$ bins, to follow the same pattern as it was used in the one-dimensional procedure where the Φ_j is divided in 16 equal bins. However in the two-dimensional procedure, the MINUIT failed to minimize the calculated χ^2 distribution due to the presence of very low statistics in some bins. Therefore a re-binning is done with $n_h = 8$, $n_s = 8$. Even after re-binning, two-dimensional fit failed to converge results for periods with low statistics namely in COMPASS 2002 data periods. As a result, 2002 data periods namely (P2B/P2C) and P2H is excluded in the two-dimensional fitting procedure.

The two-dimensional fit proves to be a powerful and elegant method to extract any number of asymmetries, but the results obtained with two-dimensional fit are very close to those obtained with the one-dimensional fit, given the smallness of all obtained asymmetries. Therefore, the final results presented in this thesis are extracted using one-dimensional fitting procedure as it was used to extract Collins and Sivers asymmetry in our published papers [84] and [77].

4.13.1 Correlation coefficients

One of the advantages of using two-dimensional fit with multi parameters is that we have access to the covariances of the *error matrix* yielding the correlation coefficients. In our case we have 9 parameters and a 9×9 matrix with $M_{[i,j]}$ elements (i = 1 to 9) and (j = 1 to 9). In total we have 36 pairs for each x, z and p_t variable to look for correlation. The MINUIT program gives access to calculate the covariance and the variances. With that, one can calculate the correlation coefficient ρ as:

$$\rho_{[i,j]} = \frac{covariance_{[i,j]}}{\sqrt{variance_{[i,i]} \cdot variance_{[j,j]}}} \tag{4.79}$$

The correlation coefficient is calculated for 36 possible pairs. The observed correlation coefficients are mainly ≈ 0. Only for 8 combinations, the maximum value exceeds 0.1. Values of up to $|\rho| = 0.4$ are seen for some rare cases (single low statistics bins). Only the correlated pairs where the ρ value exceeds 0.1 is considered and plotted. As a sample, Fig. 4.33 shows the correlated pairs for the pions, whereas Fig. 4.34 shows it for the kaons.

- Red solid square indicates the correlation between $A_{UT}^{-\sin(\phi_h+\phi_s)}$ and $A_{UT}^{\sin(\phi_h-\phi_s)}$

- Green upper solid triangle indicates the correlation between $A_{UT}^{-\sin(\phi_h+\phi_s)}$ and $A_{UT}^{\sin(\phi_s)}$

- Blue lower solid triangle indicates the correlation between $A_{UT}^{\sin(3\phi_h-\phi_s)}$ and $A_{UT}^{\sin(2\phi_h-\phi_s)}$

- Yellow hollow circle indicates the correlation between $A_{UT}^{\sin(\phi_h-\phi_s)}$ and $A_{UT}^{\sin(\phi_s)}$

- Violet hollow square indicates the correlation between $A_{UT}^{\sin(\phi_h-\phi_s)}$ and $A_{UT}^{\sin(2\phi_h-\phi_s)}$

- Blue upper hollow triangle indicates the correlation between $A_{UT}^{\cos(\phi_h-\phi_s)}$ and $A_{UT}^{\cos(\phi_s)}$

- Green hollow diamond indicates the correlation between $A_{UT}^{\cos(\phi_h-\phi_s)}$ and $A_{UT}^{\cos(2\phi_h-\phi_s)}$
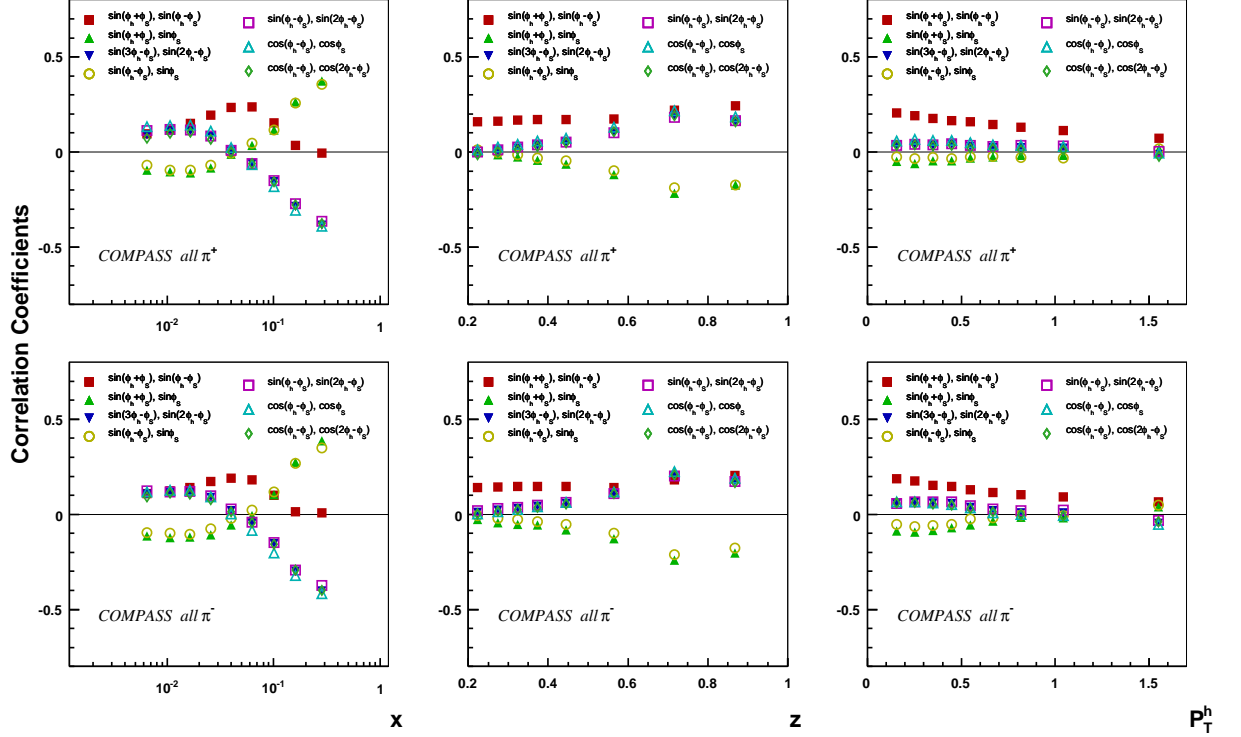
Figure 4.33: Correlation coefficients observed for pions, where the correlation is in the range above $\pm$ 0.1 in any one of the x, z and p_t bin.

To summarize the observed correlation coefficients are very small ($<$ 0.1). Only for 8 combinations, the maximum value exceeds 0.1 with the maximum value of up to $|\rho| = 0.4$ in some bins. The covariance i.e. the correlation in the error matrix are automatically taken into account in the calculation of the errors when the asymmetries are extracted via two-dimensional procedure. They are not accounted with the one-dimensional fitting procedure. The rather small correlation coefficients are due to the inhomogeneous detector acceptance (see Fig. 4.32).

Figure 4.34: Correlation coefficients observed for kaons, where the correlation is in the range above $\pm$ 0.1 in any one of the x, z and p_t bin.

4.14 Comparison of asymmetries with the two procedures

As we have extracted all the 8 asymmetries via a one-dimensional fitting procedure and two-dimensional fitting procedure, it becomes necessary to compare these results. Below are the comparison between the results from two different fitting procedures from 2003 - 2004 data. Fig. 4.35 shows the cross check between 1D and 2D results for Sivers asymmetry for the positive pions(left) and the negative pions (right) plotted against x, z and p_t. Fig. 4.36 shows the same for kaons. A very small difference can be observed. The difference could be due to the fact that the one-dimensional fitting procedure suffers an acceptance effect with a non uniform detector acceptance, as explained before.
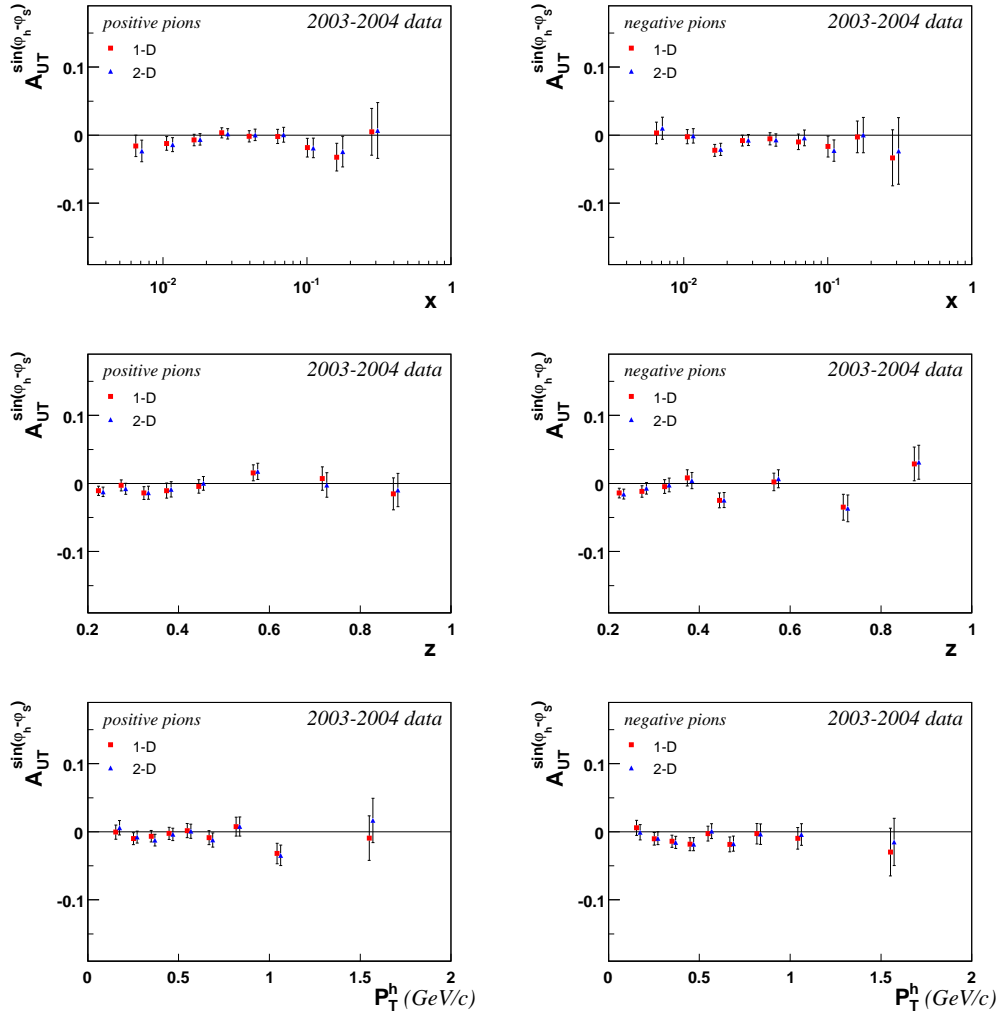
Figure 4.35: Cross check between 1D and 2D analysis for $A_{UT}^{\sin(\phi_h - \phi_s)}$ asymmetry for the periods in 2003 - 2004, all positive pions vs. x, z and p_t(left) and all negative pions vs. x, z and p_t(right).
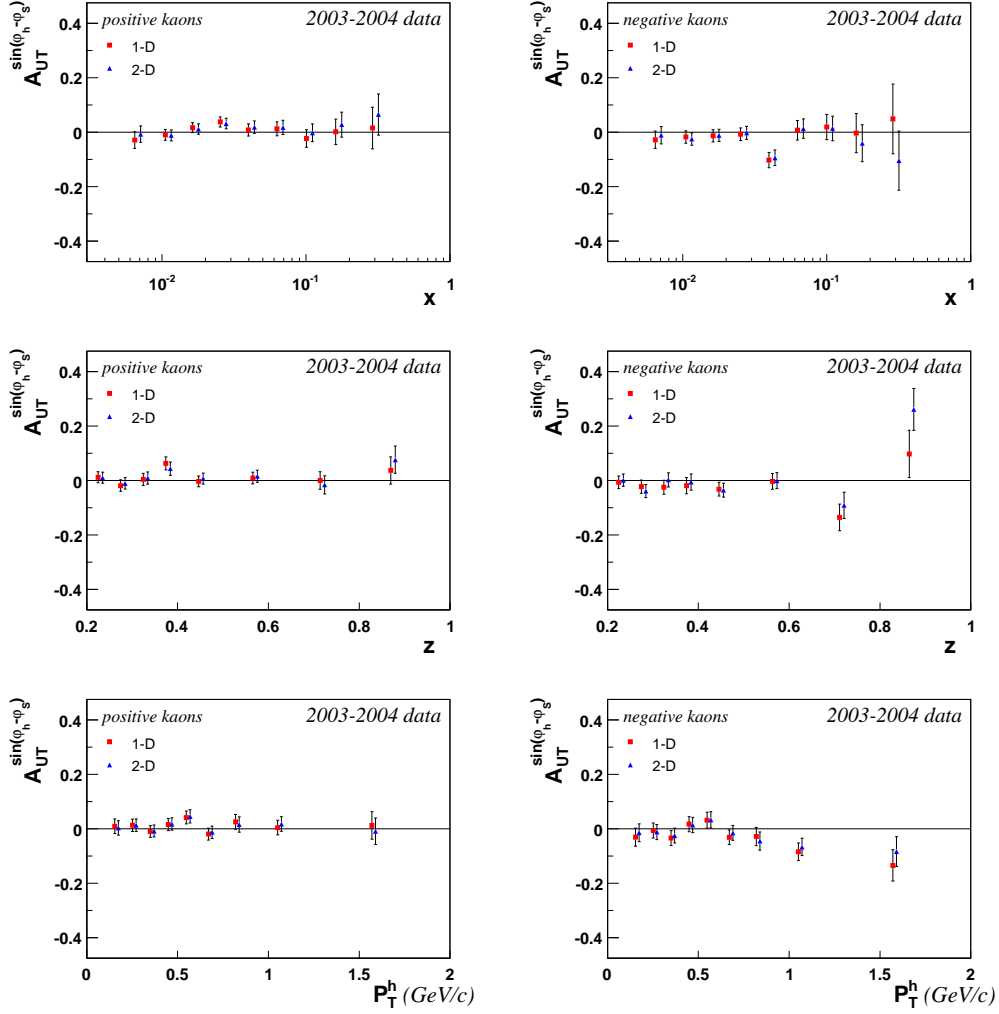
Figure 4.36: Cross check between 1D and 2D analysis for $A_{UT}^{\sin(\phi_h - \phi_s)}$ asymmetry for the periods in 2003 - 2004, all positive kaons vs. x, z and p_t(left) and all negative kaons vs. x, z and p_t(right).

Chapter 5

Results and interpretation

"When I have fully decided that a result is worth getting, I go ahead of it and make trial after trial until it comes."

Thomas Alva Edison

In this chapter the results of the eight Transverse Momentum Dependent (TMD) asymmetries will be presented. Results for each asymmetry is given for unidentified hadrons (positive and negative) with COMPASS 2002-2004 data followed up by identified pions (positive and negative) and kaons (positive and negative) with COMPASS 2003-2004 data sample. Asymmetries are plotted as a function of x, z and P_T^h. Results for Collins asymmetry are presented first including comparison with the theoretical models. Results for Sivers asymmetry are presented next including comparison with the theoretical models. Global fits by various theory groups with COMPASS, HERMES (see section 5.5.1) and BELLE (see section 5.5.2) data were performed to extract transversity, Collins function and Sivers function. These fits were only possible with the proton data from HERMES and the corresponding deuteron data from COMPASS. A short description of other transversity measurements performed at COMPASS will also be discussed. The chapter ends with the discussion on other existing experiments around the globe performing transversity measurements along with the future plans of various other experiments which plan to extract transversity, Collins distribution function and Sivers function.

5.1 Collins asymmetry $\left(A_{UT}^{\sin(\phi_h+\phi_s-\pi)}\right)$

The measured values for Collins asymmetry with 2002-2004 COMPASS data against three variables x, z, P_T^h are given in Fig. 5.1. The error bars shown in all the plots

are statistical only whereas the systematic error is considerably smaller than the statistical one. The red circles show the results for positive hadrons, pions and kaons whereas blue triangles show the results for negative hadrons, pions and kaons. In all the plots the blue triangles are slightly shifted horizontally with the respect to the measured value. Measured Collins asymmetry for pions, kaons and unidentified hadrons are very small or compatible with zero.
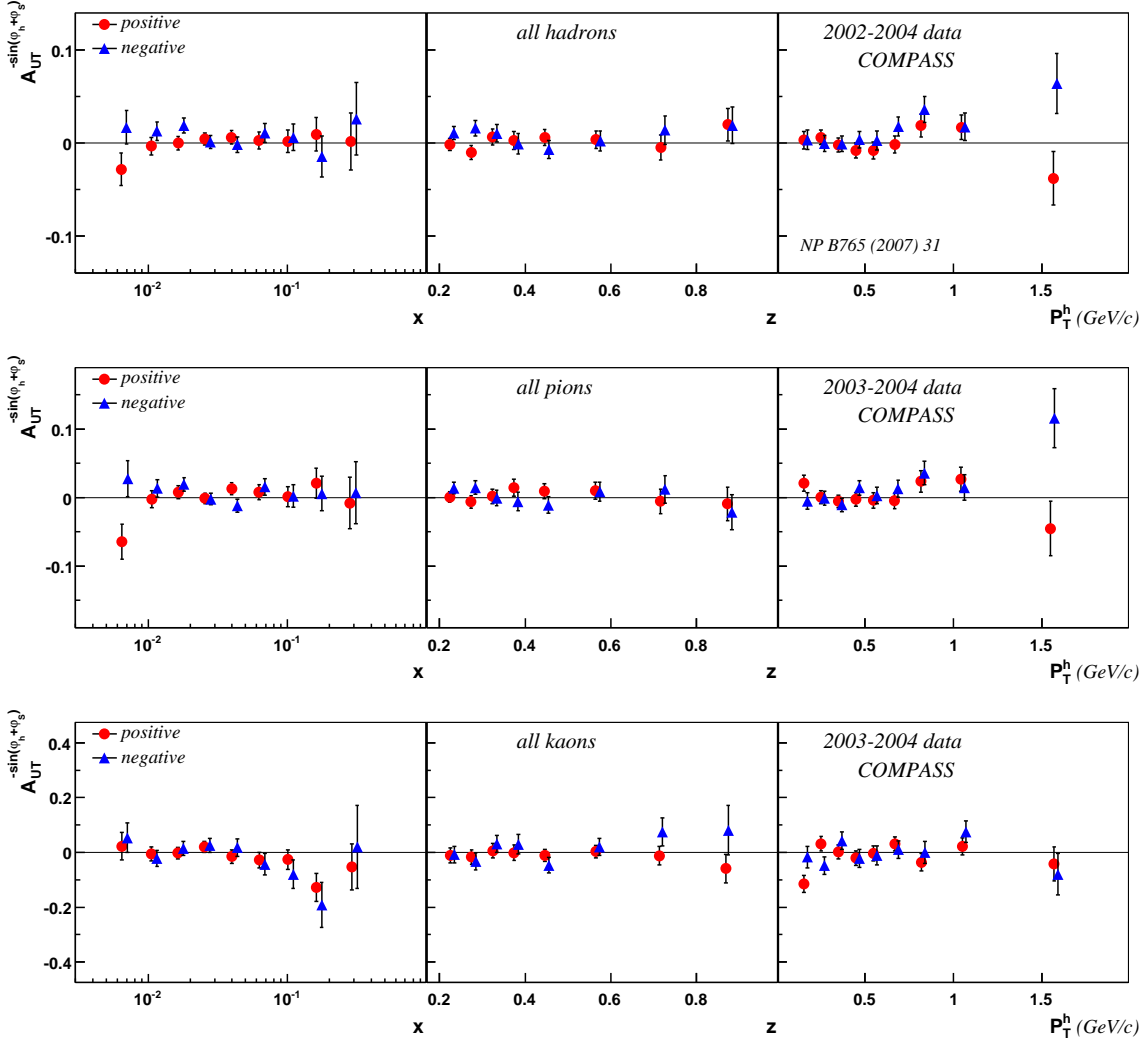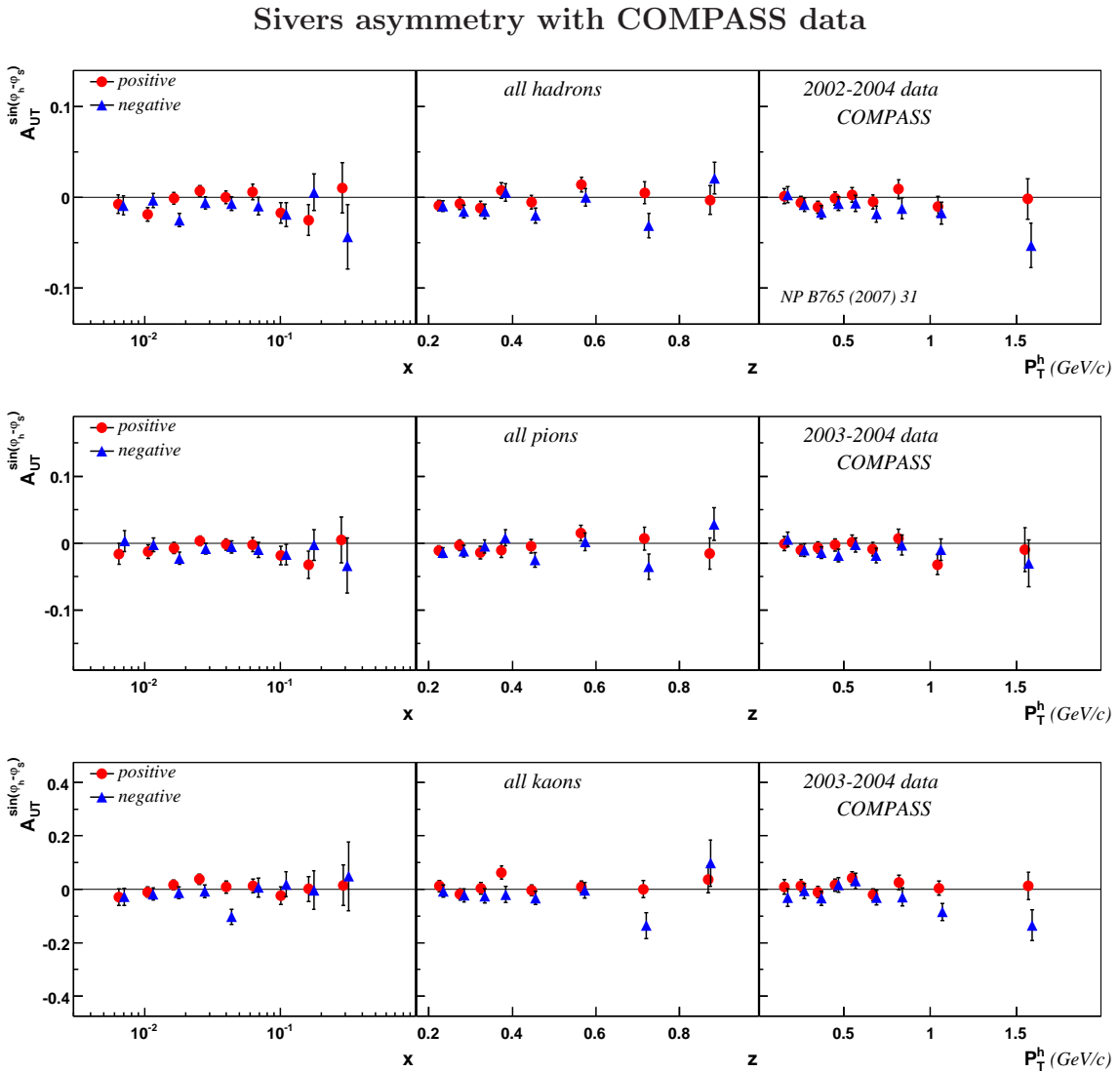

Figure 5.1: Extracted Collins asymmetry for unidentified hadrons (top row), pions (middle row) and kaons (bottom row) as a function of x, z and P_T^h.

5.1.1   Comparison with models

Observing small asymmetries is not a surprise because from the beginning it was predicted that transverse spin effects would be small in the deuteron due to the

opposite sign which was expected for the u and d distributions, causing cancelations of the asymmetries of an iso-scalar target. Any attempt to analyze the results on the deuteron can be done only in conjunction with corresponding proton data. The HERMES collaboration [89] measured non zero Collins asymmetry on proton. The data provide convincing evidence that both the transversity and the Collins mechanism are nonzero. Recent results of the BELLE collaboration provides evidence for a non zero Collins fragmentation function. A global analysis (described later in this section) using data available for deuteron and proton should shed light on the estimation of the contribution from u and d quarks.

First, a naive interpretation of the measured Collins asymmetry on deuteron for unidentified hadrons can be performed. For this interpretation, considering the pion sample, many assumptions are made such as, neglecting the sea quark contribution (i.e. $\Delta_T \bar{q} = \Delta_T s = 0$ and $\bar{q} = s = 0$) and considering only the x range between $0.1 < x < 0.3$ (valence region). Now lets take the equation for Collins asymmetry [77],

$$A_{Coll} = \frac{\sum_q e_q^2 \cdot \Delta_T q(x) \cdot \Delta_T^0 D_q^h(z, p_T^h)}{\sum_q e_q^2 \cdot q(x) \cdot D_q^h(z, p_T^h)} \,. \tag{5.1}$$

Taking the two sets of fragmentation functions:

$$D_{\pi^+/u} = D_{\pi^+/\bar{d}} = D_{\pi^-/\bar{u}} = D_{\pi^-/d} \qquad favoured, \tag{5.2}$$

$$D_{\pi^+/\bar{u}} = D_{\pi^+/d} = D_{\pi^-/u} = D_{\pi^-/\bar{d}} \qquad unfavoured \tag{5.3}$$

and lets assume,

$$D_u^{\pi^+} = D_d^{\pi^-} = D_1 \,, \; D_d^{\pi^+} = D_u^{\pi^-} = D_2 \,, \tag{5.4}$$

$$\Delta_T^0 D_u^{\pi^+} = \Delta_T^0 D_d^{\pi^-} = \Delta_T^0 D_1 \,, \; \Delta_T^0 D_d^{\pi^+} = \Delta_T^0 D_u^{\pi^-} = \Delta_T^0 D_2 \,. \tag{5.5}$$

Now substituting the relevant assumptions to Eq. (5.1), one gets Collins asymmetry for π^+ on a proton target as :

$$A_{Coll}^{p,\pi^+} \simeq \frac{4\Delta_T u_v \Delta_T^0 D_1 + \Delta_T d_v \Delta_T^0 D_2}{4u_v D_1 + d_v D_2}, \tag{5.6}$$

and for π^- as :

$$A_{Coll}^{p,\pi^-} \simeq \frac{4\Delta_T u_v \Delta_T^0 D_2 + \Delta_T d_v \Delta_T^0 D_1}{4u_v D_2 + d_v D_1} \,. \tag{5.7}$$

Taking the suggestion from the HERMES data i.e $\Delta_T^0 D_1 = -\Delta_T^0 D_2$, and taking the information from the unpolarized data, $D_2 \simeq 0.5 D_1$, $d_v \simeq 0.5 u_v$, the previous expressions become

$$A_{Coll}^{p,\pi^+} \simeq \frac{\Delta_T u_v}{u_v} \frac{\Delta_T^0 D_1}{D_1}, \tag{5.8}$$

and

$$A_{Coll}^{p,\pi^-} \simeq -\frac{4}{2.5} \frac{\Delta_T u_v}{u_v} \frac{\Delta_T^0 D_1}{D_1}, \tag{5.9}$$

respectively. It clearly shows the contribution from the u-quark is dominant.
We can play the same game for a deuteron target. With the isospin considerations
i.e. $u_v^p = d_v^n$ and vice versa, the Eqs. (5.6), (5.7), (5.8), and (5.9) become

$$A_{Coll}^{d,\pi^+} \simeq \frac{\Delta_T u_v + \Delta_T d_v}{u_v + d_v} \frac{4\Delta_T^0 D_1 + \Delta_T^0 D_2}{4D_1 + D_2} \tag{5.10}$$

$$A_{Coll}^{d,\pi^-} \simeq \frac{\Delta_T u_v + \Delta_T d_v}{u_v + d_v} \frac{\Delta_T^0 D_1 + 4\Delta_T^0 D_2}{D_1 + 4D_2} \tag{5.11}$$

and

$$A_{Coll}^{d,\pi^+} \simeq \frac{3}{7} \frac{\Delta_T u_v + \Delta_T d_v}{u_v} \frac{\Delta_T^0 D_1}{D_1} \tag{5.12}$$

$$A_{Coll}^{d,\pi^-} \simeq -\frac{3}{4.5} \frac{\Delta_T u_v + \Delta_T d_v}{u_v} \frac{\Delta_T^0 D_1}{D_1}. \tag{5.13}$$

respectively. Both the π^+ and the π^- Collins asymmetries on the deuteron are
proportional to $\Delta_T u_v(x) + \Delta_T d_v(x)$. Therefore cancelations are expected to reduce
considerably the effect which has been measured on the proton. As a matter of fact,
assuming $\Delta_T d_v = 0$ (no limit on the size of $\Delta_T d_v$ is provided by the HERMES data)
one derives relations between the Collins asymmetry measured by HERMES and
COMPASS which are only marginally satisfied. Thus, the present precise data on
$A_{Coll}^{d,\pi}$ should allow to extract $\Delta_T d_v$.

Three different global analyses have been performed till now with the
published data from COMPASS, HERMES and BELLE experiments. In ref [90],
the single spin asymmetry (SSA) in the SIDIS process $ep \to ehX$ (measured in
HERMES) and $\mu d \to \mu hX$ (measured at COMPASS) were studied. By using some
simple parameterizations for the Collins fragmentation function, a fit of the HER-
MES data were performed. The Soffer bound $|\Delta_T q| = (q + \Delta q)/2$ was considered
to extract Collins functions. Different scenarios for favored and unfavored Collins
fragmentation functions were considered but the fits always favored the relation
$\Delta_T^0 D_1 \sim -\Delta_T^0 D_2$. The fit results were used to make phenomenological prediction
for the published COMPASS data [84] shown in Fig. 5.2. It should be noted that,
the authors have used the leading hadron sample in the published COMPASS data.
The figure shows a fair agreement of the theoretical interpretations.

In ref [91], the Collins fragmentation function is extracted with SIDIS
data obtained from HERMES experiment, COMPASS experiment and azimuthal
asymmetries in e^+e^- annihilation data obtained from BELLE experiment. A gaus-
sian model is assumed for the distribution of transverse parton momenta and a chiral
quark-soliton model was used for the transversity distribution function. First the
Collins effect is studied with the available SIDIS data and checked for its compatibil-
ity with e^+e^- annihilation data from BELLE experiment, and it was observed that
they are in good agreement. A fit is made with HERMES data and the fit results
were used to predict published COMPASS data [84]. It should be noted that, the
authors have used the leading hadron sample in the published COMPASS data. Fig.
5.3 shows the description of the COMPASS data.
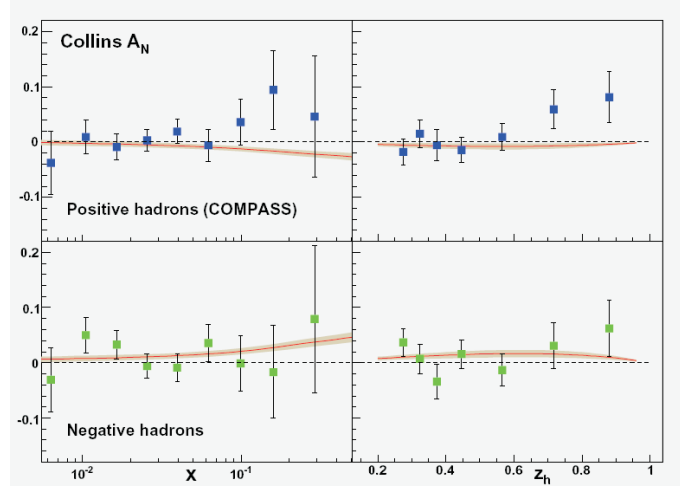
Figure 5.2: Collins asymmetry compared with COMPASS data [84] for the fitted Collins functions in reference [90]
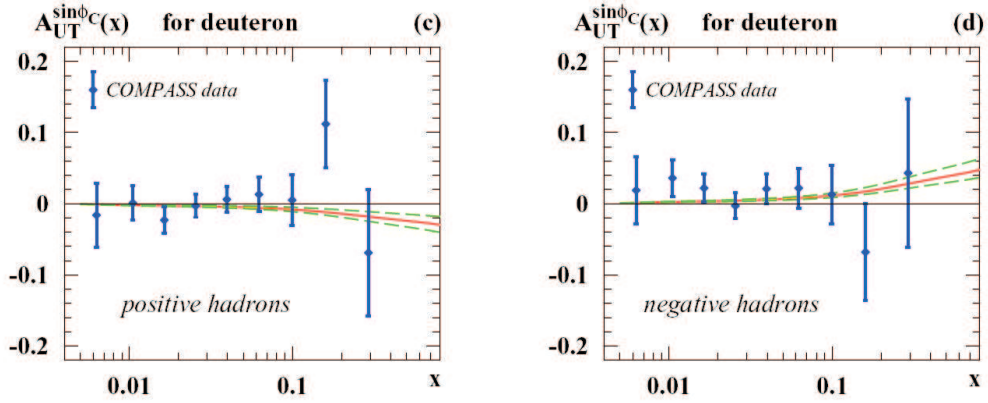
Figure 5.3: Collins asymmetry compared with COMPASS data [84] for the fitted Collins functions in reference [91]

In ref [92], a global fit is performed with results obtained from COMPASS, HERMES and BELLE experiments. This analysis is fairly new and it results in the extraction of the Collins fragmentation of the transversity distribution function for u and d quarks for the first time. First Transversity and Collins functions were extracted with the available SIDIS data then the Collins fragmentation function was extracted with the available e^+e^- annihilation data. With the fit results, predictions for the forthcoming experiments were given. With the global fit results description of the published data from COMPASS, HERMES and BELLE were presented. Fig. 5.4 shows the description of the published COMPASS data using the global fit results. Fig. 5.5 shows the Transversity distribution functions for u and d quarks determined through the global fit.
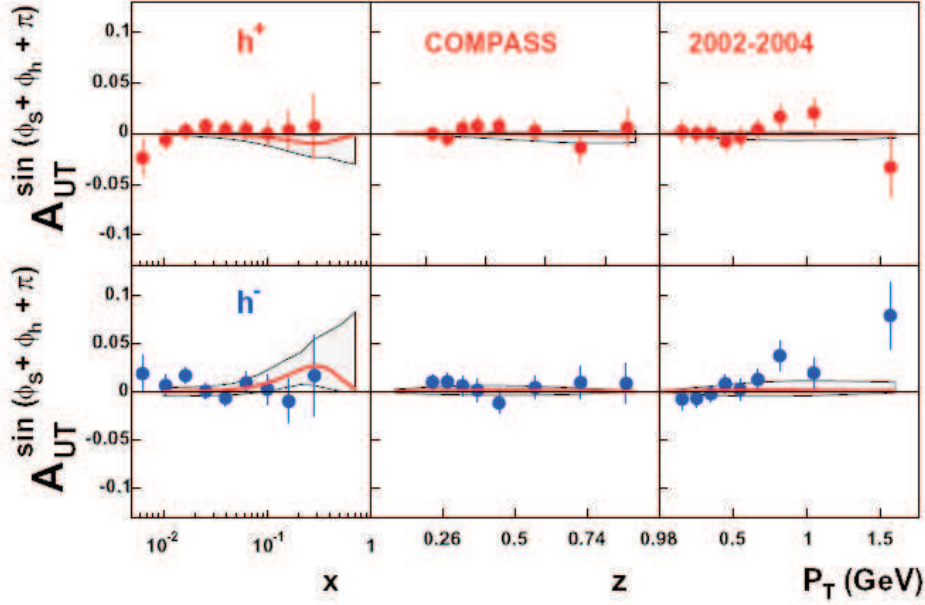
Figure 5.4: Collins asymmetry compared with COMPASS data [77] for the fitted Collins functions in reference [92]
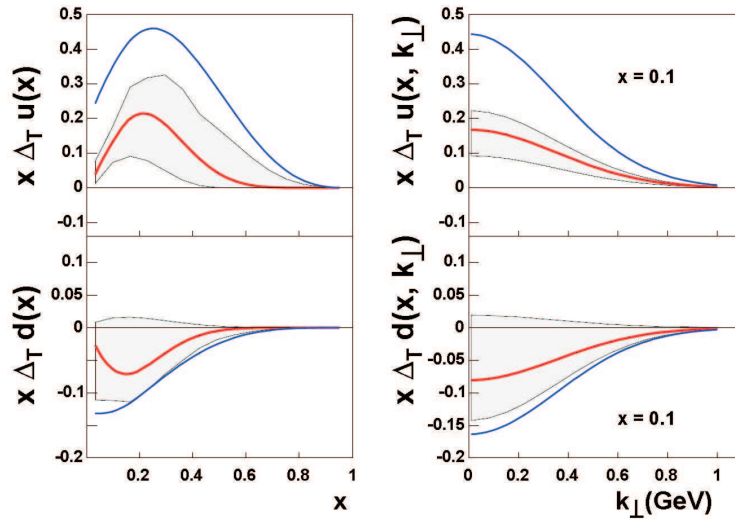
Figure 5.5: The transversity distribution functions for u and d determined with the global fit performed in [92]. The left panel shows $x\Delta_T u(x)$ (upper plot) and $x\Delta_T d(x)$ (lower plot). In the right panel, the unintegrated transversity distributions, $x\Delta_T u(x, k_\perp)$ (upper plot) and $x\Delta_T d(x, k_\perp)$ (lower plot) are shown. The bold blue line as an upper and lower limit shows the Soffer bound whereas the shaded area shows its fit uncertainty.

5.2 Sivers asymmetry ($A_{UT}^{\sin(\phi_h - \phi_s)}$)

Measured values for Sivers asymmetry with 2002-2004 COMPASS data against three variables x, z, P_T^h are given in Fig. 5.6. The error bars shown in all the plots are statistical only whereas the systematic error is considerably smaller than the statistical one. The red circles show the results for positive hadrons, pions and koans whereas blue triangles show the results for negative hadrons, pions and kaons. In all the plots the blue triangles are slightly shifted horizontally with the respect to the measured value. Measured Sivers asymmetry for pions, kaons and unidentified hadrons are very small or compatible with zero.

Figure 5.6: Extracted Sivers asymmetry for unidentified hadrons (top row), pions (middle row) and kaons (bottom row) as a function of x, z and P_T^h

5.2.1 Comparison with models

Similar to the Collins asymmetry, the measured Sivers asymmetry for pions, kaons and hadrons are very small or compatible to zero. Similar hypothesis can be implemented here for Sivers asymmetry as it was performed for Collins asymmetry. Lets take the equation for Sivers asymmetry [77],

$$A_{Siv} = \frac{\sum_q e_q^2 \cdot \Delta_0^T q(x, p_T^h/z) \cdot D_q^h(z)}{\sum_q e_q^2 \cdot q(x, p_T^h/z) \cdot D_q^h(z)} \tag{5.14}$$

Considering the pion sample and restricting the analysis to the valence region by neglecting the sea contribution (i.e. $\Delta_0^T \bar{q} = \Delta_0^T s = 0$ and $\bar{q} = s = 0$ at all x) and assuming $D_u^{\pi^+} = D_d^{\pi^-} = D_1$ and $D_d^{\pi^+} = D_u^{\pi^-} = D_2$, on a proton target the equation for Sivers asymmetry can be written for π^+ and π^-.
For π^+:

$$A_{Siv}^{p,\pi^+} \simeq \frac{4\Delta_0^T u_v D_1 + \Delta_0^T d_v D_2}{4u_v D_1 + d_v D_2} \tag{5.15}$$

and for π^-:

$$A_{Siv}^{p,\pi^-} \simeq \frac{4\Delta_0^T u_v D_2 + \Delta_0^T d_v D_1}{4u_v D_2 + d_v D_1} . \tag{5.16}$$

Assuming $D_2 \simeq 0.5 D_1$, $d_v \simeq 0.5 u_v$, the previous two expressions can be simplified and written as

$$A_{Siv}^{p,\pi^+} \simeq \frac{\Delta_0^T u_v}{u_v} \tag{5.17}$$

and

$$A_{Siv}^{p,\pi^-} \simeq \frac{2\Delta_0^T u_v + \Delta_0^T d_v}{2.5 u_v} \tag{5.18}$$

respectively.
Sivers asymmetry for π^- measured by HERMES on a proton target is about zero, this simplifies the treatment and we get,

$$\Delta_0^T d_v = -2\Delta_0^T u_v . \tag{5.19}$$

Now we can go on and perform the similar treatment for a deuteron target. We can get the expressions for Sivers asymmetry in the case of π^+ and π^-,

$$A_{Siv}^{d,\pi^+} \simeq \frac{\Delta_0^T u_v + \Delta_0^T d_v}{u_v + d_v} \tag{5.20}$$

and

$$A_{Siv}^{d,\pi^-} \simeq \frac{\Delta_0^T u_v + \Delta_0^T d_v}{u_v + d_v} \tag{5.21}$$

The two expressions (5.20) and (5.21) simply imply that $A_{Siv}^{d,\pi^+} \simeq A_{Siv}^{d,\pi^-}$. This clearly shows that the Sivers asymmetry for positive and negative hadrons observed in COMPASS experiment requires,

$$\Delta_0^T d_v \simeq -\Delta_0^T u_v. \tag{5.22}$$

In ref [90], the authors have performed a simple fit for the Sivers functions for u and d quarks using the HERMES data. The fit of the HERMES data is very good and gave as a result $\Delta_0^T d_v \simeq -\Delta_0^T u_v$. Using the fit results the Sivers asymmetries were calculated for π^+ and π^- in the kinematic region of the COMPASS experiment. These results are then compared to the COMPASS results for leading positive and negative hadrons [84]. Fig. 5.7 shows the comparison with the Sivers data obtained from the COMPASS experiment. Predicted Sivers asymmetries for a deuteron target are very small, except in the large-x region. The smallness of the Sivers asymmetry is related to cancelations between u and d contributions, which for deuterons enter in a different combination than for a proton target.
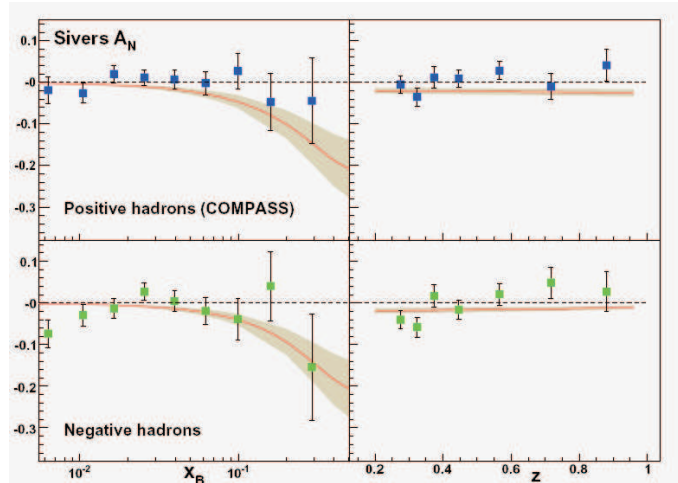
Figure 5.7: Sivers asymmetry compared with the COMPASS data [84] for the fitted Sivers functions in the reference [90]

In ref [93], SIDIS data from HERMES and COMPASS were analyzed within leading order (LO) parton model with un-integrated parton distribution and fragmentation functions. For the first time constrained extraction of the Sivers function for u and d quarks was performed. Fig. 5.8 shows the description of the COMPASS data from the results of the fit. Assuming a Gaussian factorization of the $k_\perp$ and $p_\perp$ dependence of all distribution and fragmentation functions, together with a most simple parametrization of the x-dependence of the unknown Sivers functions, for the first time the information on $\Delta^N f_{u/p^\uparrow}(x, k_\perp)$ and $\Delta^N f_{d/p^\uparrow}(x, k_\perp)$ were extracted. Fig. 5.9 shows the x dependence of the extracted Sivers function.

In an another approach in ref [94], the authors have performed a detail empirical studies to estimate the gluon and quark orbital angular momentum con-
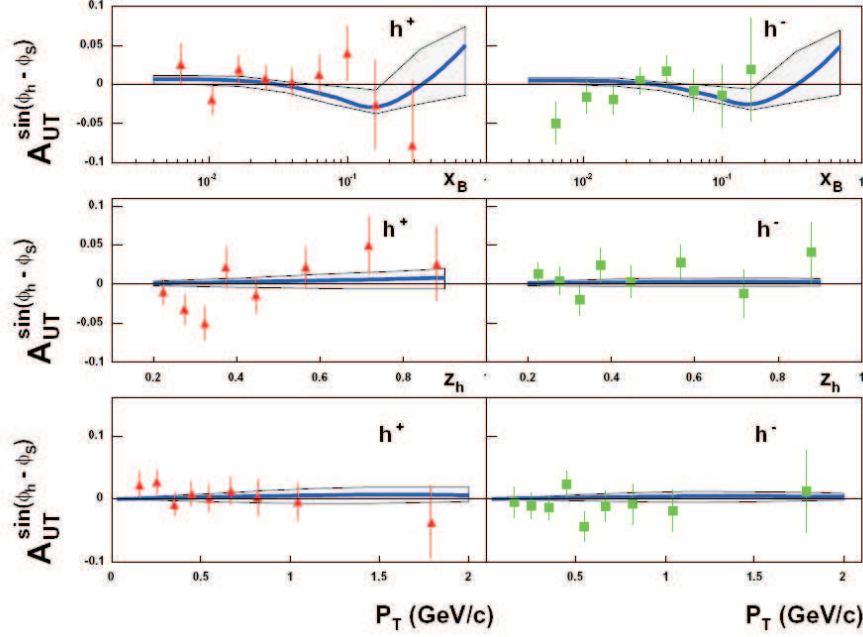
Figure 5.8: Sivers asymmetry compared with the COMPASS data [84] for the fitted Sivers functions in the reference [93]

tributions to the Sivers asymmetry. In their studies with the deuteron data, it was found that the SSA for u-quark fragmentation to leading positively charged hadrons, as well as d-quark fragmentation to leading negatively charged hadrons, ought to be small. Therefore the authors claim that, the observed small Sivers asymmetry for positive and negative hadrons on the deuterons has been interpreted as the evidence for the absence of gluon orbital angular momentum in the nucleon.

5.3 Results for other asymmetries

Measured values for other TMD asymmetries such as $A_{LT}^{\cos(\phi_h-\phi_s)}$ asymmetry, $A_{UT}^{\sin(3\phi_h-\phi_s)}$ asymmetry, $A_{UT}^{\sin(\phi_s)}$ asymmetry, $A_{UT}^{\sin(2\phi_h-\phi_s)}$ asymmetry, $A_{UT}^{\cos(\phi_s)}$ asymmetry and $A_{LT}^{\cos(2\phi_h-\phi_s)}$ asymmetry for pions, kaons and unidentified hadrons are very small or compatible with zero. These six asymmetries are only extracted from COMPASS data up to now. Even a naive interpretation cannot be preformed for these asymmetries without the corresponding results from proton data. Therefore the final results for these asymmetries, see Figs. 4.15 to 4.20.
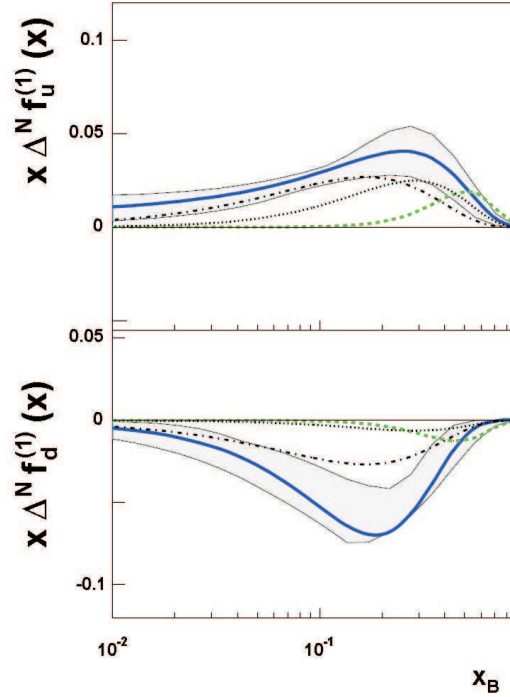
Figure 5.9: The x dependence of the Sivers function extracted with fit performed in [93]. The shaded area corresponds the to fit uncertainity.

5.4 Other transversity measurements at COMPASS

So far we have seen the results for Transverse Momentum Dependent (TMD) asymmetries with special attention to Collins asymmetry and Sivers asymmetry. There are two other measurements which have been performed with COMPASS experiment namely the measurement of "two hadron production" introducing the chiral odd interference fragmentation function $H_1^\sphericalangle$ (very much similar to the Collins fragmentation function) to probe the transverse distribution function $\Delta_T q(x)$ and the "Λ polarimetry" to get information on the transversity distribution function by measuring the polarization of the current jet Λ produced in SIDIS.

5.4.1 Two hadron asymmetry

An alternative method has been proposed (see [95] and references therein) to measure the "relative Collins effect" between two fast particles on the jet, which allows us to measure an asymmetry which is practically not affected by fluctuations in the fragmenting quark momentum. An asymmetry is expected due to the interference between the helicity-flip amplitude and the helicity conserving one namely the "in-

terference fragmentation function" [96]. This asymmetry is measured very much like the Collins asymmetry, essentially replacing the azimuthal angle of the hadron ϕ_h with the azimuthal angle of the plane containing two hadrons φ_R (see Fig. 5.10).
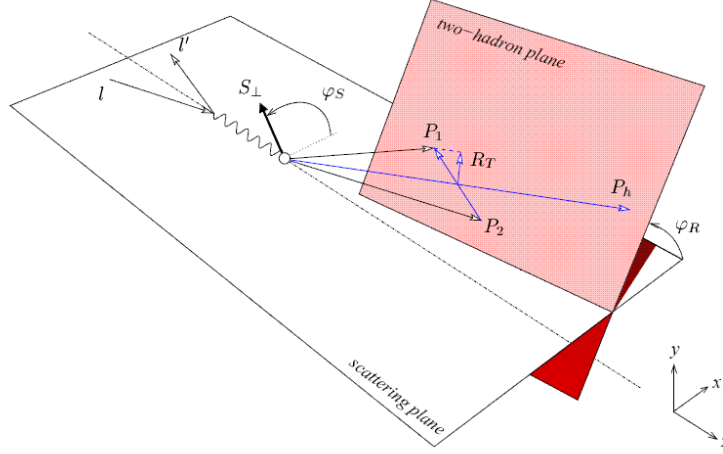
Figure 5.10: Description of the angles involved in the measurement of single spin asymmetries in deep-inelastic production of two hadrons [96].

In COMPASS experiment, φ_R is defined as the azimuthal angle of R_T with respect to the lepton scattering plane. From the angular distribution in $\varphi_{RS} = \varphi_R - \varphi_s$, it is possible to measure the asymmetry $A_{UT}^{\sin \varphi_{RS}}$ by:

$$\frac{A_{UT,raw}^{\sin \varphi_{RS}}}{f \cdot P_T \cdot D_{NN}} = \frac{\sum_i e_i \cdot \Delta_T q_i(x) \cdot H_1^{\triangleleft h}(z, M_h^2)}{\sum_i e_i \cdot q_i(x) \cdot D_i^h(z, M_h^2)}. \tag{5.23}$$

.

Here both the spin dependent fragmentation function $H_1^{\triangleleft h}(z, M_h^2)$ and the corresponding spin averaged FF $D_i^h(z, M_h^2)$, are unknown and need to be measured in e^+e^- annihilation or to be evaluated using models.

5.4.2 Λ polarimetry

Another transversity measurement carried out in COMPASS experiment is the Λ polarimetry. Here the information on the transversity distribution function $\Delta_T q(x)$ can be obtained by measuring the polarization of the current jet Λ or $\overline{\Lambda}$ produced in SIDIS. This is one of the first methods proposed to access transversity. The transverse polarization of the Λ measured with respect to the nucleon spin axis $\overrightarrow{S_T}$ is related to the transversity distribution function by:

$$\frac{P_{\lambda,raw}^S}{f \cdot P_T \cdot D_{NN}} = \frac{\sum_q e_q^2 \cdot \Delta_{Tq} \cdot \Delta_T D_q^\lambda}{\sum_q e_q^2 \cdot q \cdot D_q^\Lambda}. \tag{5.24}$$

Here $\Delta_T D_q^\lambda$ is the fragmentation function of the transversely polarized quark q into a Λ and it needs to be measured independently. The only disadvantage of this measurement is that the statistical efficiency as a quark polarimetry is poor due to the relatively small abundance of weak decaying hyperons in quark jets.

5.5 Measurements in other experiments

There are several experiments measuring transversity, Collins function and Sivers function. To unravel several unknown distribution and fragmentation functions, SIDIS measurements cannot be mapped alone. In addition, data from e^+e^- annihilation, polarized hadron-production of mesons and polarized Drell-Yan can be used to make a global analysis in order to extract the unknown functions.

5.5.1 HERMES

HERMES is a fixed target experiment being conducted using the HERA particle accelerator at DESY. The experiment's goal is to investigate the quark-gluon structure of matter by examining how a nucleon constituents affect its spin. HERMES conducted its first run from 1995 to 2000, and a second run began in 2001 and is scheduled to end during the summer 2007. HERMES scatters longitudinally polarized electron and positron beams of 27.5 GeV from longitudinally or transversely polarized targets. In the years 2002 - 2005, HERMES has taken data with a transversely polarized proton target to measure single-spin asymmetries for semi-inclusive electroproduction of charged pions in deep-inelastic scattering. So far results for Collins asymmetry and Sivers asymmetry has been published in [89] for charged pions and kaons. Their measurement so far reveals a non zero Collins and Sivers asymmetry on a proton. A non-zero Collins asymmetry shows clear evidence for the existence of both transversity distribution function and the Collins fragmentation function. A non-zero Sivers asymmetry provide first evidence for a T-odd parton distribution function appearing in leptoproduction which implies a non vanishing orbital angular momentum of the quarks inside the nucleon. The results observed by HERMES play a major role in the global analysis performed by many groups to extract the transversity distribution function for u and d quarks.

5.5.2 BELLE

The BELLE experiment [97] at the asymmetric e^+e^- collider KEK-B at Tsukuba, Japan, is mainly dedicated to the study of CP violation in B meson decays. Its center of mass energy is tuned to the resonance at $\sqrt{s} = 10.58$ GeV/c, whereas background studies are performed off resonance at 10.52 GeV/c. These off resonance events are studied in order to measure spin-dependent and precise spin-independent

fragmentation functions. Using the KEK-B storage ring, 8 GeV/c electrons are collided with 3.5 GeV/c positrons producing $q\bar{q}$ pairs. In $e^{+}e^{-} \rightarrow q\bar{q}$, one measures the azimuthal distribution of two pions in opposite hemispheres [98]. With that one either computes the azimuthal angles of each pion relative to the thrust axis, which results in a $cos(\phi_1 + \phi_2)$ modulation, or one calculates the azimuthal angle relative to the axis defined by the 2nd pion, which results in a $cos(2\phi_0)$ modulation. The first method directly accesses the Collins fragmentation functions whereas the second method contains a convolution integral of the Collins fragmentation function over all involved transverse momenta. The BELLE experiment plays a major role in the global analysis performed by many groups to extract the transversity distribution function for u and d quarks.

5.5.3 RHIC - SPIN

The RHIC facility at Brookhaven National Laboratory was built originally for heavy ion physics, to search for the new state of matter, quark gluon plasma. The facility has its own spin physics program with the help of two experiments, PHENIX [99] and STAR [100]. Both experiments concentrate on the investigation of the quark and gluon helicity distributions in nucleon using two polarized proton beams colliding with each other. In addition to the helicity distributions also transversity and transverse momentum dependent distribution or fragmentation functions in hadron production can be accessed via azimuthal asymmetries. Such experiments can give a direct access to the combination of quark and anti-quark transversity when colliding transversely polarized protons.

5.5.4 CEBAF

The Continuous Electron Beam Accelerator Facility at the Jefferson Lab operates a 6 GeV electron beam at very high luminosity. Most of the measurements with the low energy electrons are performed in a low Q^2, low W^2 region. Nevertheless, non-zero azimuthal beam spin asymmetries have been reported at the CLAS experiment [101] in the deep inelastic regime. An upgrade of the accelerator to a maximal energy of 12 GeV will allow to increase the statistical precision for SIDIS

5.6 Future experiments

The previously presented experiments have already been producing results. There are two more new experiments lined up to measure transverse spin effects.

5.6.1 PAX

PAX is a proposed experiment at GSI in Germany. Proposed measurement is via Drell-Yan process by colliding transversely polarized antiprotons with a transversely polarized fixed target. The advantage of using antiprotons instead of protons is that one can measure two valence quark transversities instead of a valence and a sea transversities.

5.6.2 EIC

Electron **I**on **C**ollider is planned with the possibility to have both a polarized electron as well as a polarized proton beam. Realization of the project has two possibilities.One among them is called eRHIC solution, which involves adding an electron accelerator of up to 10 GeV energy to the existing RHIC facility with proton energies of 50 - 250 GeV. The other involves upgrading the electron beam at CEBAF by polarized proton beam at reasonable high energies.

Chapter 6

Conclusion and outlook

> "I think and think for months and years. Ninety-nine times, the conclusion is false. The hundredth time I am right."
>
> Albert Einstein

The contribution reported in this thesis is the analysis of the data taken with transverse spin configuration during the COMPASS beam-time 2002 - 2004. In Semi-Inclusive DIS of polarized leptons on a transversely polarized target, eight azimuthal modulations appear in the cross-section. Within the QCD parton model, four azimuthal asymmetries can be interpreted at leading order, two of them being the already known Collins and Sivers asymmetries. The other two leading twist asymmetries are related to different transverse momentum dependent quark distribution functions. There are four additional asymmetries which can be interpreted as twist-three contributions.

The analysis was centered on the extraction of eight transverse momentum dependent asymmetries for the first time at COMPASS. The asymmetries were extracted separately for positive and negative hadrons as well as pions and kaons. All asymmetries were extracted with two different methods, namely one-dimensional and two-dimensional method. The two-dimensional fit proves to be a powerful and elegant method to extract any number of asymmetries, results obtained with two-dimensional fit are very close to those obtained with the one-dimensional fit, given the smallness of all obtained asymmetries. Therefore, the final results presented in this thesis are extracted using one-dimensional fitting procedure.

All the measured asymmetries are small, mostly compatible with zero within the statistical errors. The most likely interpretation for this behavior is a

cancelation between the proton and neutron asymmetries in the results obtained with COMPASS iso-scalar target.

Especially the new global analysis for Collins and Sivers mechanism obtained with the data from COMPASS, HERMES and BELLE experiments clearly shows that the Collins and Sivers effect are real. It also shows that precise COMPASS data with deuteron target has to be used to estimate the down quark transversity distribution $\Delta_T d$. COMPASS data provide convincing evidence on the cancelation of the u and d quark Sivers distribution function.

After the SPS stop in 2005, COMPASS started data acquisition in 2006 but data were taken only with longitudinal mode. Currently in the year 2007, data acquisition is going on with transversely polarized proton target with much higher acceptance. With the improved geometrical acceptance of the spectrometer obtained using the new COMPASS polarized target magnet, it should result in the measurements of the asymmetries with reduced error bars at large x.

Measurements for transverse spin dependent asymmetries with a proton target at COMPASS is expected to be non-zero and a new global analysis with new COMPASS proton data would play a crucial role in the field of transverse spin physics.

List of Tables

List of Figures

Bibliography

[1] G. Baum *et al.* Compass: A proposal for a common muon and proton apparatus for structure and spectroscopy. CERN - SPSLC-96-14.

[2] J. Ralston and D. E. Soper. Nucl. Phys. **B152** 109 (1979).

[3] C. Scholz B. Povh, K. Rith and F. Rith. Particles and Nuclei: An Introduction to the physical concepts. Springer, 2003.

[4] E. Leader. Spin in Particle Physics. Cambridge University Press, 2001.

[5] A. V. Manohar. An introduction to spin dependent deep-inelastic scattering. Lectures given at Lake Loise Winter Inst. Lake Loise, Canada. [arXiv:hep-ph/9204208], 1992.

[6] D. J. Griffiths. Introduction to Elementary Particles. John Wiley & Sons, New York, USA, 1987.

[7] F. Halzen and A. D. Martin. Quarks and Leptons: An introduction course in modern physics. John Wiley & Sons, 1984.

[8] R. G. Roberts. The Structure of the proton: Deep Inelastic Scattering. Cambridge University Press, 1990.

[9] Thierry Pussiex and Roland Windmolders. A collection of formulas for spin dependent deep inelastic scattering. Technical report, SMC Report, 1993.

[10] M. Anselmino *et al.* The theory and phenomenology of polarized deep inelastic scattering. Phys. Rept. **261** 1-124, (1995).

[11] J. D. Bjorken. Asymptotic sum rules at infinite momentum. Phys. Rev. **179** 1547-1553, (1969).

[12] P. L. Anthony *et al.* Precision measurement of the proton and deuteron spin structure functions g_2 and asymmetries a_2. Phys. Lett. **B553** 18-24, (2003).

[13] L. G. Greeniaus. Deep inelastic scattering with spin. Lectures presented for the troisieme cycle de la physique en suisse romande. Technical report, 2001.

[14] J. D. Bjorken. Inelastic electron-proton and gamma-proton scattering and the structure of the nucleon. Phys. Rev. **185** 5, (1969).

[15] C. G. Callan and D. J. Gross. High-energy electoproduction and the constitution of the electric current. Phys. Rev. Lett. **22** 156-159, (1969).

[16] E. D. Bloom *et al.* High energy inelastic e-p scattering at 6-degrees and 10 degrees. Phys. Rev. Lett. **23** 930-934, (1969).

[17] M. Breidenbach *et al.* Observed behavior of highly inelastic electron - proton scattering. Phys. Rev. Lett. **23** 935-939, (1969).

[18] R. E. Taylor. Deep inelastic scattering: The early years. Rev. Mod. Phys. **63** 573-595, (1991).

[19] H. W. Kendall. Deep inelastic scattering: Experiments on the proton and the observation of scaling. Rev. Mod. Phys. **63** 597-614, (1991).

[20] J. I. Friedman. Deep inelastic scattering: Comparisons with the quark model. Rev. Mod. Phys. **63** 615-629, (1991).

[21] R. P. Feynmann. Very high energy collisions of hadrons. Phys. Rev. Lett. **23** 24, (1969).

[22] M. Gell-Mann. A schematic model of baryons and mesons. Phys. Rev. Lett. **214** 8, (1964).

[23] C. Zweig. An su3 model for strong interaction symmetry and its breaking. CERN Report pages 401-412, (1964).

[24] Y. l. Dokshitzer. Calculation of the structure functions for deep inelastic scattering and e^+e^- annihilation by perturbation theory in quantum chromodynamics. Sov. Phys. JETP **46** 641-653, (1977).

[25] V. N. Gribov and L. N. Lipatov. e^+e^- pair annihilation and deep inelastic ep scattering in perturbation theory. Sov. J. Nucl. Phys. **15** 675-684, (1972).

[26] L. N. Lipatov. The parton model and perturbation theory. Sov. J. Nucl. Phys. **20** 94-102, (1975).

[27] G. Altarelli and G. Parisi. Asymptotic freedom in parton language. Nucl. Phys. **B126** 298-330, (1997).

[28] V. Barone and P. G. Ratcliffe. Transverse Spin Physics. World Scientific, New Jersey, London, Singapore, Hong Kong, 2003.

[29] X. Ji R. L. Jaffe. Phys. Rev. Lett. **67** 552, (1991).

[30] R. L. Jaffe. Can transversity be measured? [arXiv:hep-ph/9710465 V2].

[31] K. Bora and D. K. Choudhury. Transversity of quarks in a nucleon. Pramana Journal of Physics **61** 979-985, (2003).

[32] A. Henneman A. Bachhetta, Mariaelena Boglione and P. J. Mulders. The full spin structure of quarks in the nucleon. [arXiv:hep-ph/0005140] 2000.

[33] John C. Collins and Davison E. Soper. Parton distribution and decay functions. Nucl. Phys. **B194** 445, (1982).

[34] Daniel Boer and P. J. Mulders. Time-reversal odd distribution functions in leptoproduction. Phys. Rev. **D57** 5780-5786, (1998).

[35] Alessandro Bacchetta. Probing the transverse spin of quarks in deep inelastic scattering. PhD thesis, [arXiv:hep-ph/0212025] 2002.

[36] Rainer Jakob. Transverse Momenta in Hard Scattering Process. PhD thesis, University of Wuppertal, 2002.

[37] J.-P. Ma X. Ji and F. Yuan. Phys. Rev. **D71** 034005, (2005).

[38] D.Boer *et al.* Nucl. Phys. **B667** 201-241, (2003).

[39] J. C. Collins. Fragmentation of transversely polarized quarks probed in transverse momentum distributions. Nucl. Phys. **B396** 161-182, (1993).

[40] A. Bachetta *et al.* Semi-inclusive deep inelastic scattering at small transverse momentum. [arXiv:hep-ph/0611265 V1].

[41] A. Henneman A. Baccheta, M. Boglione and P. J. Mulders. Phys. Rev. Lett. **85** 712, (2002).

[42] A. Kotzinian. Nucl. Phys. **B441** 234, (1995).

[43] D. Sivers. Phys. Rev. **D41** 83, (1990).

[44] M. Anselmino *et al.* Phys. Rev. **D71**, (2005).

[45] A.Kotzinian M. Anselmino, A. Efremov and B. Parsamyan. Phys. Rev. **D74** 074015, (2006).

[46] P. Abbon *et al.* [COMPASS Collaboration]. The compass experiment at cern. CERN-PH-EP. e-print: hep-ex/0703049 Jan 2007.

[47] Lao gatignon. User guide for the m2 beam. http://gatignon.home.cern.ch/gatignon/m2manual.html.

[48] H. W. Atherton *et al.* Precise measurement of particle production by 400 GeV/c protons on beryllium targets. Technical report, CERN Yellow report, 1980.

[49] G. K. Mallot. The compass spectrometer at CERN. Nucl. Inst. Meth. **A518** 121-124, (2004).

[50] R. L. Garwin. Observations of the failure of conservation of parity and charge conjugation in meson decays. Phys. Rev. **105** 1415, (1957).

[51] G.Backenstoss. Helicity of μ^- mesons from π-meson decay. Phys. Rev. **6** 415, (1961).

[52] D.Adams *et al.* Measurement of the smc muon beam polarization using the asymmetry on the elastic scattering of polarized electrons. Nucl. Inst. Meth. **A443** 1, (2000).

[53] B. Adeva *et al.* Measurement of the polarization of a high energy muon beam. Nucl. Inst. Meth. **A343** 363, (1998).

[54] Takabayashi *et al.* First results of the large COMPASS ^{6}lid polarized target. Nucl. Inst. Meth. **A498** 1-3, (2003).

[55] N. W. Schellingerhout *et al.* Nucleon polarization in three-body models of polarized ^{6}li. Phys. Rev. **C48** 2714, (1993).

[56] G. Abraham and M. Goldman. Principles of dynamic nuclear polarization. Rep. Prog. Phys. **41** 395, (1978).

[57] J. Kyynrainen. The SMC polarized target. Nucl. Inst. Meth. **A356** 47, (1995).

[58] D. Adams *et al.* The polarized double cell target of the SMC. Nucl. Inst. Meth. **A437** 23, (1999).

[59] J. Koivunniemi. Dilution refigerator for compass polarized target. Physica **B284-288** 2012-2013, (2000).

[60] J. Bisplinghoff *et al.* A scintillating fibre hodoscope for high rate applications. Nucl. Inst. Meth. **A490** 101-111, (2002).

[61] H. Angerer *et al.* Present status of silicon detectors in COMPASS. Nucl. Inst. Meth. **A512** 229-238, (2003).

[62] A. Magnon *et al.* Tracking with $40 \times 40 cm^2$ micromega detectors in the high energy, high luminosity COMPASS experiment. Nucl. Inst. Meth. **A478** 210-214, (2002).

[63] F. Kunne *et al.* Micromegas as a large microstrip detector for the COMPASS experiment. Nucl. Inst. Meth. **A469** 133-146, (2001).

[64] F. Sauli *et al.* Performance of gem detectors in high intensity particle beams. Nucl. Inst. Meth. **A470** 548-561, (2001).

[65] F. Sauli *et al.* Constructing, test and commissioning of the triple-gem tracking detector for COMPASS. Nucl. Inst. Meth. **A470** 548-561, (2001).

[66] V. N. Bychkov. Construction and manufacture of large size straw-chambers of the COMPASS spectrometer tracking system. Particles and nuclei Letters **2(111)** 64-73, (2002).

[67] E. Albrecht *et al.* Nucl. Inst. Meth. **A553** 215, (2005).

[68] S. Torre *et al.* The COMPASS RICH project. Nucl. Inst. Meth. **A433** 207-211, (1999).

[69] F. Tessarotto *et al.* COMPASS RICH-1. Nucl. Inst. Meth. **A478** 340-343, (2002).

[70] O. Gavrishchuk *et al.* Calorimeter for hadron detection in the energy range 10 - 100 GeV. Technical report, JINR Dubna D13-2004-186, 2004.

[71] F. Binon *et al.* Nucl. Inst. Meth. **A256** 444, (1987).

[72] D. Alde *et al.* Nucl. Phys. **B269** 485, (1986).

[73] J. Hannapel *et al.* The COMPASS trigger system for muon scattering. Nucl. Inst. Meth. **A550** 217-240, (2005).

[74] H. Fischer *et al.* The COMPASS data acquisition system. IEEE Trans. Nucl. Sci. **49** 443-447, (2002).

[75] PHAST. http://ges.home.cern.ch/ges/phast/index.html. Technical report.

[76] Rene Brun. Root - an object oriented data analysis framework. Technical report, CERN, 2001.

[77] E. Ageev *et al.* [COMPASS Collaboration]. Nucl. Phys. **B765** 31, (2007).

[78] Release note on collins and sivers asymmetries on hadrons identified as pions and kaons from compass 2003-2004 transverse run. Technical report, COMPASS Internal note, 2006.

[79] P. Schiavon. Particle identification in compass rich 1. Technical report, COMPASS Internal note, 2000.

[80] P. Schiavon. Particle identification in compass rich 1. Technical report, COMPASS Internal Note, 2001.

[81] F. Bradamante and A. Martin. A method to compute the collins angle in transversely polarized DIS. Internal COMPASS note 2002 -5.

[82] K. Gustafsson. Computation of the dilution factor for the year 2002 compass data. COMPASS internal note 2003 -3.

[83] Release note on extraction of target transverse spin dependent asymmetries from COMPASS 2002-2004 runs. Technical report, COMPASS Internal note, 2007.

[84] V. Y. Alexakhin *et al.* [COMPASS Collaboration]. Phys. Rev. Lett. **94**, (2005).

[85] Aram Kotzinian. Remarks on acceptance effects in asymmetry extraction. Technical report, Compass Internal Note, 2007.

[86] Physical Review D chapter Statistics, pages 010001-229, 010001-238. The American Physical Society, 2002.

[87] Philip. R. Bevington. Data Reduction and Error Analysis for the Physical Sciences. McGraw-Hill Book Company.

[88] F. James and M. Winkler. Minuit user's guide. Technical report, CERN, 2004.

[89] A. Airapetian *et al.* [HERMES Collaboration]. Single spin asymmetries in semi-inclusive deep-inelastic scattering on a transversity polarized hydrogen target. Phys. Rev. Lett. **94**, (2005).

[90] W. Vogelsang and F. Yuan. Single-transverse spin asymmetries: From DIS to hadronic collisions. Phys. Rev. **D72**, (2005).

[91] K. Goeke A. Efremov and P. Schweitzer. Collins effect in semi-inclusive deeply inelastic scattering and in e^+e^- annihilation. [arXiv:hep-ph/0603054 v2].

[92] M. Anselmino *et al.* Transversity and collins functions from SIDIS and e^+e^- data. [arXiv:hep-ph/0701006 v2].

[93] M. Anselmino *et al.* Extracting the sivers function from polarized SIDIS data and making predictions. [arXiv:hep-ph/0507181 v2].

[94] S. J. Brodsky and S. Gardner. Evidence for the absense of gluon orbital angular momentum in the nucleon. [arXiv:hep-ph/0608219].

[95] X. Artru. "the transverse spin", proceedings of 10th rhodanien seminar. [arXiv:hep-ph/0207309].

[96] A. Bacchetta and M. Radici. Modeling dihadron fragmentation functions. [arXiv:hep-ph/0608037].

[97] A. Abashian *et al.* The BELLE detector. Nucl. Inst. Meth. **479** 117-232, (2002).

[98] R. Seidl. Spin dependent fragmentation functions at BELLE. In Spin04 16th international spin physics symposium 2004.

[99] L. Aphecetche *et al.* PHENIX calorimeter. Nucl. Inst. Meth. **499** 521-536, (2003).

[100] K. H. Ackermann *et al.* STAR detector overview. Nucl. Inst. Meth. **499** 624-632, (2003).

[101] H. Avakian *et al.* Measurement of beam spin asymmetries for deep inelastic π^+ electroproduction. [arXiv:hep-ex/0301005] 2003.

Acknowledgments

I would like to conclude the dissertation by expressing my indebtedness to all those who have significantly helped me during the past years at Bonn.

First and foremost, I express my deepest sense of gratitude and respect to my adviser Prof. Dr. Frank Hinterberger for providing me the opportunity to work under his supervision at the University of Bonn. His constant encouragement, constructive criticism and above all, his efforts to accord my financial support, for my sustenance here at Bonn, have been the guiding force behind my writing the thesis and bringing it to its present form for which I shall ever remain grateful to him.

I would like to thank my group leader Prof. Dr. Jens Bisplinghoff, for his continuous support in this thesis work. He was always there to listen and to give advice. He is responsible for involving me in the COMPASS Experiment at CERN in the first place and showed me different ways to approach a research problem and the need to be persistent to accomplish any goal.

Words can hardly express how much I owe to Dr. Rainer Joosten without whose assistance my thesis work would not have been possible. Rainer has been a friend and mentor. He taught me how to write academic papers, made me a better programmer, had confidence in me when I doubted myself, and bought out the good ideas in me. He was always there to meet and talk about my ideas, to proofread my thesis and to ask me good questions to help me think through my problems. My heartfelt thanks are due to him.

I would like to thank my colleagues, Frank Massmann and Ralf Ziegler. Special thanks is due to Dr. Kay Ulbrich for always being there to guide me through times of trouble with programming. I would like to seize this opportunity to express my gratitude to the other members of the Transversity analysis group, especially to Prof. Dr. Franco Bradamante and Prof. Dr. Anna Martin for their useful comments on various aspects of this work. Special thanks to Bakur Parsamyan, who not only cross-checked my results but also co-operated to meet deadlines.

In the midst of serious work over last four years some lasting memory of cherishable moments resulted from the few close bonds that were forged during this period of stay at Bonn. Innumerable thanks to Nirmal Robinson, Jinitha Robinson and their cute son Bryan for being my family away from home. Special thanks to Poornnima Anbalagan for carefully proofreading my thesis and for being there whenever i needed help. I would like to thank all my friends in Bonn: Amit, Hari, Nikhil,.....

Last but not least, I would like to thank my family: Mr. P. C. Venugopal and Mrs. Susila Venugopal for giving me life in the first place , for educating me with aspects from both arts and science, for unconditional support and encouragement to pursue my interests, even when it went beyond boundaries. My sister Yogalakshmi, for listening to my complaints and frustrations and for believing in me. My little niece Chetna, who manage to cheer me up anytime although she is miles away in India. A heartfelt thanks to all.